Development of novel algorithms suitable for clinical assessment of ocular diseases using OCT imaging

Yuxuan Cheng

A dissertation

submitted in partial fulfillment of the

requirements for the degree of

Doctor of Philosophy

University of Washington

2024

Reading Committee:

Ruikang K. Wang, Chair

Tueng Shen

Ramkumar Sabesan

Dan Fu

Program Authorized to Offer Degree:

Bioengineering

University of Washington

Abstract

Development of novel algorithms suitable for clinical assessment of ocular diseases using OCT imaging

Yuxuan Cheng

Chair of the Supervisory Committee:

Ruikang K. Wang

Department of Bioengineering

Optical coherence tomography (OCT) is a widely utilized imaging modality in ophthalmology. However, its accuracy and clinical utility are limited by several significant challenges. This study describes a series of innovative signal processing approaches and novel algorithms for OCT and OCT angiography (OCTA) that address these limitations and enhance the accuracy and comprehensiveness of imaging for the diagnosis and monitoring of ocular diseases.

Our first contribution is a three-dimensional registration algorithm that enhances the contrast and signal-to-noise ratio of OCTA images, thereby facilitating improved visualization and quantification of the choriocapillaris. Additionally, we propose a novel model for widefield OCTA distortion correction and demonstrate that this correction significantly improves quantification metrics.

Subsequently, we differentiate between various types of drusen and their interaction of with the choriocapillaris, and analyze the grading exercise of macular atrophy. This study demonstrated how OCT can be utilized to identify and monitor the biomarkers of age-related macular degeneration accurately.

To further advance AMD diagnosis and monitoring, a deep learning model for geographic atrophy (GA) segmentation based on hyper-transmission defects is presented. This is complemented by a method for

automatic identification, segmentation, and comparison of hyperpigmentation extent using optical attenuation coefficients (OAC) obtained from both swept-source (SS) OCT and spectral domain (SD) OCT scans. By enhancing our understanding of these biomarkers, OCT and OCTA can act a critical role in quantifying the progression of this disease.

Together, these methods represent a significant advancement in OCT image analysis, holding immense promise for improved clinical diagnosis and monitoring of ocular diseases.

Table of Contents

Abstract 3

Table of Contents 5

Acknowledgement 7

List of Figures 8

List of Tables 11

Chapter 1. Introduction 12

1.1 Significance and research motivation 12

1.2 Time domain optical coherence tomography 12

1.3 Fourier domain optical coherence tomography 13

1.4 Optical coherence tomography angiography (OCTA) 16

1.5 Current status and challenge in eye imaging 18

1.6 Scope of the thesis 20

Chapter 2. Optimizing OCT Image Quality and Usability through Robust Image Processing Algorithms 21

Chapter 2.1 Robust three-dimensional registration on optical coherence tomography angiography for speckle reduction and visualization 21

2.1.1 Introduction 21

2.1.2 Methods 23

2.1.3 Results 30

2.1.4 Discussion and conclusion 37

Chapter 2.2 Optical coherence tomography angiography distortion correction in widefield montage images 41

2.2.1 Introduction 41

2.2.2 Methods 42

2.2.3 Results 49

2.2.4 Discussion 51

2.2.5 Conclusion 53

Chapter 3. Using OCT to better understand the biomarkers of Age-related Macular Degeneration 54

Chapter 3.1 Calcified Drusen Prevent the Detection of Underlying Choriocapillaris Using Swept-Source Optical Coherence Tomography Angiography 54
3.1.1 Introduction 54
3.1.2 Material and methods 56
3.1.3 Results 62
3.1.4 Discussion 69
Chapter 3.2 Comparison between OCT B-scan and En Face Imaging for the Diagnosis of Early Macular Atrophy in Age-Related Macular Degeneration 72
3.2.1 Introduction 72
3.2.2 Methods 74
3.2.3 Results 77
3.2.4 Discussion 81
Chapter 4. Developing Automated Biomarker Detection Techniques for Age-related Macular Degeneration Using OCT and OCTA Imaging 83
Chapter 4.1 Automatic segmentation of geographic atrophy in both SD-OCT and SS-OCT scans using deep learning 83
4.1.1 Introduction 83
4.1.2 Methods 84
4.1.3 Results 88
4.1.4 Discussions and conclusion 93
Chapter 4.2 Depth-resolved visualization and automated quantification of hyperreflective foci on OCT scans using optical attenuation coefficients 98
4.2.1 Introduction 98
4.2.2. Method 99
4.2.3 Results 103
4.2.4 Discussion 106
4.2.5 Conclusion 108
Chapter 5. Summary and feature work 109
List of Journal Publications 111
Bibliography 113

Acknowledgement

My deepest gratitude goes to my advisor, Dr. Ruikang Wang, for his support and mentorship throughout my PhD journey. I am grateful to him for accepting me as his PhD student year ago. His emphasis on hard work, productivity, and perseverance have shaped me as a researcher.

Next, I would like to express my sincere gratitude to my supervisory committee members, Dr. Tueng Shen, Dr. Ramkumar Sabesan, and Dr. Dan Fu (Graduate School Representative) for their invaluable guidance and time dedicated to reviewing my work. Their suggestions significantly contributed to the completion of my research, and I appreciate their willingness to attend my defense despite their busy schedules.

I would also like to express my deep appreciation to my collaborators and mentors: Dr. Philip J. Rosenfeld of the Bascom Palmer Eye Institute for his expertise in age-related macular degeneration. His rigorous approach to research and keen intuition have been invaluable in my own development. I should also thank Dr. Amir Kashani of Johns Hopkins University who has provided invaluable assistance and guidance in navigating the research and clinical applications of OCTA. Additionally, I appreciate Dr. Steven Jacques for his education and discussions based on his profound knowledge of tissue optics.

I am also indebted to my colleagues in the Biophotonics and Imaging Laboratory (BAIL) and collaborators. I recall their invaluable support and our friendship during my PhD studies. I would like to express my sincerest gratitude to Yaping Shi, Dr. Jie Lu, Zhiying Xie, Dr. Athira B S, Sivathanu Kumar, Dr. Mengxi Shen, Jianqing Li, Dr. Farhan E. Hiya, Yuxin Xia, Zhaoyu Gong, and Dr. Qing Chao and all of my other colleagues for their invaluable support and guidance throughout my academic career. I would like to express my gratitude to Dr. Zhongdi Chu, Dr. Qinqin Zhang, Dr. Yuandong (Jenny) Li, Dr. Nhan Le, Dr. Qinghua He, Dr. Shaozhen Song, Dr. Mitchell Kirby, Dr. Anthony Deegan, Dr. Wei Wei, Dr. Hao Zhou, Xiao Zhou, Ziyu Liu for their invaluable contributions to my academic career, both professionally and personally. I am grateful for the fond memories we have shared and wish each of them the very best in their future endeavors.

Finally, I would like to express my profound gratitude to my parents for their unwavering support throughout my PhD studies. Without their encouragement and guidance, I would not have been able to reach this milestone.

List of Figures

Figure 1.2.1 Schematic of time domain optical coherence tomography. 13

Figure 1.3.1 Schematic Fourier domain optical coherence tomography. 14

Figure 1.4.1 Imaging of branch retinal vein occlusion (BRVO) in the left eye of a 68 year-old female. .. 17

Figure 2.1.1. An illustration of the correction of affine and B-spline registration on 2D images. 25

Figure 2.1.2. The illustration of anisotropic deformation and multi-resolution down-sampling approach using 3D OCT retinal image $a(x, y, z)$ as an example due to patient movement during image capture. ... 26

Figure 2.1.3. The Workflow of 3D volumetric registration. 27

Figure 2.1.5. A comparison of original and noise deducted B-scan OCT images of fovea scan. 33

Figure 2.1.6. A comparison of different number of averaging. 34

Figure 2.1.7. Illustration of the OCT imaging of skin with volume averaging. 35

Figure 2.1.8. The performance assessment with the increase of averaging numbers. 36

Figure 2.2.1: Schematic of image acquisition in OCT system. 43

Figure 2.2.2. Flow chart describing the procedure for distortion correction and image quantification. 44

Figure 2.2.3. Geometric model for radial distortion correction. 45

Figure 2.2.4: Image registration and montaging procedure. 47

Figure 2.2.5. Example of quantitative analyses on macular and peripheral regions. 48

Figure 2.2.6. Relationship between before- and after-correction vessel area density. 50

Figure 2.2.7: Relationship between before- and after-correction flow impairment area. 50

Figure 2.2.8: Relationship between before- and after-correction vessel complexity. 51

Figure 3.1.1. A schematic flow chart illustrating the image processes. 57

Figure 3.1.2. Examples of choriocapillaris flow deficit (CCFD) density masks and drusen lesion masks for computing Dice similarity coefficients. 60

Figure 3.1.3. Examples of a normal eye (A-F), an eye with soft drusen (G-L), and an eye with calcified drusen (M-R) imaged using swept source OCT angiography (SS-OCTA) scans. 63

Figure 3.1.4. Illustration of OCT imaging characteristics of calcified drusen (CaD). 64

Figure 3.1.5. Comparison of the choriocapillaris flow deficits (CCFDs) among the three groups of eyes. 65

Figure 3.1.6. Dice similarity coefficients of choriocapillaris flow deficit density masks associated with calcified drusen and soft drusen masks. 66

Figure 3.1.7. Phantom experiment to confirm the scattering tail due to highly scattering deposits that simulate calcified drusen demonstrating the inability to detect OCTA flow signals beneath the scattering lesions. 67

Figure 3.1.8. A representative case that evolved from a normal druse to a calcified druse to a hypertransmission defect (hyperTD) over a nine-month period. 68

Figure 3.2.1. Identification of incomplete retinal pigment epithelium and outer retinal atrophy (iRORA) and complete RORA (cRORA) in a representative Eye using SD-OCT and SS-OCT Instruments. 76

Figure 3.2.2. Four representative cases used to grade iRORA, cRORA, and persistent choroidal hyperTDs. 78

Figure 3.2.3. Comparison of total area measurements for cRORA on SD-OCT scans and persistent choroidal hyperTDs on SS-OCTA scans. 79

Figure 4.1.1. Representative images obtained using the optical attenuation coefficient (OAC) algorithms and the traditional OCT images with choroidal hypertransmission defect (hyperTDs). 86

Figure 4.1.2. Model architecture and specifications used to perform geographic atrophy segmentation. . 87

Figure 4.1.3. Geographic atrophy (GA) visualized using the optical attenuation coefficient (OAC) estimated from swept-source optical coherence tomography (SS-OCT). 90

Figure 4.1.4. *En face* visualization of geographic atrophy (GA) predicted by trained models from a 92 years old male patient. 92

Figure 4.1.5. *En face* visualization of geographic atrophy (GA) predicted by trained models from a 79-year-old male patient. 93

Figure 4.1.6. Quantitative comparison of geographic atrophy (GA) square-root area predicted by trained models with ground truth. 94

Figure 4.2.1. Representative OCT B-scans of eyes with drusen, intra-retinal pigment migration and hyperreflective foci along the retina pigment epithelium. 100

Figure 4.2.2. Color-coded visualization of hyperreflective foci (HRF) using optical attenuation coefficients (OACs). 102

Figure 4.2.3. Comparison of the area of total pigment burden measured manually and automatically. .. 104

Figure 4.2.4. An example of manual and automated segmentations of the total pigment burden in an eye with hyper-reflective foci along the RPE. 105

Figure 4.2.5. An example of manual and automated segmentations of the total pigment burden in an eye with intra-retinal hyper-reflective foci. 105

List of Tables

Table 2.1.1. The normalized correlation coefficient of original images registered images 37

Table 2.2.1: Average measurements by region, before and after image correction. 49

Table 3.1.1. Characteristics of subjects and eyes with calcified drusen, typical soft drusen eyes, and eyes with no obvious disease 62

Table 4.1.1 Patient demographics 88

Table 4.1.2. Training and testing results of proposed models. 91

Table 4.1.3. Evaluation metrics for all trained models. 91

Chapter 1. Introduction

1.1 Significance and research motivation

Blindness and visual impairment have a profound impact on quality of life, impeding daily activities and social interactions. In 2020, it is estimated that approximately 43.3 million people worldwide will be blind, 295 million will have moderate to severe visual impairment, and 258 million will suffer from mild visual impairment.[1] Notably, studies have demonstrated that up to 80% of all cases of visual impairment can be prevented or treated through the established prevention and treatment methods.[2]

Early diagnosis in ophthalmology is crucial as timely treatment can prevent or delay irreversible damage. Traditional diagnostic tools, such as the slit lamp microscope or fundus photography have been supplemented by advanced imaging technologies to enhance early detection and treatment efficacy.[3] Fluorescein angiography (FA) and indocyanine green angiography (ICGA) are notable for their ability to visualize retinal and choroidal vasculature, respectively. [4] However, these methods require the injection of contrast agents, which can result in severe side effects. Ultrasonography offers a contact-based, contrast-free alternative with deep penetration, yet it typically provides lower resolution imaging.[5]

Optical Coherence Tomography (OCT) represents a significant advancement in non-invasive ophthalmologic imaging techniques, as it invented in 1991.[6–9] It provides high-resolution, cross-sectional and en face images of the retina and choroid, which are essential for diagnosing and monitoring various ocular diseases. It has enabled the visualization of ocular structures with unprecedented detail, thereby facilitating the early detection and management of diseases that could lead to irreversible vision loss[10–13].

Despite the considerable advantages that OCT offer, it is important to understand their limitations. A number of challenges can affect the quality and utility of images produced by OCT, including speckle noise, motion artifacts, and quantification issues[14–16]. The primary motivation of this research is to address these limitations by developing advanced image processing algorithms that enhance the quality and diagnostic power of OCT images, thereby extending their application in clinical practice and medical research.

1.2 Time domain optical coherence tomography

Time-Domain Optical Coherence Tomography (TD-OCT), the first generation of OCT technology, employs an interferometric technique that capitalizes on the interference signals generated by a broadband optical field.[6,7] This field is split into a sample arm and reference arm and then recombined to form the interferometric signal.

The configuration of a typical TD-OCT system involves an interferometer equipped with a low-coherence, broadband light source. The emitted light (E_{in}) enters the system, passing through a beam splitter where it divides into two separate beams. One beam travels towards a reference mirror along the reference path (E_r), and the other penetrates the biological sample (E_s). As the light reflect back to the splitter, they recombine and produce an interference pattern as illustrated in Figure 1.2.1. The intensity of the interference is strongest when the optical paths of the recombined beams match within the coherence length of the light source, this is known as the coherence gate. [17]

By mechanically adjusting the position of the reference mirror, TD-OCT can scan different depths within the tissue. This depth-resolved scanning reconstructs the tissue's reflectivity profile along the depth (Z axial) direction, known as an A-line. However, the mechanical scanning process limits the speed of TD-OCT, making it slower than that required for clinical applications.

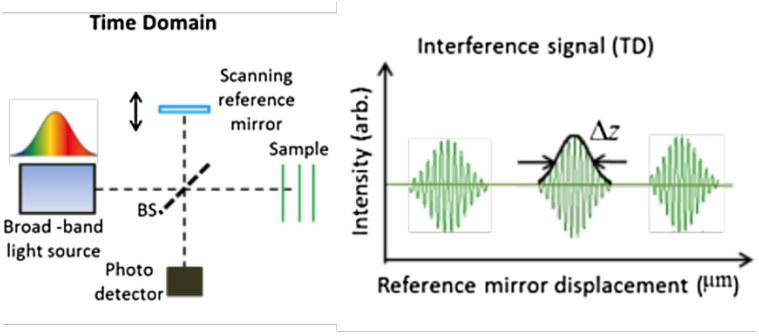

Figure 1.2.1 Schematic of time domain optical coherence tomography.

Courtery by Drexler, Wolfgang, et al. [7] by Creative Commons Attribution 4.0 Unported License.

Despite its limitations in speed, TD-OCT played an important role in the early development of OCT technologies.[8] It provided a practical method for the visualization and assessment of the internal microstructure of the eye and other tissues. The ability to obtain detailed cross-sectional images non-invasively was a breakthrough in eye imaging. And currently, it is still used for the design of some special OCT systems, such as some full-field OCT systems.[18]

1.3 Fourier domain optical coherence tomography

Fourier-domain optical coherence tomography (FD-OCT) represents an evolution in OCT technology. It overcomes the limitations of mechanical scanning by capturing depth information through frequency domain analysis. Unlike TD-OCT, which requires physical movement of a reference mirror, FD-OCT

encodes time delay information within a spectral interferogram, making the imaging process significantly faster and more efficient.[19–21]

FD-OCT converts the spectral data of light scattered from a sample into depth information through the Fourier transform. This process effectively constructs the depth information of the sample from the interference data without the need to physically adjust the position of the reference mirror. This method is not only faster but also enhancing the resolution and quality of the images. Currently, two major types of FD-OCT have been developed.

Spectral-Domain Optical Coherence Tomography (SD-OCT)

The first type of FD-OCT is spectral-domain OCT (SD-OCT). In this configuration, the reference mirror remains stationary, and the interference pattern is diffracted by a grating into its constituent spectral components.[22] These components are then detected simultaneously by a linear detector array (CCD or CMOS) as shown in Figure 1.3.1. This simultaneous acquisition of frequency information from all depths of the tissue allows for rapid generation of A-line scans through the simple operation of Fourier transforming the captured spectral interferograms.[17,19]

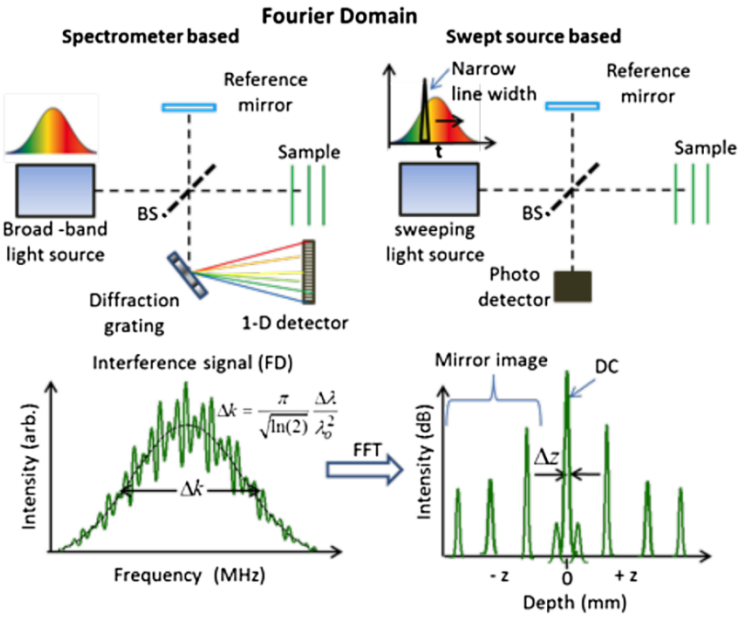

Figure 1.3.1 Schematic Fourier domain optical coherence tomography.

FD-OCT systems can be divided into spectrometer based and swept-source based systems. Courtery by Drexler, Wolfgang, et al. [7] by Creative Commons Attribution 4.0 Unported License.

In the basic SD-OCT system, which typically employs a Michelson interferometer, incident light (E_{in}) is split into reference (E_r) and sample (E_s) arms, with the resulting detected light (E_{out}) processed to produce a whole A-scan.[19,23]

The incorporation of a spectrometer in the FD-OCT system significantly improves image acquisition speeds, achieving A-scans rate up to hundreds kHz. Furthermore, the light source with a broader bandwidth enhances the axial resolution of the images, ranging from 10 μm down to an impressive 1 μm. [24] These advancements not only yield higher signal-to-noise ratios (SNR) but also enable FD-OCT to capture dynamic physiological processes, such as in vivo blood flow, making it highly effective for applications like OCT angiography.[9,25]

The technological advances inherent in SD-OCT, have markedly advanced the capabilities of OCT imaging. Clinicians are now able to obtain not only static images of tissue microstructure but also dynamic information that is crucial for diagnosing and monitoring various medical conditions. As such, FD-OCT remains a pivotal tool in medical imaging, especially in low-cost settings, offering detailed images into the intricate structures of biological tissues and their functional dynamics.

Swept-Source Optical Coherence Tomography (SS-OCT)

Swept-source optical coherence tomography (SS-OCT) represents the new generation of FD-OCT that uses a different approach to capturing coherence information.[26,27] Unlike SD-OCT which utilizes a spectrometer and line detector, SS-OCT utilizes a tunable laser source that sweeps its wavelength over time to scan the biological tissues, which are then detected by a photo detector. This allows for the direct measurement of light echoes from different tissue depths as the wavelength changes. This setup significantly reduces the complexity and potential alignment issues associated with spectrometer-based systems. [7,19,27]

The detection in SS-OCT is based on the interference of light waves that are continuously recorded as the laser sweeps across its wavelength range. The interference signal's intensity varies depending on the match between the optical path lengths in the sample and reference arms, akin to other OCT techniques as illustrated in Figure 1.3.1. However, the use of a swept laser source enhances the system's sensitivity and speed, allowing for deeper penetration into the tissue and faster data acquisition rates.[28]

The swept laser source enables very fast A-scan rate up to MHz [29–31] and long ranging distance up to several meters [32,33]. The fast scanning rate of SS-OCT not only allows for wide field of view (FOV) volumetric data acquisition but also is crucial for reducing motion artifacts in imaging, particularly important in clinical settings where patient movement can be unpredictable. This capability makes it ideal for comprehensive imaging of large organs or tissue sections, and for dynamic studies where rapid data acquisition is critical.

Another primary advantage of SS-OCT is its deeper tissue penetration. This capability is due to the longer wavelength (1060nm, 1300nm, 1700nm etc.) used by the swept laser, which can penetrate deeper into scattering media.[17,34] Moreover, SS-OCT systems often exhibit a more gradual sensitivity roll-off due to the tunable laser can maintain a more uniform spectral output over a broader range of frequencies and the high sampling resolution of the digitizer.[19,27] This results in higher SNR, especially in deep tissue. This makes SS-OCT particularly useful for imaging deeper, denser anatomical structures such as the choroid and sclera in the eye. [8]

The evolution of SS-OCT is driven by advancements in laser technology and detection systems which enable the visualization and measurement of previously inaccessible details. This development represents a significant step in the capabilities of OCT, providing researchers with a powerful tool for deeper, faster, and more detailed imaging of biological tissues.

1.4 Optical coherence tomography angiography (OCTA)

Optical coherence tomography angiography (OCTA) is an advanced imaging technique that builds upon the capabilities of traditional OCT by enabling the visualization of blood flow within tissues without the need for invasive dye injections. This capability is achieved by exploiting the motion of red blood cells (RBCs) within blood vessels as an intrinsic contrast agent.[35–38]

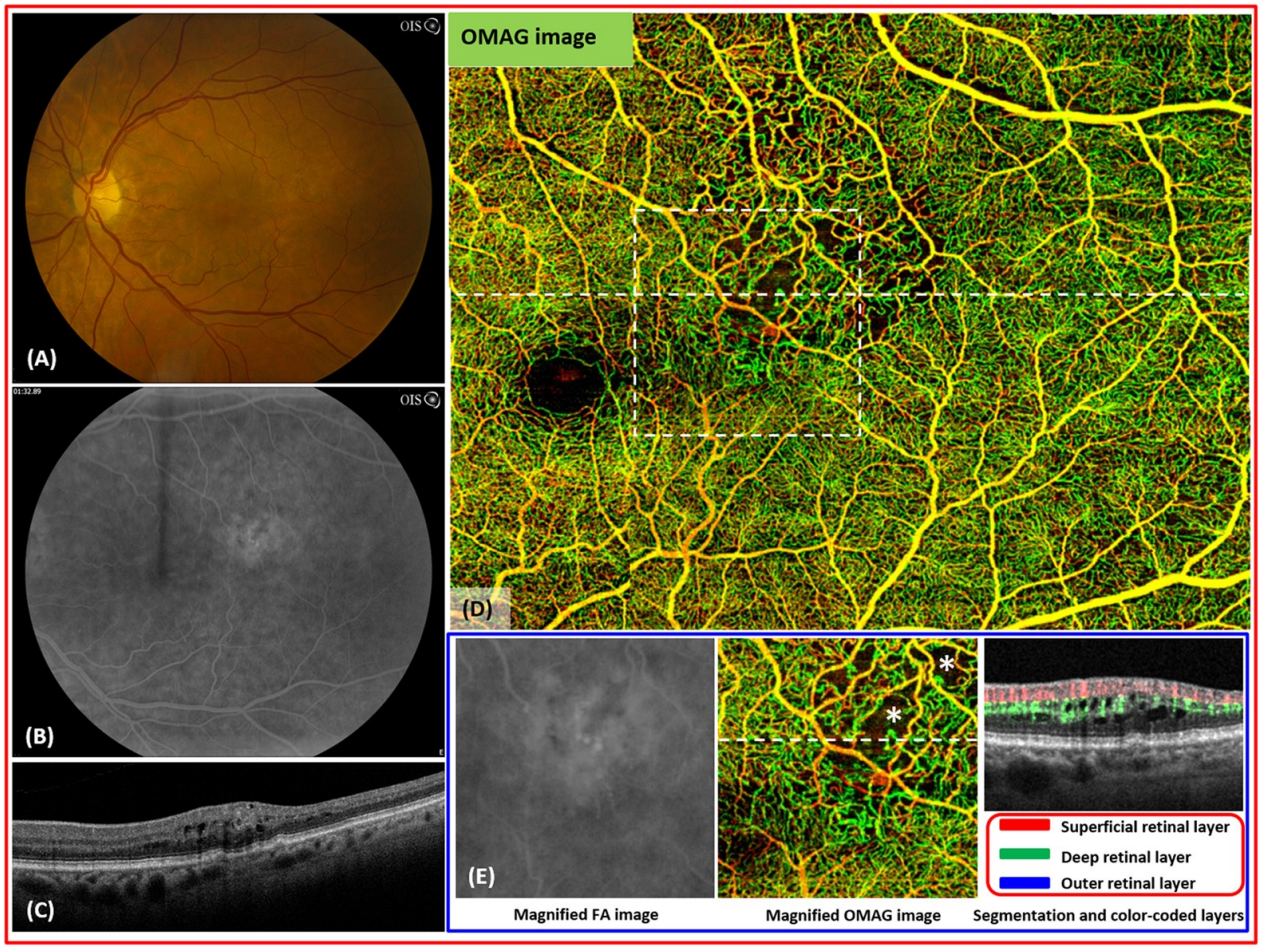

Figure 1.4.1 Imaging of branch retinal vein occlusion (BRVO) in the left eye of a 68 year-old female.

(A) the fundus photo of the left eye shows several hemorrhages and edema in the superotemporal macula. (B) the arteriovenous phase of the fluorescein angiography shows leakage in the area of the BRVO. (C) the optical coherence tomography shows intraretinal fluid. (D) the whole retinal layer optical OMAG image illustrates a large area of capillary dropout and vascular irregularity in the superotemporal macula. (E) the flow image shows the evidence of interrupted flow within the deep retina layer associated with cystoid macular edema (*). Courtery by Zhang, Qinqin, et al [13] by Creative Commons Attribution 4.0 Unported License.

The fundamental principle of OCTA is the detection of variations in the OCT signal that occur due to the movement of particles, such as RBCs, within the blood vessel. The OCT signals from static tissue components remain constant over time, while signals from areas with flowing blood change dynamically due to the movement of RBCs.[38,39]

To capture OCT signals at the same spatial location but at different time points, a specialized scanning protocol called M-scan is widely used in OCTA. This protocol scans the same cross-sectional (B-scan) with

certain time intervals which match the moving speed of RBCs. By analyzing these temporal changes, moving particles can be distinguished from static tissue, allowing for the generation of angiograms that map the blood flow within the tissue. The OCT signal is inherently complex, incorporating both amplitude and phase information. Thus, various OCTA algorithms leverage different aspects of these signal components to extract the high frequency information about blood flow based on intensity [40,41], phase [42,43] or complex signal [35–37,44].

The development of OCTA algorithms has optimized the detection and visualization of dynamic blood flow. [45] These have proven to be both practical and valuable in various clinical and research settings, enabling the visualization and quantification of vascular structures and functions without the risks associated with traditional dye-based angiography. In this thesis, eigenvalue decomposition (ED) based OCTA algorithms are used, demonstrating the versatility and potential of OCTA as a tool for non-invasive vascular imaging in medical diagnostics and treatment monitoring. [37,44]

1.5 Current status and challenge in eye imaging

The application of OCT in ophthalmology has dramatically transformed the diagnostic approach to numerous eye diseases. It is particularly effective in the diagnosis and management of conditions such as glaucoma, retinal vein occlusion, diabetic retinopathy (DR), and age-related macular degeneration (AMD). [46–50] Despite these advancements, several challenges remain, particularly in improving the field of view (FOV), addressing motion artifacts, and biomarker segmentation and quantification.

Motion artifacts present a significant challenge in OCT and OCTA imaging, particularly due to involuntary patient movements such as respiration and heartbeat, as well as eye movements like drift, tremor, and saccades.[16] These artifacts can lead to image distortions, reduced SNR, and compromised image quality, which in turn affect the accuracy and repeatability of microvasculature quantification. [15]

The resolution of OCT imaging has seen significant improvements over the years, with modern commercial devices achieving axial resolutions of around 6 μm and lateral optical resolutions of approximately 20 μm in the tissue. However, maintaining high resolution across a wide field of view remains a challenge. Commercial OCT devices (e.g. Zeiss Cirrus, PLEX Elite, Heidelberg Spectralis) are now capable of acquiring 6×6 mm or 12x12 raster scans, which are essential for comprehensive assessments of macular, but increasing the field of view without compromising resolution requires further technological innovation.

OCT has revolutionized our ability to image the retina and choroid, but the development of accurate and automated algorithms to measure the retinal and choroidal layers, as well as other biomarkers, have lagged behind the technical advancements that have led to improvements in image quality [8,38,51–53]. With increased

imaging speed, scanning density, averaged B-scans, and longer wavelengths, OCT imaging now allows for wider and deeper scans with improved image quality. However, accurate algorithms that segment anatomic layers beyond those layers that display a distinct relative signal intensity, such as the internal limiting membrane (ILM) and retinal pigment epithelium (RPE), remain an ongoing challenge for OCT developers and manufacturers. Deep learning algorithms have been a useful alternative strategy for improving the segmentation of retinal and choroidal layers, but these strategies are unique for specific instruments and scan patterns and cannot be easily used across platforms without additional intensive supervised retraining [48,54–60]. However, even these strategies have their own limitations in identifying subtle structures, particularly those associated with decreased signal intensity at greater depths within the choroid.

The need for improved OCT segmentation strategies is particularly important for the study of AMD. Our understanding of AMD has relied traditionally on the use of color fundus imaging (CFI), fundus autofluorescence imaging (FAFI), and intravenous dye-based angiographic imaging using fluorescein and indocyanine green; however, more recently, OCT and OCTA imaging have become the gold-standards for diagnosing and following disease progression in AMD, both in the clinics and in clinical trials [47,61]. Since AMD causes both anatomic and angiographic changes in multiple layers throughout the macula, OCT is ideally suited to detect and monitor these changes in the retina, the RPE, Bruch's membrane (BM), choriocapillaris (CC), and choroid [62]. Based on fundus exam and color fundus imaging, AMD has been classified into three progressive stages that can be easily translated into OCT-defined stages [46] for which the ability of OCT to image choroid is required. Quantifying AMD biomarkers, such as drusen, hyperreflective foci (HRF) [63], geographic atrophy (GA) [54], and choriocapillaris flow deficits (CCFDs) [64–66], is another area of ongoing research. Drusen, extracellular deposits between the RPE and Bruch's membrane, are early indicators of AMD [67]. Advances in OCT have enabled the detailed imaging of drusen, allowing for the differentiation between types of calcifications and their impact on disease progression. HRF, associated with cellular migration and aggregation within the retina, are crucial markers for the progression from intermediate to late AMD. [68] GA, a hallmark of late-stage AMD, is characterized by the loss of photoreceptors, RPE, and CC. Accurate grading of these lesions is vital for disease monitoring and treatment evaluation. Novel algorithmic approaches using optical attenuation coefficients (OACs) have been developed to enhance the contrast of these lesions in OCT images, facilitating precise localization and quantification. [57] This automation reduces the labor-intensive nature of manual image analysis and improves the reliability of biomarker assessments.

1.6 Scope of the thesis

This thesis aims to expand the capabilities of OCT and OCTA through the development of novel algorithms that improve image quality and usability, automate the detection and quantification of disease biomarkers for clinical applications. Each chapter is dedicated to addressing specific challenges associated with these technologies.

Chapter 2 introduces advanced image processing algorithms aimed at refining OCT and OCTA image quality. It covers innovations in three-dimensional registration and averaging techniques designed to mitigate speckle noise and correct distortions in widefield montage images. These enhancements are pivotal for advancing the diagnostic capabilities of OCT and OCTA in eye imaging, making these tools more effective and reliable.

Chapter 3 shifts the focus towards applying OCT to understand and quantify the biomarkers associated with Age-related Macular Degeneration (AMD), a leading cause of vision loss among the elderly. This chapter delves into the distinctions between different types of drusen and the detection of macular atrophy, illustrating how OCT can be instrumental in identifying and monitoring the progression of AMD.

Chapter 4 introduces automated detection techniques for AMD biomarkers using OCT and OCTA imaging, integrated with deep learning models. This chapter highlights the development of algorithms for automatic segmentation of geographic atrophy (GA) and the quantification of hyperreflective foci (HRF), which are critical for assessing the stage and the progression of AMD. These automated techniques improved utilization of OCT and OCTA for ophthalmic diagnostics, offering tools that could potentially benefit clinical workflows and patient monitoring.

The final chapter of the thesis summarizes and concludes the research, and proposes future directions based on what has been achieved. The goal is to develop powerful imaging tools reach their potential in enhancing diagnostic accuracy, guiding treatment decisions, and ultimately improving patient outcomes in ophthalmology and beyond.

Chapter 2. Optimizing OCT Image Quality and Usability through Robust Image Processing Algorithms

This chapter focuses on improving the image quality of optical coherence tomography (OCT) and optical coherence tomography angiography (OCTA). As OCT and OCTA continue to become integral tools in clinical practice and research, their application has expanded beyond ophthalmology to include dermatology, otolaryngology, and cardiology. However, despite their widespread applications, challenges remain in ensuring the quality of the images produced, which are critical for accurate diagnosis and effective treatment planning.

Section 2.1 focuses on addressing the inherent limitations of OCT and OCTA, such as speckle noise and motion artifacts, which significantly affect image quality and measurement reliability. A robust method for three-dimensional registration and averaging of OCTA scans is presented. This approach is designed to effectively align and average multiple volumes, mitigate noise and artifacts caused by patient motion, and thereby improve the signal-to-noise ratio (SNR). The proposed technique promises not only to improve image quality, but also to preserve the integrity of microvascular quantification, which is essential for accurate quantification.

Section 2.2 addresses the challenges associated with OCTA distortion, particularly in widefield montage images, which are critical for obtaining comprehensive views of vascular networks. The distortion inherent in larger scan areas can significantly impact the accuracy of these images. This section presents innovative methods for correcting the field and radial distortions that are prevalent in extended OCTA scans. By refining these correction techniques, the chapter aims to standardize OCTA image quality, making it a more reliable tool for diagnosing a wider range of pathologies.

Chapter 2.1 Robust three-dimensional registration on optical coherence tomography angiography for speckle reduction and visualization

2.1.1 Introduction

Optical coherence tomography (OCT) is a non-invasive and three-dimensional (3D) biomedical imaging technique that can provide cross-sectional images of a tissue sample with micrometer level resolution [61,69]. OCT has been proven clinically useful in ophthalmology and is gradually becoming the gold standard for the diagnosis of many retinal diseases [12,61,69,70]. Recently, OCT angiography (OCTA) has emerged as a novel non-invasive tool that can visualize functional blood vessels down to capillary levels in clinical

settings [35,64,65]. The capabilities of OCT and OCTA have made revolutionary impact on how ophthalmologists understand ocular disease pathologies as well as manage the therapeutic treatments. In addition to the rapid translation of OCTA into clinical ophthalmology, it has also been shown increasing promises in the fields of dermatology [71], otolaryngology [72], dentistry [73] and cardiology [74].

Despite their increasing popularity, OCT and OCTA still face several challenges in terms of the image quality for the purposes of providing more accurate quantification information. The motion artifacts and the inherent speckle noise from imaging process would significantly compromise its image quality, thus affect the accuracy and repeatability of microvasculature quantification [75,76]. Previous method has suggested that multiple-volume or repeat B-scan averaging strategy can compensate motion artifacts and reduce speckle noises [65,77,78]. This method requires spatial alignment of the repeated scans or volumes before performing averaging. In practice, subjects are often in motion, albeit small, during scanning. The motion, including but not limited to the respiration and heartbeat that are not inevitable, would introduce misalignment in the OCT raster scans during the process of averaging. Specifically, in dermatological OCT imaging, the inter-frame motion artifacts and global movement would corrupt the alignment of the repeated successively acquired volumes. Thus add the difficulties to perform multi-volume averaging to enhance the image quality and clarity for the purpose of quantification. Also in ocular imaging, eye motions, such as a slow shift in gaze (drift), high frequency involuntary motions (tremor), or rapid eye movement (saccades), can all lead to disconnected vessels and introduce stripes of motion artifacts, affecting our ability to provide quantitative measures of retinal vascular complex.

Therefore, the key to a successful averaging algorithm is the accurate spatial registration and alignment. Several methods have been proposed for 3D registration in OCT or OCTA for specially-designed system configurations [79] using post-processing algorithms[80]. Tracking and compensation strategies have also been proposed and utilized to mitigate the subject motion artifacts, such as with an aid of scanning laser ophthalmoscopy [81] and using wavefront sensors [82]. However, these prior approaches usually either require expensive and sophisticated system setup, or increase the total acquisition time that inevitably reduces patient compliance. Other than the hardware approaches mentioned above, software processing algorithms can also be used to reduce speckle noise and motion artifacts. Generally, one can register multiple repeated OCT volumes to mitigate the above mentioned issues and enhance the signal to noise ratio (SNR). Ideally, the OCT signals sampled at the same spatial location with sufficient time interval are correlated. As a result, the averaged signal of repeatedly sampled signals improves the SNR by suppressing the random fluctuating noise while maintaining the true signals [39]. Potsaid et al. [83] proposed a method of two dimensional (2D) registration on cross-sectional images to correct the volumetric motion, but it is computationally cost on 3D images. In addition, this method was only designed for correcting motion between slow scans. Kraus et

al. [14] introduced a method with orthogonal scanning pattern that uses intensity based registration to minimize the motion artifacts in the OCT system. This method combines the information of fast and slow scans to register and acquire the artifact-free images. Although it has been adopted in commercial OCT systems (e.g. Optovue SD-OCTA machine), it still suffers from residual inter-frame artifact when large inter-volume mismatch exists. The requirement of a special scanning pattern for this algorithm also increases the difficulties for it to be adapted by other commercial OCT systems.

Moreover, layer segmentation [84–87] or feature extraction approaches [88] have also been presented to guide the volumetric registration, such methods can correct global displacement of each sub-image or align the image based on the layer contour before co-registration. However, the robustness of such algorithms may decrease when the pathological cases are dealt with, and they tend to induce unpredictable registration errors. Therefore, there is still a demand to develop a registration and averaging method that can perform universal 3D registration on repeated OCT volumes using reasonable computation resources, without a need to modify the hardware configurations of current commercial OCT systems.

In this study, we propose a robust and comprehensive approach to register 3D OCT and OCTA volumes for speckle noise reduction, where successive OCT volumes are used to obtain the affine and B-spline transformations, upon which to obtain the coordinates of OCTA volumes for later co-registration and averaging. We demonstrate that this method can significantly increase the SNR of images and suppress motion induced artifacts, through testing the algorithm on the datasets acquired from human retina and human skin *in vivo*.

2.1.2 Methods

The workflow of 3D registration and averaging

In the registration model below, the images that are acquired when the sample is in motion are defined as I_M and the fixed image that acts as the reference is referred to as I_F. For any pixel located at x, the spatial transformation matrix T that aligns I_F to I_M is defined as :

$$T(x) = x + u(x) \tag{2.1.1}$$

where $u(x)$ is the amount of motion, or the displacement due to global or local motion between coordinates. Note that the spatial location can be of *(x,y,z)* coordinates in 3-D, here we use *x* for simplicity. Generally speaking, the intensity-based registration is a convex optimization problem that can be represented by the equation below, to obtain the correct spatial transformation.

$$\hat{T} = argmin\ C\left(T_{\boldsymbol{\mu}}; I_F, I_M\right) \tag{2.1.2}$$

In Eq(2.1.2), $\hat{T}$ represents the optimized transformation under the cost function C, which measures the deformation between the reference and registered image. Thus, the goal of image registration is to search for the best parameters vector $\boldsymbol{\mu}$ for the transformation $T_{\boldsymbol{\mu}}$ from I_F to I_M with a minimum cost. The number of parameters in vector $\boldsymbol{\mu}$ defined by the transformation matrix T. There are 12 parameters in vector $\boldsymbol{\mu}$ for affine transformation and $(\boldsymbol{P_x} \times \boldsymbol{P_y} \times \boldsymbol{P_z}) \times \mathbf{3}$ parameters for B-spline transformation, where $\boldsymbol{P_x}$, $\boldsymbol{P_y}, \boldsymbol{P_z}$ are the number of pixels in each dimension divided by the designed grid, which is 16 pixels in this study.

The cost function C here is formed by the mutual information (MI) term with the penalty term, as:

$$C[\mu; I_F, I_M] = -\alpha MI + \beta \boldsymbol{P}[\mu; I_M] \tag{2.1.3}$$

where α, β are user-defined parameters, with empirically set as 1.0 and 0.1 respectively. $\boldsymbol{P}[\mu; I_M]$ is a penalty term to reduce overfitting and to constrain the transformation matrix $T_{\boldsymbol{\mu}}$, which is modified from the rigidity penalty method introduced by Staring et al. [89]. MI is defined as below:

$$MI(\mu; I_F, I_M) = \sum_m \sum_f p(f, m; \mu)\, log_2 \left(\frac{p(f, m; \mu)}{p_F(f) p_M(m; \mu)} \right), \tag{2.1.4}$$

where p is the discrete joint probability, and p_F and p_M are the marginal discrete probabilities of the reference and moving images, obtained by summing p over moving images m and the reference image f, respectively. The joint probability p is estimated using B-spline Parzen window described by Thevenaz [90]. The MI depends on fewer assumptions of data and can provide better stability for optimizations comparing L_1, the Manhattan distance or L_2 , the Euclidean distance.

In the optimization of the parameters vector $\boldsymbol{\mu}$ for the cost function, we employed a method called adaptive stochastic gradient descent (ASGD) method. This algorithm randomly shuffles the datasets to calculate the gradients, updating the parameters with less variance to produce a more stable convergence. It also requires fewer parameters to be set and tends to be more robust by its adaptive step size. Mathematically, the ASGD can be represented as:

$$\begin{aligned} \mu_{k+1} &= \mu_k - \gamma(t_k) g_k \\ t_{k+1} &= \max\left(t_k + S\left(-g_k^T g_{k-1}\right), 0\right) \end{aligned} \tag{2.1.5}$$

where $\boldsymbol{\mu_k}$ denotes the registration parameter vector for optimization, $\gamma(t_k)$ denotes the step size and g_k denotes the gradient of the cost function at step k. The learning rate is defined by a monotone decreasing function γ [91] and controlled by the incremental variable t_k. In the determination of t_k, S represents the sigmoid function to normalize the inner products of the gradients of previous two steps [91]. If the directions of the gradients g_k, g_{k-1} are same, the positive inner product of gradients will result to a small t_{k+1} and a

larger step size $\gamma(t_{k+1})$. Eq(2.1.5) illustrates that the ASGD method implements an adaptive step size mechanism through adjusting the independent variable t_k of step size $\gamma(t_k)$. The optimization starts with zero initiation of $\boldsymbol{\mu_0}$, and the images are further sampled for calculating the cost function. At next step, $\boldsymbol{\mu_1}$ is updated according to Eq(2.1.5). Then the algorithm will update the $\boldsymbol{\mu_k}$ iteratively until reaching the predefined step number, which was set as 250 in this study. To summarize, the ASGD method (Eq (2.1.5)) was used to update the transformation vector $\boldsymbol{\mu}$ and to minimize the cost function Eq(2.1.3) until desired vector $\boldsymbol{\mu}$ is found.

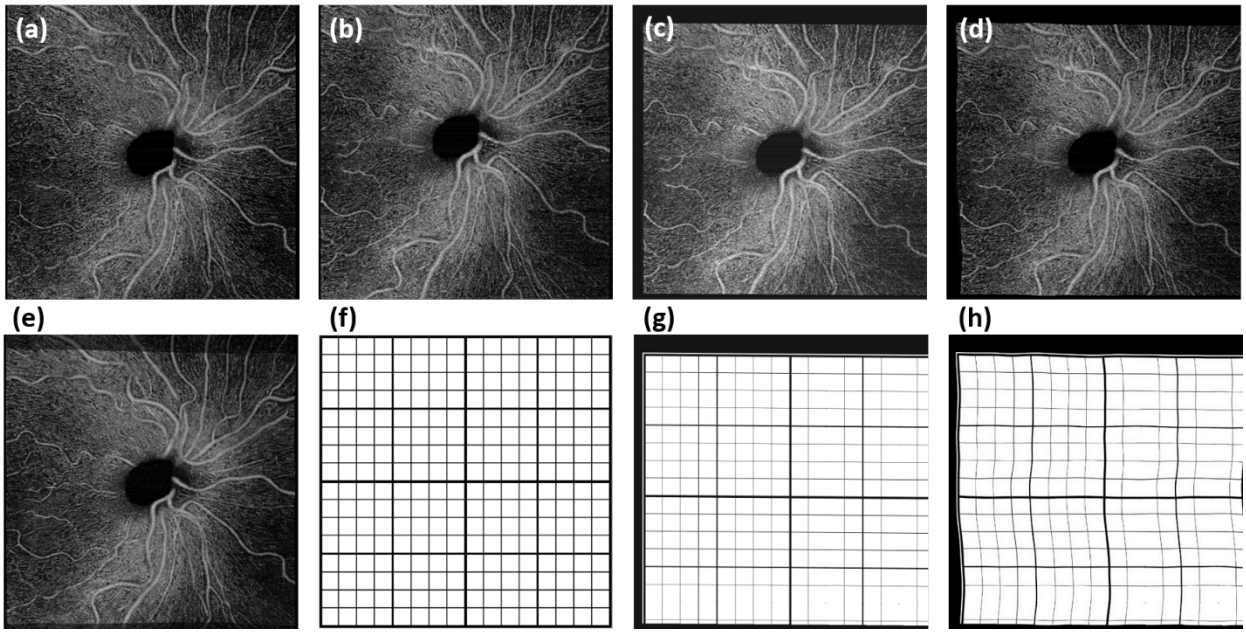

Figure 2.1.1. An illustration of the correction of affine and B-spline registration on 2D images.

(a) is the reference image and (b) is the moving image. (c)(d) are the images registered by affine and B-spline transformation, respectively. (e) is the final averaged image. The mesh (f-h) visualize the deformation that corresponding to (b-d). The affine transformation corrects the global motion and the B-spline improves the local alignments.

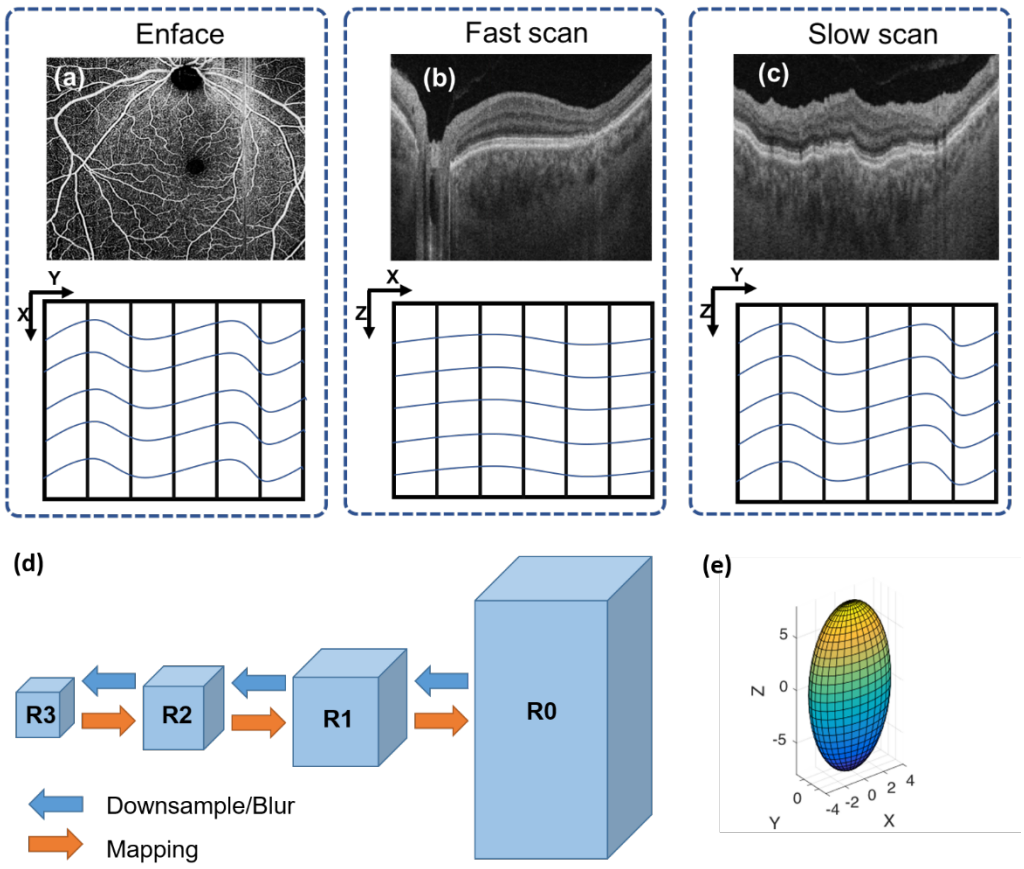

Figure 2.1.2. The illustration of anisotropic deformation and multi-resolution down-sampling approach using 3D OCT retinal image $a(x, y, z)$ as an example due to patient movement during image capture.

(a) Illustration of the resulting deformation of 3D retinal image, $a(x, y, z)$, at a certain depth slice of z, $a(x, y)$. (b) B-frame at fast scan axis, $a(x, z)$, with minimal distortion. (c) B-frame along slowest scan axis, $a(y, z)$, with severe disortion due to the longer time interval. (d) The anisotropic down sampling and multi-resolution approach for 3D registration. R0 is the original resolution volume and R1-R3 are down sampled volumes. The low resolution volumes are downsampled from higher resolution images as indicated by the blue arrows. The registration matrices are applied to high resolution volumes, as shown by the orange arrows. (e) The anisotropic Gaussian kernel is used to acquire the low resolution volumes, which is largely dependent on the imaging speed of the system, where the kernel ellipse is most elongated at the fastest direction (i.e. A-scan) and most compressed at the slowest direction (i.e. C direction). X denotes the fast scan axis (B-scan), Y the slowest axis (C-scan), and Z the fastest scan axis (A-scan).

We utilized two approaches in our registration model. Firstly, we employed both affine and B-spline models to obtain the transformation matrix T. The affine transformation was designed to correct translation, scaling, shear, and rotation of the images, also known as global correction of relatively large movement [84,85] . Afterward, we used the B-spline transformation to correct the free-form deformation, also known as irregular movement and local deformation correction [84,85] as shown in Figure 2.1.1. Secondly, we performed

registration on different resolution levels iteratively in order to refine and minimize misalignments between 3D volume scans. Specifically, a range of Gaussian kernels were used to down sample OCT scans in a particular fashion to reduce the complexity and the amount of data. As illustrated in Figure 2.1.2, the original OCT scan R0 with highest resolution was down sampled to R1 and then further down sampled to R2, R3, and so on [92]. The image size and resolution were decreased to form the image pyramids. The down sampling Gaussian kernel $\sigma(x, y, z)$ was set with a size of $(2, 4, 8)$ for the image pyramids and this was specifically designed to match the anisotropic motion patterns in OCT scans. In $\sigma(x, y, z)$, z corresponds to the A-line direction, x corresponds to the B-scan direction (fast scan) and y corresponds to the C-scan direction (slow scan). The A-line acquisition speed is the fastest, with the least motion artifacts, and thus, down sampled the most (8 times). The C-scan acquisition speed is the slowest, with the highest probability to have motion artifacts, and consequently, down sampled the least (2 times). The down-sampling for the B-scan is in between. For each image pyramids, the registration process was first conducted on R3 as the optimization had better convergence on blurred images. Then the resulted parameters from R3 were applied and mapped back on R2-R0, as indicated by the orange arrows of Figure 2.1.2. Specifically, the affine transformation calculated by R3 was firstly applied onto R2 globally, then the B-spline transformation calculated by R3 on each grid was applied onto corresponding pixels on R2. The registration on R2 was then conducted on the modified images with less movements and its results were further applied to R1 and R0. The registration and mapping process were iteratively performed until R0 was reached.

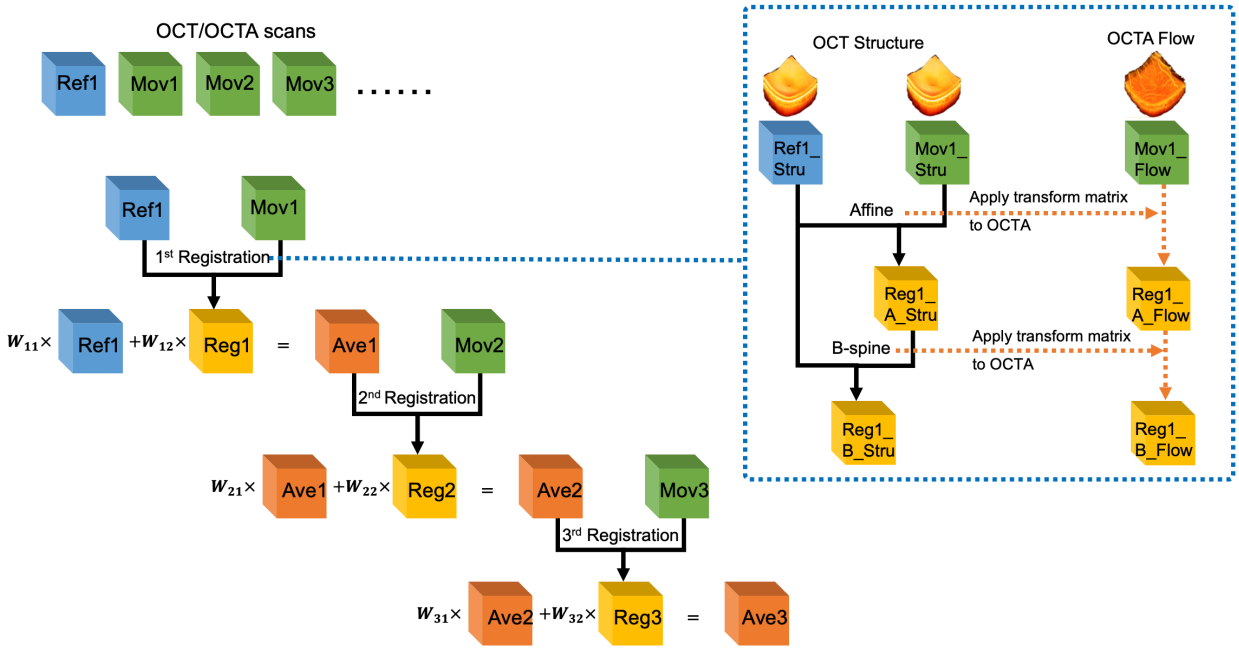

Figure 2.1.3. The Workflow of 3D volumetric registration.

For the consecutive 4 scans, the first OCT and OCTA volumes are set as the reference volumes as Ref1 and the following scans Mov1, Mov2, Mov3 are to be registered. Firstly, the 1st registration is first to register the Mov1 to the Ref 1 as illustrated in the right-side box, where 1) the affine transformation matrix is generated to correct the bulk motion between Ref1_Stru with Mov1_Stru; and 2) The B-spline transform is calculated between Ref1_Stru and Reg1_A_Stru to correct the local movements. The transformation matrices from the structural volumes are directly applied to the corresponding flow volumes. Then, the average volume Ave1 is calculated from Ref1 and Reg1 by the weight $W_{11} = 1/2, W_{12} = 1/2$. Secondly, for the 2nd registration, the new reference volume is assigned as Ave1 and the registration procedures are similar to the first step. The weights W_{21}, W_{22} are calculated from Eq (2.1.5), i.e., 2/3, 1/3. Thirdly, the 3rd Registration is similar to step 2, with the updated new weights $W_{31} = 3/4, W_{32} = 1/4$.

After registration, the registered image was weighted and averaged with the reference image, which was then assigned as the new reference image for next round of registration as it has better contrast. The weighted averaging process for n_{th} image is defined by the following rules, as shown in Figure 2.1.3.

$$\begin{aligned} I_{ave,n} &= w_{n1} I_{Fix,n} + w_{n2} I_{Reg,n} \\ \mathrm{I_{Fix,n+1}} &= \mathrm{I_{ave,n}} \end{aligned} \tag{2.1.6}$$

For n_{th} registration, the designed weights ensure each individual image has the same weight $1/n$ in the final averaged results. We set the $w_{n1} = n/(n+1)$ as the weight for the reference image and the $w_{n2} = 1/(n+1)$ as the weight for the registered image. $I_{Fix,n}$, $I_{Reg,n}$ represent the corresponding reference image and registered image, respectively. In our study, all registrations were conducted on the OCT scans. Since OCT and OCTA datasets share the same spatial coordinates, transformations calculated from the OCT scans were stored and directly applied to OCTA scans as shown by the dash arrows of Figure 2.1.3. The implementation of the registration program was based on MATLAB (MathWorks, R2016a) and an open source project Elastix [93].

Data acquisition

Two datasets were collected to test the proposed algorithm: human skin data using a laboratory built SS-OCT 1310nm system [15] and human retina data acquired by a 1050nm swept-source OCT angiography (SS-OCTA) (PLEX® Elite 9000, Carl Zeiss Meditec, Dublin, CA). Both systems have an imaging speed of 100 kHz. The subject imaging followed protocols reviewed and approved by the Institutional Review Board of Medical Sciences Subcommittee at the University of Washington, Seattle. The tenets of the Declaration of Helsinki and Health Insurance Portability and Accountability Act were followed. Informed consent forms were obtained from all subjects before participation.

For the human skin data acquired by the laboratory system, 10 consecutive OCT volumes with 9x9mm scanning pattern were acquired from each subject. Each volume had a total of 2400 B-scans with four repeated B-scans at each spatial B-location for the purpose of OCTA. Each B-scan had 600 A-scans. No tracking mechanism was employed in this system and the acquisition of 10 volumes took ~180 seconds for each subject in total. For the human retina data acquired by the commercial SS-OCTA device, 22 repeated 6x6 mm volume scans were acquired from the right eye of each subject. Of these 22 volume scans, 11 scans were acquired centered at the fovea and 11 scans were acquired ~9 mm inferonasally away from the fovea. Each scan takes about ~6 seconds and short breaks were taken between scans. The *Fastrac* motion tracking system was employed to minimize the eye motion during scanning, and the Track to Prior function was turned on to acquire repeated scans at the same location [94]. For both sets of data, the ultrahigh sensitive optical microangiography (OMAG) [36] algorithm was used to generate OCTA volumes and the subpixel registration approach was applied to compensate the displacement between adjacent B-scans [95]. After OCTA volumes were generated, the proposed registration algorithm was employed to register and average both OCT and OCTA data. After obtaining the average OCTA data, a semi-automatic segmentation software [96] was used to extract slabs of interest to demonstrate the quality of the resulting images. Human retina data were segmented into whole retina slab and choriocapillaris slab, following protocols of previously published study [97]. Human skin data were segmented into different slabs for better visualization, following protocols of previously published study [71]. After segmentation, the maximum intensity projection (MIP) was used to generate en face images.

Registration evaluation

To evaluate the performance of resulting registration and subsequent averaging, three parameters were used: peak signal-to-noise ratio (PSNR), normalized correlation coefficient (NCC), and signal to noise ratio (SNR). The PSNR measures the quality of single scans compared with the high-quality averaged images. It is defined as:

$$PSNR = 10 \times \log_{10} \frac{MAX_I^2}{\frac{1}{lmn}\sum_L \sum_M \sum_N (I_H - I_S)^2} \tag{2.1.7}$$

where l, m, n represent the size of the volume, and I represents the intensity of data. The averaged high-quality image was picked as the reference image I_H and the single scan image was denoted as image I_S. MAX_I is the maximum possible pixel value of the image. The whole 3D OCT volumes were used to quantify PSNR.

The NCC measures the similarity of images by assuming a linear relationship between the intensity values of the reference image and the moving image. It evaluates how well the volumes are aligned. The NCC is defined as

$$NCC(\mu; I_F, I_M) = \frac{\sum((I_F - \overline{I_F})\left(I_M\left(T_\mu(x)\right) - \overline{I_M}\right))}{\sqrt{\sum(I_F - \overline{I_F})^2 \sum\left(I_M\left(T_\mu(x)\right) - \overline{I_M}\right)^2}} \quad (2.1.8)$$

The $T_{\boldsymbol{\mu}}(x)$ represents the registered image I_F that is suspected of motion. $\overline{\mathrm{I_F}}$ and $\overline{\mathrm{I_M}}$ are the mean of reference image and moving image, respectively. The whole 3D OCT and OCTA volumes were used to quantify NCC.

The SNR is defined by the ratio of mean to standard deviation of the signal:

$$SNR = \frac{\mu_{signal}}{\sigma_{noise}} \quad (2.1.9)$$

where μ_{signal} is the mean of OCT signal and σ_{noise} is the standard deviation of the background noise. The regions of tissues around the focus position were manually selected as the signal and the regions of no tissues were manually selected as noise floor. Theoretically, the mean of signals from individual samples improves linearly to the repetition N with the standard deviation inversely related to $\sqrt{N}$. Therefore SNR should increase linearly to $\sqrt{N}$ [78].

2.1.3 Results

A total of five healthy subjects with a normal ocular history, no visual complains, and no identified optic disc, retinal, or choroidal pathologies on examination were recruited for human retina imaging and a total of five healthy volunteers were imaged for human skin imaging. To evaluate the performance of proposed algorithm, we examined the cost function at 4 resolution levels during the optimization, inspected visual appearance of the averaged images, and calculated quantitative metrics from averaged images describing image quality.

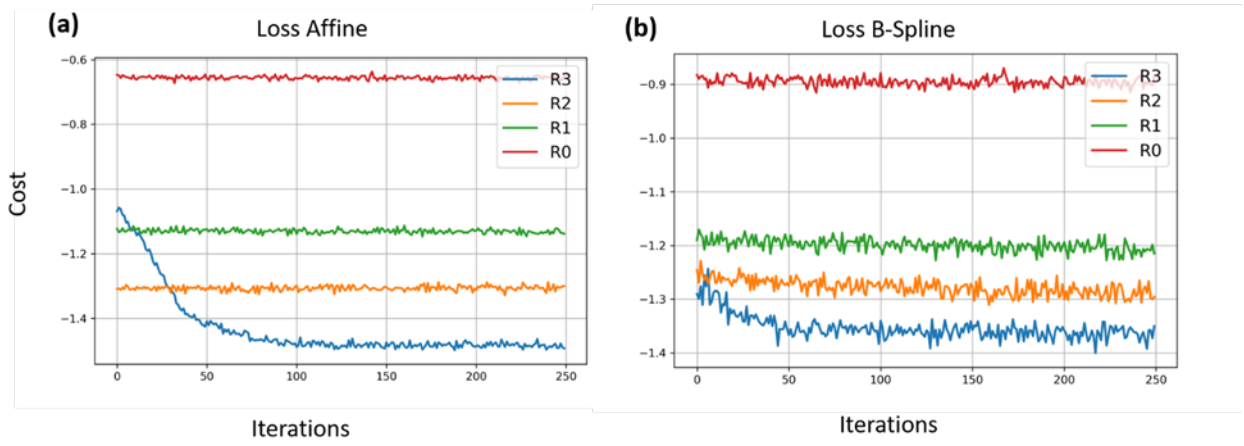

Figure 2.1.4. The evolution of the cost function in registration with the increase of iterations during optimization.

(a) affine and (b) B-spline transformation matrix. The curve with label R0 represents the cost function that used at original resolution during optimization; and labels R1, R2, and R3 represent the cost functions that were using 2x, 4x and 8x down-sampled images, respectively. The differences between images were calculated by mutual information.

As explained in the Methods section, a cost function is commonly used to evaluate the differences of the reference (fixed) image and the image that is to be registered. This function indicates how well the registration algorithm performs. Figure 2.1.4 presents how the cost function changes with the number of iterations during optimizing the transformation parameters. Ideally, the value of the cost function should decrease with the increase of iterations and eventually reach a plateau, from where further increase of iteration would not benefit more the optimization. Figure 2.1.4(a) demonstrates how the cost function varies with the number of iterations for the affine transformation when the optimization was performed on 4 different resolution levels (R3-R0). The cost function decreases relatively fast on the low resolution level (R3), and reaches a plateau at about 100 iterations which would deliver similar performance to that of higher resolution levels (R0-R2). This means the optimal affine registration parameters can be obtained on the low resolution level images. Figure 2.1.4(b) demonstrates how the cost function changes for the B-spline transformation at different resolution levels (R3-R0). The cost decreases relative slowly, but still most significantly in the low resolution level (R3) images. However, unlike in the affine transformation, the value of the cost function is kept on decreasing at higher resolution level images (R1 and R2). That indicates the local movements are progressively aligned by the B-spline registration during the process. The parameter space for affine transformation is much smaller than the B-spline transformation, thus the cost function curves in Figure 2.1.4(a) converges for fewer iterations and on lower resolution level images than in Figure 2.1.4(b). The appearance of cost function provides ground for selecting the number of iterations and the levels of down sampling during optimization. If the cost functions are converged on the lowest resolution

level and keep same at higher levels (like Figure 2.1.4(a)), then the motion of images are not severe. The users can set less iterations and down sampling levels so that the optimization can speed up. Otherwise users can keep the default settings for better registration.

The averaged images suggest its effectiveness for noise reduction and contrast enhancement. Figure 2.1.5 shows an example of single ((a),(c)) and averaged ((b),(d)) OCT((a),(b)) and OCTA((c),(d)) B-scans. These B-scans were taken from 6x6 mm volumes centered at the fovea. Yellow dash lines indicate zoomed-in regions for detailed comparison before and after using the proposed algorithm. Visually, the common appearance of speckle patterns in the single images has been significantly reduced in the averaged images.

Figure 2.1.6 shows another example of human retina data, but located inferornasally to the fovea. Panels (a), (d) and (g) are the enface images of retina, choriocapillaris and OCTA B-scan of a single volume. Panels (b), (e) and (h), panels (c), (f) and (i) are organized the same way as (a), (d) and (g), but from volumes averaged three times and six times, respectively. Visually, the averaged en face images showed smoother vasculature, i.e. better connectivity, better contrast between vasculature and avascular regions. It is particularly evident that the disrupted retinal vasculatures on the single scan image, likely caused by patient movements, were significantly resolved and improved after registration and averaging, as indicated by green arrows.

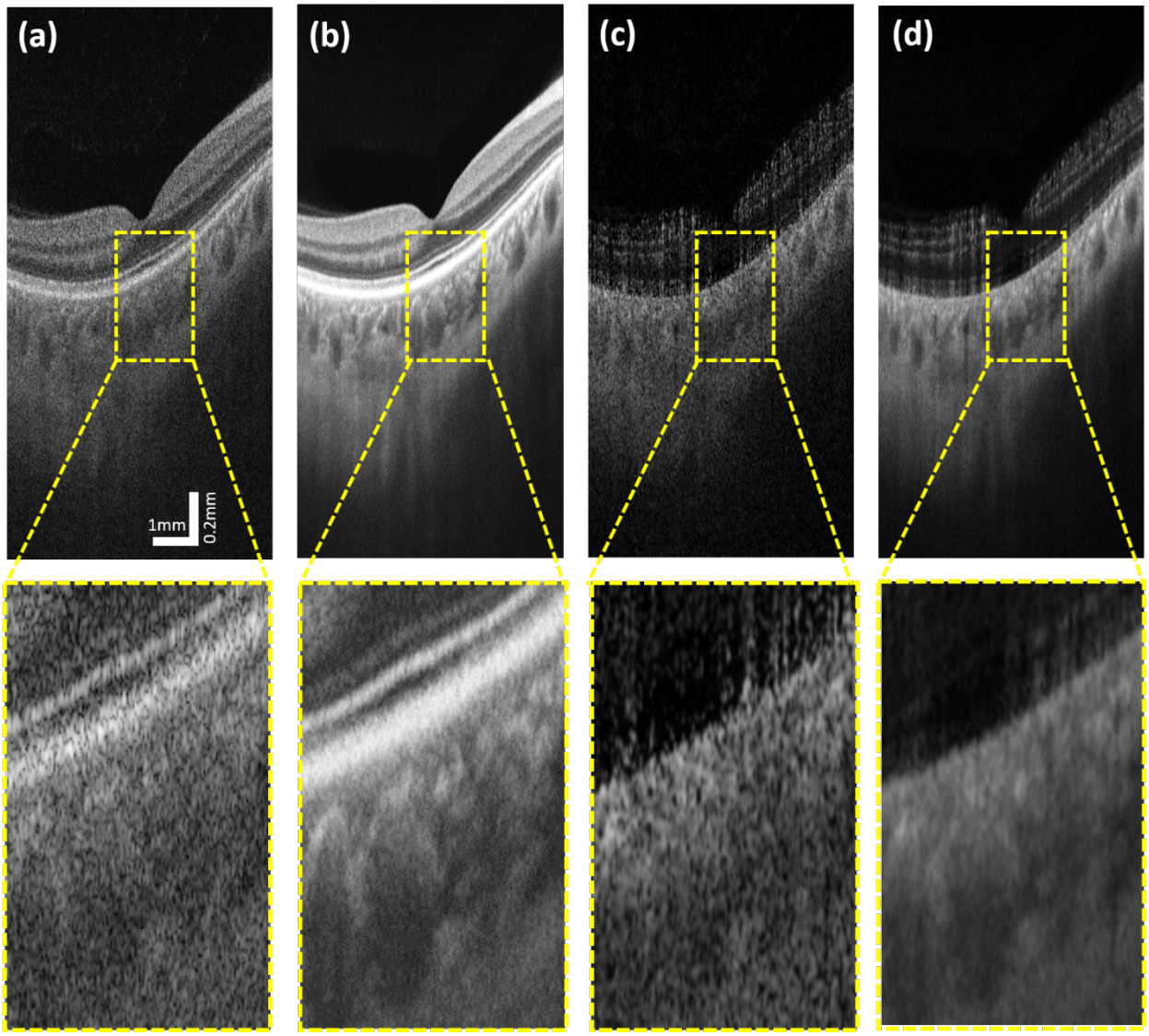

Figure 2.1.5. A comparison of original and noise deducted B-scan OCT images of fovea scan.

(a) typical single OCT B-scan. (b) Corresponding averaged OCT B-scan from 10 repeated volumes. (c) Corresponding single OCTA B-scan image. (d) Corresponding averaged OCTA B-scan from 10 repeated volumes. The zoomed areas show the changes of speckle after registration, indicating the speckle noise is significantly reduced after the registration and averaging algorithm. The scale bars represent 1mm and 0.2mm in lateral and axial dimension, respectively.

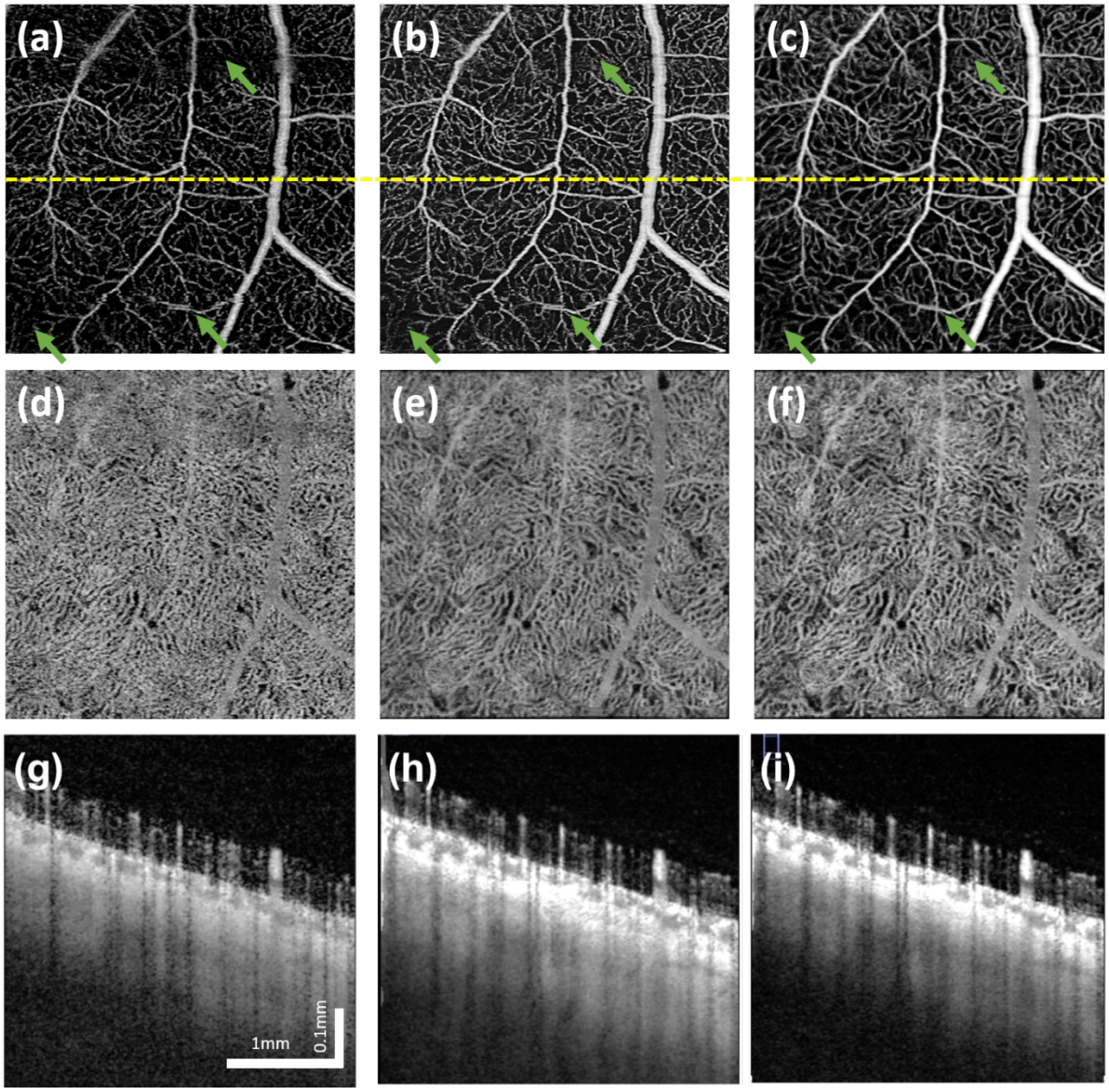

Figure 2.1.6. A comparison of different number of averaging.

Single scan (left column), averaged from 3 repeated volume scans (middle column), and averaged from 6 repeated volume scans (right column). (a-c) The MIP of retinal layer. (d-f) The MIP of choriocapillaris layer. (g-i) The cross-sectional image at the yellow dash line in (a-c). Generally speaking, the OCTA image quality is progressively improved with the increased number of repeated scans, in terms of vessel smoothness, connectivity, and background noise level. The green arrows indicate the regions where there is dramatic enhancement of vessel connectivity after processing. The scale bars represent 1mm and 0.1mm in lateral and axial dimension, respectively.

Apart from the human retina imaging, we have also tested this proposed algorithm on human skin imaging due to the increased usage of OCT/OCTA in dermatology applications. Figure 2.1.7 shows an example of

en face OCTA image before and after registration and averaging. Similar to the human retina data, the averaged en face image shows less speckle noise, higher image contrast and better vascular connectivity. The inter-frame motion artifacts present on the single image (white arrows) have also removed after registration and averaging. Panels (c) and (d) show a zoomed-in region of the whole 9x9 mm scan. It can be visually observed that in the registered and averaged images, the presence of larger vessels from deeper layers (blue) is significantly enhanced compared to the single image. Moreover, the capillaries from superficial layers (yellow) also have a smoother appearance and less noisy.

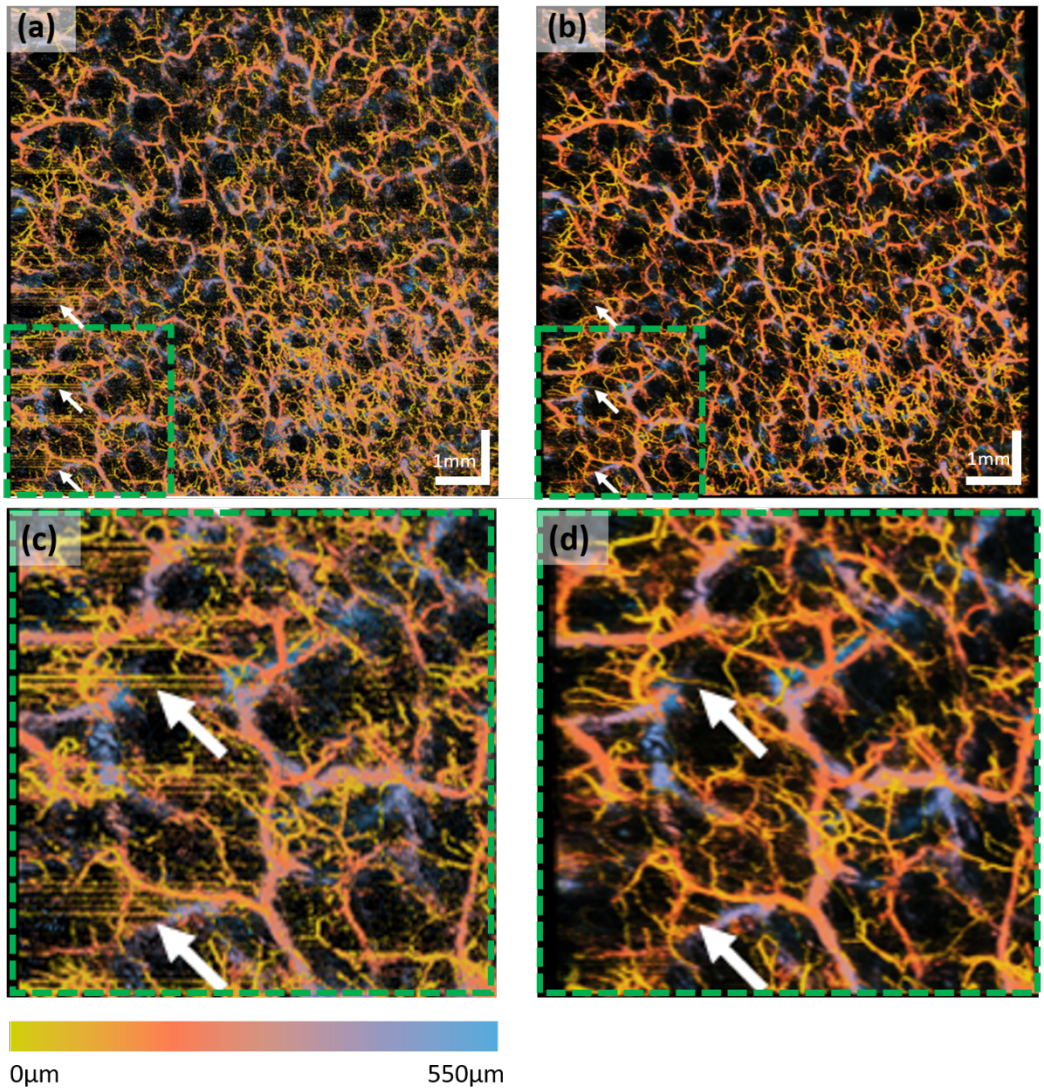

Figure 2.1.7. Illustration of the OCT imaging of skin with volume averaging.

The OCTA en-face projection images are color encoded by vessel depth information from the tissue surface (see color bar). (a) is the color encoded projection of a single volume and (b) is the projection of the averaged result of 10 registered volumes. (c) and (d) are the zoomed views of the green dash regions in (a) and (b), respectively. The speckle noise and the motion noise are suppressed in averaged results as indicated by the white arrows. The connectivity of

vessel has been improved through the averaged image. (b) and (d) also provide cleaner backgrounds and enhance the overall contrast. The scale bar represents 1mm.

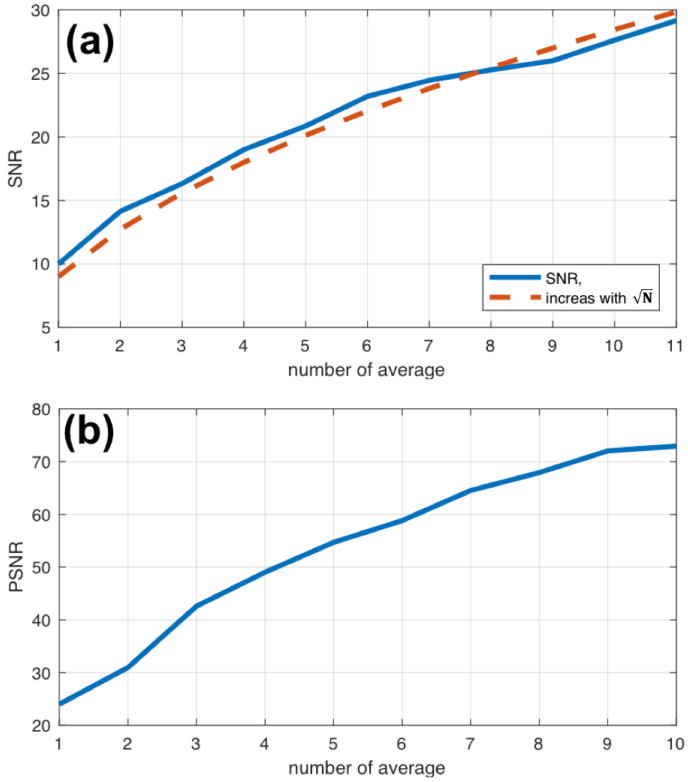

Figure 2.1.8. The performance assessment with the increase of averaging numbers.
(a) SNR and (b) PSNR of OCT structure images increased with the increase of the number of averages. The dashed line in (a) represents the fitting by $\sqrt{N}$ curve

The proposed algorithm works relatively fast. For 3D image registration, it took ~8 minutes to register 2 human skin OCT volumes (600x600x1000) and 6 minutes to register 2 human retina volumes (500x500x1000). For 2D images, it took ~6 seconds to register 2 human retina en face images (500x500). These processing times were assessed on a workstation configured with the Intel Xeon 2630-v3 CPU and 128G RAM.

To evaluate further the performance of the proposed algorithm, PSNR and SNR were calculated using human skin data from all 5 subjects. As explained in the Methods section, there is a linear relationship between theoretical SNR value and the square root of iteration N. Such linear relationship is shown in Figure 2.1.8(a) (the orange dashed line). The experimentally calculated SNR values against $\sqrt{N}$ is shown in Figure 2.1.8(a) (blue line), which agrees well with the theoretical ones. Figure 2.1.8(b) shows the

experimentally calculated PSNR value against the iteration N. 11 registered volumes were used to generate this graph, PSNR describes how similar low quality images (the Ref1, Ave1, Ave2…Ave9 volumes) are to the highest quality image (Ave10 in Figure 2.1.3) base on Eq(2.1.9). The PNSRs over 4 averaged scans with the highest quality image are all over 50dB, which indicates a very high similarity for and an early stop to acquire a high contrast image.

Other than the SNR and PSNR, the NCC has also been calculated using the human skin data. Table 2.1.1 shows the calculated NCC between individual scans on original, Affine, and Affine combined with B-spline transforms. The NCC was calculated for both OCT and OCTA volumes. Notably, the NCC values in OCTA data were lower than that in OCT volumes, this was likely due to the high frequency noise and motion artifacts that existed in the OCTA images, degrading the similarity between volumes.

Table 2.1.1. The normalized correlation coefficient of original images registered images

	Original	Affine Registered	B-spline Registered
OCT	0.3535±0.087	0.5727±0.1463	0.6334±0.1834
OCTA	0.1547±0.0094	0.4381±01202	0.5028±0.1452

2.1.4 Discussion and conclusion

In this paper, we have presented a useful approach for multi-volume registration in OCT/ OCTA, resulting in better averaging and noise reduction that would be useful for quantitative assessment of microvasculature features within tissue beds. The algorithm was designed for compensating the patient motion during and between each individual scans. Specifically, the proposed registration algorithm can minimize the spatial mismatch between repeated 3D scans, and align the volumes by using both affine and B-spline transformation. The affine transformation corrects the bulk motion, i.e. the global movement while the B-spline transformation compensates the local deformation. To increase the accuracy, stability and robustness of the algorithm we have also employed a multi-level resolution approach, in which the registration first starts on low resolution level and then the transformation calculated from lower resolution levels is being progressively applied to higher resolution levels. We have shown that such multi-level resolution approach has the advantage of speeding up the processing, important for in vivo imaging applications. As demonstrated by both retina and skin data, after registering and averaging multiple 3D OCT and OCTA volumes, the proposed algorithm could significantly reduce speckle noise and motion artifacts, yielding higher SNR, PSNR and NCC values.

The proposed registration algorithm has been shown very robust for two main reasons: 1) the combined use of Affine and B-spline strategies, and 2) the multi-level resolution treatments in the registration. We employed the combination of both Affine and B-spline registration after careful considerations of misalignments at the sources between OCT volumes. The Affine registration compensates for the global movement between individual repeated scans due to patient movement. And the B-spline registration aligns the local mismatches due to local movement. Specifically, the movements are the results of the heartbeat, respiration and other deformation of the tissue. The multi-level resolution treatment is specifically designed for considering how the OCT's scanning protocol would influence motion patterns. In the OCT imaging protocol, multiple A-lines are used to form a B-scan and multiple B-scans would form a C-scan (3D volume). Therefore, when scanning a 3D sample, on the A-line direction, the motion is minimal (almost negligible) because the scanning speed is the fastest at the collection of A-scans. On the C-scan direction, the motion is the worst because the scanning speed is the slowest, and the B-scan direction is in between. This is why we designed the strategy to downsample the data differently at the A, B, and C scan directions. Comparing to a uniform downsampling, the proposed approach is efficient in reducing computational resources and increasing the stability of the algorithm on different samples. The number of downsampling levels and the iterations for parameters optimization can also be further optimized based on the cost function curves shown in Figure 2.1.7. For example, since the cost function for Affine transform converged on R1, it is not necessary to downsample four times. It is likely that with different type of OCT data, the required levels of downsampling for affine and B-spline transformation would also be different. Therefore, it is suggested that the optimal selection of downsampling levels is adjusted accordingly in terms of practical imaging situations.

Successful registration on both human skin data and human retina data from different OCT systems can also attest to the robustness of the proposed registration and averaging algorithm. Qualitatively, the averaging images are all shown with significantly less speckle noise and with line-like motion artifacts removed. On OCTA images, the connectivity of vasculature has been demonstrated to improve after averaging. The human skin data (Figure 2.1.7) revealed that the motion artifacts (the horizontal lines) are minimized and image contrast has been improved after averaging. For human retina data, Figure 2.1.5 showed that less speckle noise is present on OCT and OCTA B-scan images after registration and averaging. Particularly, the features of vessels and lumens in the choriocapillaris can be much clearly observed in averaged images. Figure 2.1.6 showed examples of *en face* projection images after the volumetric registration. On single scan OCTA images (Figure 2.1.6 (a) and (d)), there are small broken endpoints and disconnectivity within capillary networks as well as obvious motion artifacts (green arrows). After 3 or 6 averages, vasculature connectivity has been significantly improved and previously present motion artifacts have also been compensated. It is expected that further quantification analysis based on averaged OCTA

images could be much more reliable than single scan OCTA images. Quantitatively, we calculated SNR, PSNR and NCC as numerical descriptions of image quality. All three parameters have increased to a various extent with multiple averaging. Both qualitative and quantitative evidence strongly suggest that the proposed method can significantly improve OCT and OCTA image quality and potentially facilitate better clinical decision making.

Even though the proposed algorithm was designed for 3D data, it can also be applied to 2D images. Similar procedures have been reported in our previous study [65] with various constraints and parameters. The 2D registration requires fewer computation resources but it also requires layer segmentation as a step of image preprocessing. Moreover, with a 3D registration approach, it is likely that the extra depth information could be useful in some clinical settings. For example, the diagnosis and management of macular edema sometimes would require 3D OCT scans. In this case, this averaging approach could help obtain more accurate information of 3D tissue and vessel morphology.

There are a couple of advantages of our proposed algorithm comparing to previously published methods. Mostly, this proposed algorithm can be applied directly to OCT and OCTA data acquired from commercially available OCT systems. It does not require image preprocessing such as layer segmentation [84,85], or extra imaging hardware [79,81]. Therefore, compared to previously published methods, it has a wider range of application possibilities. It can also be applied to data from other 3D imaging modalities such as ultrasound, MRI, multiphoton microscopy etc. Moreover, this approach does not require any particular scanning protocols such as orthogonal scanning requirement like in [14], though it can be applied to data acquired by any scanning protocols.

There are also some limitations of the proposed algorithm. Firstly, this algorithm is an intensity based registration algorithm, therefore it could fail if the intensity of images is too homogenous. Luckily, biological tissues usually have some unique features that can guide the registration and reduce unconstrained errors. Secondly, it is quite computationally expensive to register multiple 3D volumes. We have already utilized parallelization for optimization to improve the speed of the framework, but it still takes 60 minutes to register and average 10 OCT volumes unider high quality setting, especially when each volume is as large as 600x600x2560 pixels. There certainly exists a tradeoff between the quality of registration and the computational resources needed. With the same workstation set up, the time needed for registration can be adjusted by optimizing the number of downsampling levels and the number of iterations according to practical situations. The future development is to implement the proposed algorithm on a GPU platform [98] to further improve the speed. Lastly, the proposed registration algorithm is not boundless, meaning that a certain amount of overlap between images is need to succeed. For our collected human retina data, the motion tracking feature was turned on during acquisition; and for our collected human skin

data, the portable probe was attached to the samples to avoid large subject movements. We did not observe any failures of registration on our collected data, but if the inter-volume motion is too large, this proposed algorithm can certainly experience errors or failures.

In conclusion, we have proposed a 3D registration method and demonstrated its robustness on reducing speckle noises and suppressing motion artifacts. Both human skin data and retina data were collected from different OCT systems to test the robustness of this proposed algorithm. Averaged OCTA data showed higher contrast of vascular network and better connectivity for vessels of all sizes, as evidenced by the resulting higher SNR, PSNR and NCC metrics. It is expected that the proposed algorithm would be practically useful in better visualization and more reliable quantification of in vivo OCT and OCTA data, which could be beneficial to research and clinical applications of OCT.

Chapter 2.2 Optical coherence tomography angiography distortion correction in widefield montage images

2.2.1 Introduction

Optical coherence tomography (OCT) angiography (OCTA) has recently emerged as a means of acquiring rapid, non-invasive, depth-resolved images of the posterior segment vasculature [61,94]. OCTA holds numerous advantages over traditional retinal visualization methods, such as fundus photography and fluorescein angiography (FA). One of the promises of OCTA is its ability to provide visualization and eventually quantification of the microvasculature. However, currently available OCTA technology also has several important limitations that prevent OCTA from fully assuming the diagnostic role of other imaging techniques. Chief among these limitations is the fact that, at present, OCTA cube images are restricted to at most 12 × 12 mm in size. Moreover, the 12 × 12 mm scan protocol is currently not widely available [99]. For a larger field of view that approximates the images provided by fundus photography or FA, a montage technique can be used [13,94]. In montage imaging, multiple images are taken with varying fixation targets. These individual images are then stitched together, using common overlapping features among them, to produce a final widefield image. In a previous case series, montage images were found to be comparable or superior to FA in detecting vascular abnormalities across a variety of pathologies [100].

In general, a typical OCT system suffers from two types of distortion: field distortion and optical distortion [101]. During OCT scanning, a pair of orthogonally arranged galvo-mirror scan at constant angular speeds that provide a two-way raster scan, so that the backscattering light from retinal tissue with the same optical path length as the reference optical length is recorded as a flat surface using a Cartesian coordinate system (Figure 2.2.1a). This introduces the fan-shape field distortion in 3D space (Figure 2.2.1b), the correction of which is well-described in the literature [102]. However, when imaging the retina, another distortion will be created by the geometry of the eyeball; the curvature of the eye introduces the radial distortion when generating the en-face projection. The extent of radial distortion is determined by the distance from the scan (the pivotal point at the pupil plane) to the fovea and the axial length of the eye, as illustrated in Figure 2.2.1(c). As the light spot moves from the fovea to the far peripheral region, the distortion increases due to the curvature of retina, as shown in Figure 2.2.1(d) [103]. The radial arc length of the retina is longer than the length that is projected on the projection plane; therefore the en-face images produced by the distorted 3D volumetric data result in 2D images with more significant distortion around the border (Figure 2.2.1e).

While these distortions may not be pronounced on small images, such as 3 × 3 or 6 × 6 mm scans, they become more relevant in scans that are larger than 12 × 12 mm. Radial distortion—a consequence of the en-face projection method that is widely used in ophthalmology—is particularly marked when imaging the

far peripheral region of the retina, impacting the image quality and the morphology of the vascular networks. Montaged OCTA images are thus especially susceptible to these distortions as they are composed of multiple 12 × 12 mm scans, many of which are obtained from the periphery of the eye.

Moreover, the creation of montaged images requires registration of images, which depends on the overlapped regions between adjacent scans to ensure common information. Image distortion can compound difficulties in image registration, and different registration methods can in turn introduce additional image distortion. Correcting image distortion prior to registration may mitigate the effects of further distortion introduced by registration.

In clinical practice and for research purposes, image distortion introduces difficulties in quantification of images. With quantitative metrics from OCTA images increasingly finding clinical application [104], it is important to recognize and try to correct possible factors that can introduce variability into these measurements. Several distortion correction methonds have been developed previous mainly based on Fermat's principle, Podoleanu et al. used ray tracing method to correct the distortion on cross sectional OCT images [105]. Ortiz et al. developed a numerical approach to correct the distortion on 3D anterior segments OCT [101]. However, these methods required prior knowledge of the system and samples. Other methods have also been introduced that require calibration [102,106], which is generally not feasible for clinical applications. Thus, we propose a novel methodology which uses 12 × 12 mm OCTA en-face images to montage and then generate an extended field-of-view retinal image that incorporates correction of both field and radial distortion with minimum parameters.

2.2.2 Methods

This prospective study conformed to the Declaration of Helsinki and the Health Insurance Privacy and Portability Act and was approved by the Institutional Review Board at Tufts Medical Center.

Imaging Protocol

16 eyes from 9 healthy participants (2 female, 7 male) were imaged. The mean age was 28.2 years. Participants had no to moderate myopia (0 to -7 D) with otherwise no ocular pathology. Axial length was measured in all participant eyes using a Carl Zeiss IOLMaster (Carl Zeiss Meditec AG, Jena, Germany). Five measurements were taken in each eye and then averaged to obtain a final axial length measurement.

30 minutes prior to imaging, all eyes were dilated using Tropicamide 0.5% ophthalmic solution. OCTA imaging was performed on the Carl Zeiss PLEX Elite 9000 swept-source OCTA prototype (Carl Zeiss Meditec, Dublin, CA, USA). The system is powered by a swept-source tunable laser that has a center wavelength of 1060 nm, operating at 100,000 A-scans per second with an A-scan depth of 3.0 mm. 12x12

mm OCTA scans were performed using the following nine fixation points, which were in-built into the device's software: superonasal, superior, superotemporal, nasal, central (foveal), temporal, inferonasal, inferior, and inferotemporal. FastTrack motion correction software was used during image acquisition. Each 12 × 12 mm scan consisted of 500 A-scans per B-scan with two-time repeats before moving to the next sequential B-scan location, which results in a homogenous sampling grid with an A-scan and B-scan separation of 24 µm. Five 12 × 12 mm images were taken in each eye. Un-montaged images were exported individually for analysis.

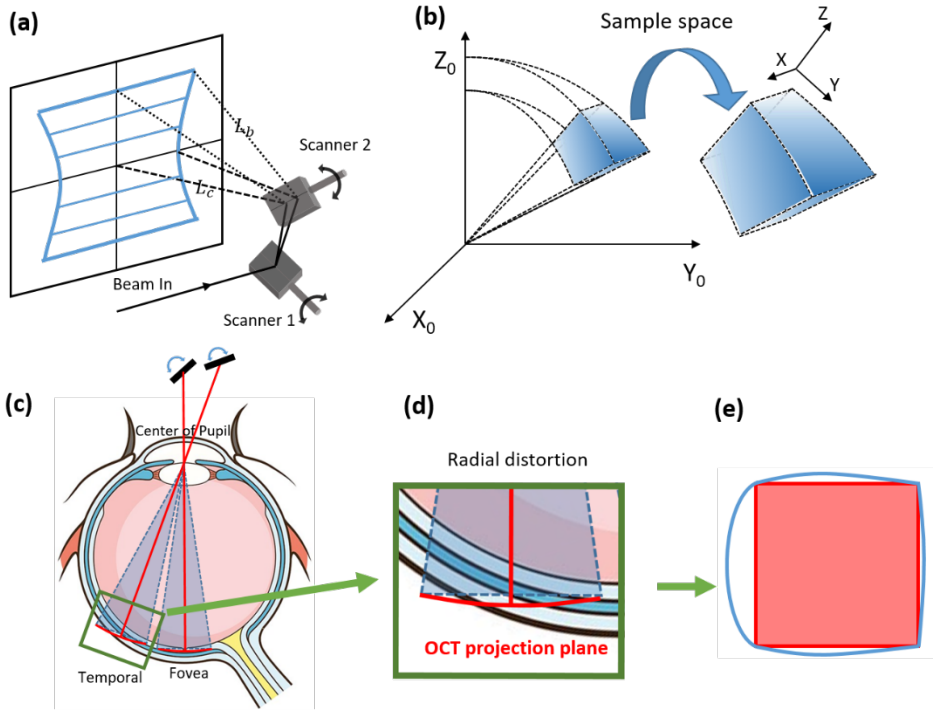

Figure 2.2.1: Schematic of image acquisition in OCT system.

(a) Setup of 2-way OCT galvo-scanner, that provides a raster scan pattern of the OCT probe beam at the fundus. The scanner 1 facilitates the fast B-scan with a fixed maximum scanning angle (that determines the B-scan size), and the scanner 2 is driven to steer OCT beam moving in the orthogonal direction to the Scanner 1, providing 3D scan. The distance from center of the region to the scanner (L_c) is shorter than the distance from the border of the region to the scanner (L_b), thus the lengths of corresponding B-scans are not equal at each B-scan locations within the field of view, as shown by the blue lines. (b) The fan shape region in sample space (x_0, y_0, z_0) is scanned by OCT system which is mapped to a data cube in a new Cartesian coordinate system (x, y, z) during data recording. This effect squeezes the pixels in deep retinal layers and stretches the pixels at the superficial retinal layer. (c) Illustration shows that two OCT 3D scans are obtained in the foveal and peripheral regions that suffer from radial distortion. The effects of distortion depend on the radial location of the scans. (d) Zoomed-in region of at the peripheral region shown in (c), the actual retina and OCT projection plane are not coincident. (e) The area inside the blue circle is the actual retina region

scanned by the OCT, and the red area is the corresponding region recorded in the data cube. Note the illustrations are not to the scale.

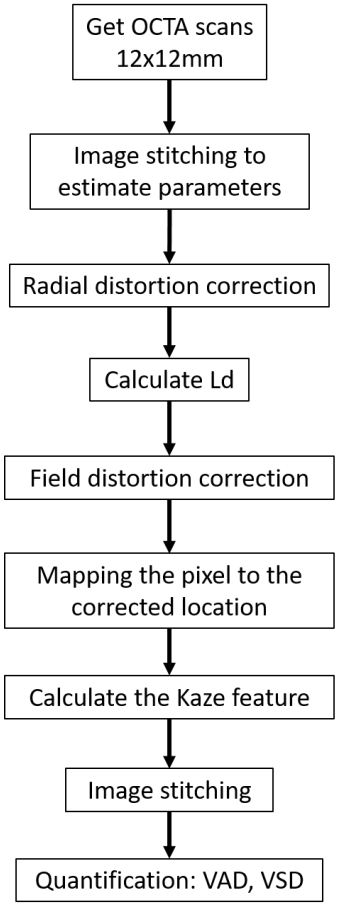

Figure 2.2.2. Flow chart describing the procedure for distortion correction and image quantification.

Radial Distortion Correction

All image correction and analysis steps were performed using Matlab 2017b (Mathworks, Natick, MA, USA). To compensate for radial distortion, the approximate relative location of each single OCT scan and its angular scan range was first estimated by rough image stitching. The algorithm first calculated the Kaze features (i.e., identified by multiscale 2D feature detection and described in nonlinear scale spaces) on two images and then paired the common features between the scans in order to roughly stitch them together [107]. The locations of the fovea and optic disc were then used as a reference to approximate the scanning angle for radial distortion correction. The compensation was based on the estimated distance from the off-axis angle to the fovea and the local curvature of eyeball.

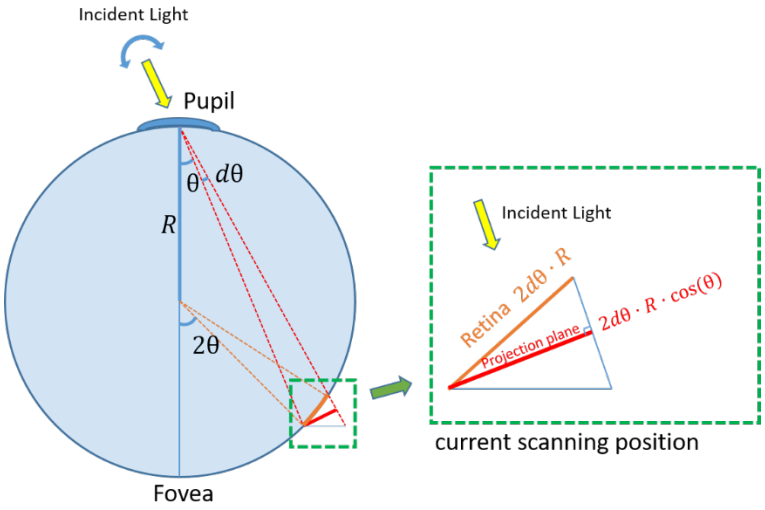

Figure 2.2.3. Geometric model for radial distortion correction.

The axial length of eye ball is assumed to be 2R. At the each scanning position θ, each small step of the scanning angle is $d\theta$. At the scanning position (region inside the green dash line), the retina plane on the sphere (orange line) is projected to the plane that is perpendicular to the incident light (red line) for recording. Therefore, the actual length of the retina is not correctly represented in the data cube. The accumulation of this error causes the radial distortion. Note drawings are not to the scale.

The shape of the eyeball is approximated as a sphere and with the pivotal point of the scanning OCT beam at the center of the pupil (Figure 2.2.1c). The distortion correction model is described in Figure 2.2.3 in more detail, where the axial length of the eyeball is assumed to be 2R and the arbitrary scanning angle is θ, which is within the range of the field of view represented by Φ. The scanning interval between adjacent A-scans in the fast axis is $d\theta$.

The correction ratio, $L_d(\lambda)$, for every pixel from the center of the fovea to the current angular scanning location λ can be integrated by:

$$L_d(\lambda) = \frac{\int_0^{\lambda} R \cdot d2\theta}{\int_0^{\lambda} R \cdot \cos(\theta) d2\theta}$$

For stitching the final widefield image, the calculated correction ratio L_d for each pixel was used to re-map that pixel into its original location in 3D. The numerator represents the real arc length from the fovea to the current scanning location and the denominator is the length on the projection plane. After this procedure was completed for all the pixels, the en-face 2D image was then obtained by projection to minimize the distortion for better visualization. We modified the concept of the azimuthal equidistant

projection on a sphere to ensure that all points on the corrected image are at the correct azimuth from the fovea, and that the distances from the fovea represented correctly [108].

Field Distortion Correction

To correct the field distortion, the working distance, scanning angle and the axial length of eye were recorded and then used to calculate the transformation matrix, as described previously [102]. Briefly, we first built a 3D matrix based on the size of the image and the estimated parameters above. Then, each pixel in the 2D image was re-sampled and transformed to a sphere surface in the 3D matrix. The coordinates in the 3D matrix were then transferred to the original physical space as the fan shape volume in Figure 2.2.1(b). Finally, the fan shape images were projected to a natural space to minimize the field distortion.

Image Stitching

After compensating for distortion, all individual images were stitched together using a feature-based image stitching method. The algorithm starts with a 2-image pair with relatively larger overlapping areas. The overall signal strength is calculated on each image to compensate and normalize the inhomogeneous illuminance of the vessel. The scale, corner, and the invariant features are calculated on the images (Figure 2.2.4a-b) and are further paired by the random sample consensus (RANSAC) method (Figure 2.2.4c)[109]. The affine and B-spline transformation are calculated by the paired feature points. After transformation, the overlapping areas are blended between the two images (Figure 2.2.4d). We perform the 2-image registration process iteratively until the five images were registered together as a single wide-field image.

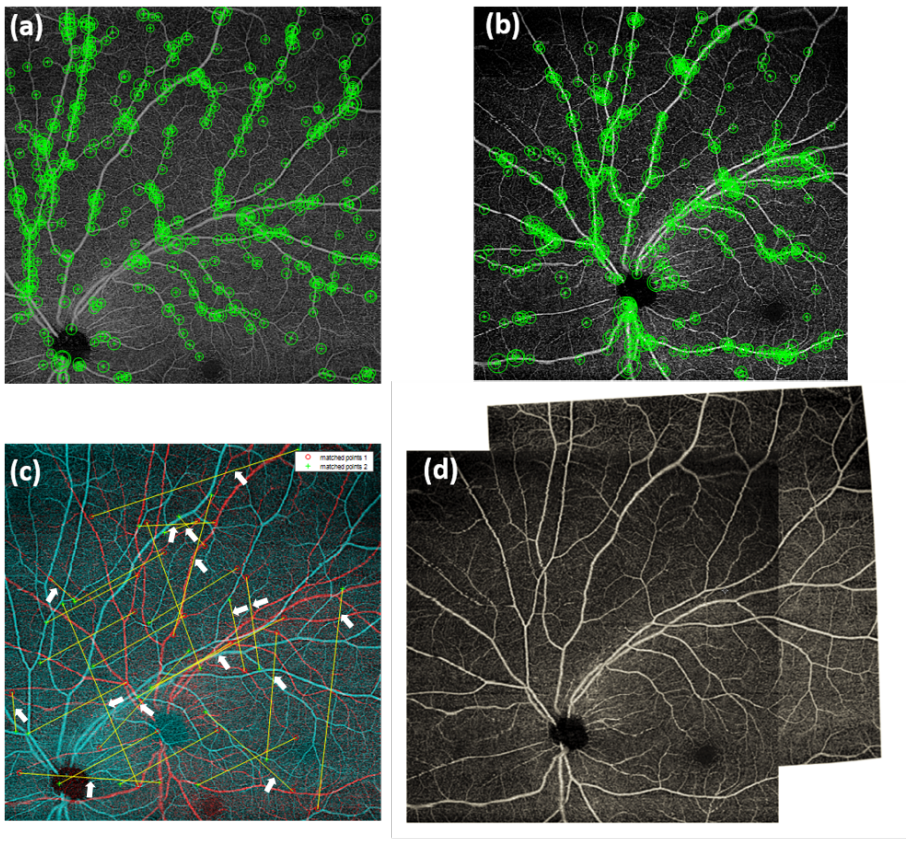

Figure 2.2.4: Image registration and montaging procedure.

(a, b) The KAZE feature points on two individual images are identified, represented by green circle cross symbols. (c) feature points on the two images (displayed in red and cyan colors respectively) are paired, represented by connected lines. Then RANSAC algorithm is used to reject the outlier of matched pairs, e.g. those pointed by the white arrows. The spatial transformation matrix is calculated by the remaining paired and matched points. (d) The final images are finally registered and stitched together to form a montage image.

Quantitative Analysis

To quantitatively analyze the influence of distortion, we applied our previously-described MATLAB-based algorithm to calculate quantification metrics [76,110–112]. The vessel area density (VAD), flow impairment area, and vessel complexity index (VCI) were calculated on the corrected and uncorrected widefield en-face OCTA images. VAD describes the percentage of the image occupied by flow information, i.e., the percentage of the vessel area in the entirety of binarized image. Flow impairment area is calculated from vessel skeleton map as the non-perfusion area between vessels. Finally, VCI describes the degree of branching in vessels.

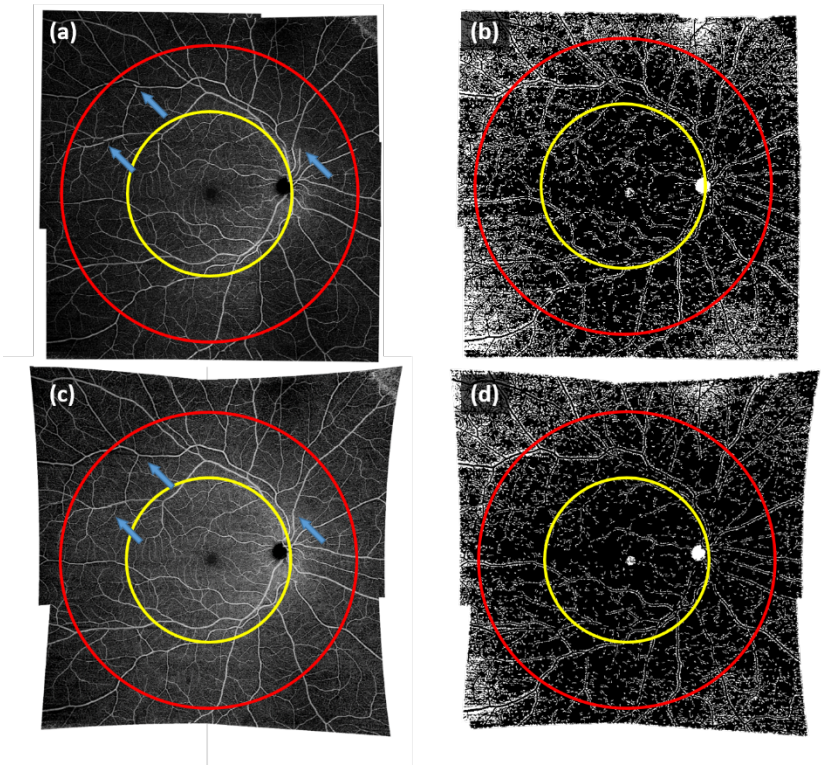

Figure 2.2.5. Example of quantitative analyses on macular and peripheral regions.

Five 12 × 12 mm images were acquired with the following fixation points: central, superonasal, superotemporal, inferonasal, and inferotemporal, which were used for montaging to form a wide field of view composite image. (a) The montaged image of the uncorrected images. Blue arrows show the registration error due to the distortion. (b) The flow impairment map of (a). (c) The montaged image of corrected images. Blue arrows show better connection of vessels. (d) The flow impairment map of (c). The macular region (yellow circle) is selected by the center of fovea and the ONH with radius r, and the peripheral region (red circle) is defined with radius1.8r.

The images were divided into a macular and peripheral region (Figure 2.2.5a and c). The macular region was defined by a circle with a radius r equivalent to the distance between the central macula and the optic disc. The peripheral region was defined by a concentric circle with a radius of 1.8r. Image areas outside of the circle were excluded from further quantification due to low image quality caused by vignetting, focusing issue and aberrations.

The Wilcoxon matched-pairs signed-rank test for non-normal data was used to compare metrics in the peripheral and macular region before and after image correction. Statistical analysis was performed using StataSE v15.1 (StataCorp, College Station, Texas, USA).

2.2.3 Results

The changes in metrics before and after image correction in the macular and peripheral regions are shown in Table 2.2.1.

Table 2.2.1: Average measurements by region, before and after image correction.

	Vessel Density		**Flow Impairment Area**		**Vessel Complexity**	
	Macular	**Peripheral**	**Macular**	**Peripheral**	**Macular**	**Peripheral**
Before Correction	0.503±0.018	0.491±0.025	0.089±0.036	0.147±0.067	4.755±0.477	4.476±0.418
After Correction	0.504±0.019	0.493±0.024	0.096±0.039	0.172±0.086	4.697±0.472	4.266±0.423
Change (%)	0.1	0.2	8.2	17.2	-1.2	-4.7
p-value	0.020	0.134	0.049	0.011	0.0004	0.0004

Vessel density changed very slightly before and after correction in the macular and peripheral region. Although the change in the macular region was statistically significant (p=0.02), the magnitude of the absolute change was so small (+0.1%) so as to not be clinically significant. The change in the peripheral region was also quite small and not statistically significant. There was a strong linear relationship in both the macular ($R^2 = 0.983$) and peripheral ($R^2 = 0.9992$) regions between the uncorrected and corrected vessel density values.

The average flow impairment area changed to a significant degree before and after correction, especially in the peripheral region (+17.2%, p = 0.011). In the macular region, there was a strong linear relationship between pre-correction and post-correction flow impairment area ($R^2 = 0.8894$). However, the linearity was not as strong in the peripheral region ($R^2 = 0.7579$).

The average vessel complexity decreased in both regions following correction, from 4.76 to 4.70 in the macular region and from 4.48 to 4.27 peripherally. These changes were both statistically significant but also small in magnitude (<5%). There was a strong linear relationship between pre- and post-correction vessel complexity in the peripheral and macular regions ($R^2 = 0.9957$ and 0.9973, respectively).

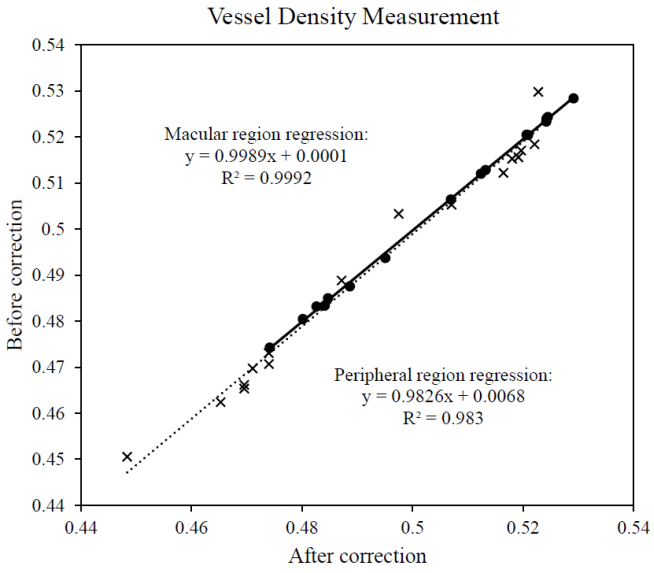

Figure 2.2.6. Relationship between before- and after-correction vessel area density.

Where the symbols "•" denotes the values from macular region, and "×" from peripheral region, respectively. The solid and dashed lines denote linear regression lines of the macular and peripheral measurements, respectively.

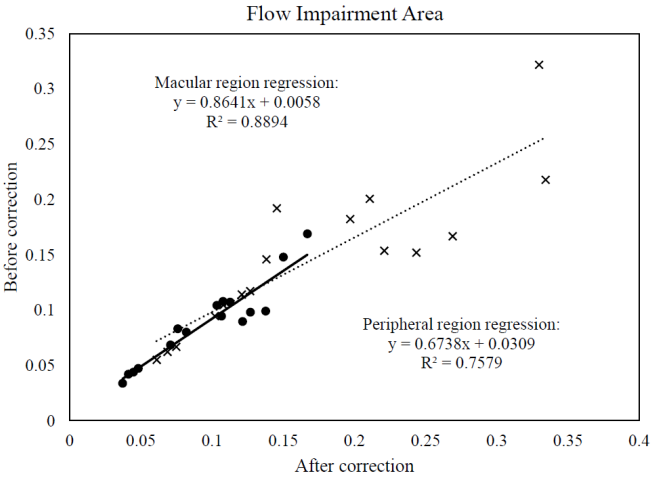

Figure 2.2.7: Relationship between before- and after-correction flow impairment area.

Where the symbols "•" denotes the values from macular region, and "×" from peripheral region, respectively. The solid and dashed lines denote linear regression lines of the macular and peripheral measurements, respectively.

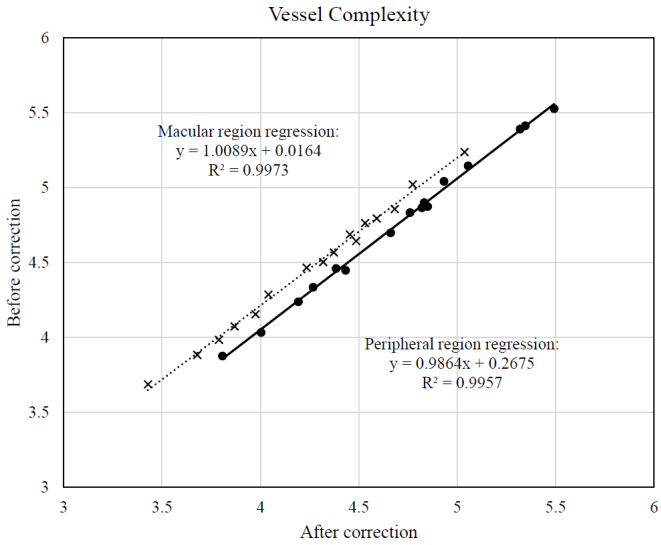

Figure 2.2.8: Relationship between before- and after-correction vessel complexity.

Where the symbols "•" denotes the values from macular region, and "×" from peripheral region, respectively. The solid and dashed lines denote linear regression lines of the macular and peripheral measurements, respectively.

2.2.4 Discussion

As the quality and acquisition speed of images produced by commercial OCTA devices continues to improve, widefield angiography imaging is becoming more common in clinical practice. The PLEX Elite device, as with some others, already has automatic montaging software, which can montage five 12 × 12 mm images with varying fixation points into a single widefield image on the device itself. Ensuring correct presentation of vasculature on widefield montage images is thus increasingly important. Our model is able to estimate the location of a single scan, apply distortion correction, and precisely stitch together single scans into one ultra-widefield montage image.

It is inevitable to introduce distortion when performing projections from a 3D spherical eyeball to a 2D flat surface. The field distortion of a single scan creates a mismatch in the overlapping region between adjacent scans. Distortion correction may benefit the quality of image registration, especially on the border area of the peripheral images. The projection model we applied in this approach is modified from the azimuthal equidistant projection approach. It maintains proportionately correct distances from the central fovea to far peripheral region for ultra-widefield retinal images. A similar approach could be applied to other map projections, such as equidistant or equal-area, to satisfy different goals.

In one prior study on correction of OCT images for eye curvature, Kuo *et al.* applied a radial correction to spectral domain-OCT B-scans in order to take into account the curvature of the posterior eye [113]. They

compared metrics from the uncorrected and corrected images to dimensions obtained from magnetic resonance imaging (MRI) scans of the eye. Correction of the OCT images resulted in less variable eye radius curvature values that were closer to those from the reference MRI images. Image correction did not, however, result in a significant change in retinal thickness measurements. The effects of image distortion on quantitative metrics thus may be more relevant in en-face OCT scans, such as those produced by OCTA, than in cross-sectional B-scans.

The prior literature examining correction of widefield ophthalmic imaging has focused largely on fundus photographs and fluorescein angiography images. In a 2016 study, Tan *et al.* used a stereographic, rather than the conventional azimuthal, projection for ultrawide-field FA images [114]. Stereographic projections preserve shape and angle, but do not accurately preserve area information. Tan *et al*. found non-significant difference in non-perfusion area between the uncorrected and corrected images. Spaide applied a different projection technique, the Lambert azimuthal equal-area projection, which does preserve areas accurately but does not accurately display angles [4]. To our knowledge, this methodology is the first that incorporates radial and projection distortion correction into registration of widefield montage OCTA images.

In the present study, the changes in vessel complexity and vessel density were either not statistically significant or were so small in magnitude so as to be clinically insignificant. However, there was a larger degree of change in vessel flow impairment area between uncorrected and corrected montage images. Although both vessel density and flow impairment area increased with correction, primarily due to image stretching, this increase was not equal likely because of variations in the degree of stretching applied to flow and non-flow areas, and different methods to quantify these variables. Flow impairment quantification in widefield OCTA images is increasingly being applied, particularly in studies of diabetic retinopathy, highlighting the importance of considering how distortion correction may affect these metrics [61]. This effect was more pronounced peripherally, which is consistent with the greater degree of distortion that occurs in peripheral scans. This finding is particularly relevant in the imaging of diseases, such as diabetic retinopathy, that may present early with peripheral lesions, including neovascularization, microaneurysms, and nonperfusion.

Our results further reveal that the changes in vessel complexity and vessel density were small in magnitude and maintain a very good linear relationship with the original images. The corrected images were locally stretched or compressed as compared to the original images, causing the vessel area to be scaled by the same factor. Thus, the VAD only changed by a small magnitude. The distortion correction did not change the morphological shape of the vessel as the VCI change was also small. To calculate the flow impairment area, our algorithm excludes small discontinuous non-flow areas on the binary vessel map in order to avoid

including physiologic non-perfusion areas between capillaries; consequently, the radial distortion did influence calculation of the flow impairment area, especially in the peripheral region.

Generally, the changes in the quantification parameters post-correction can be expressed by a Taylor expression as below:

$$f(s) = f(s_0) + f'(s_0)\Delta s + \frac{1}{2} f''(s_0)\Delta s^2 + \cdots$$

As the changes in the parameters Δs are small, the high order term of the expression can be ignored. The changes of parameters then followed a linear approximation: $f(s) - f(s_0) \approx k\Delta s$.

Thus, the small changes in VAD and VCI resulted from a relatively linear relationship (Figure 2.2.6, 2.2.8). However, the changes in flow impairment area were relatively large as they were the result of more non-linear effects (Figure 2.2.7).

There were several limitations in our study. In some cases, the most peripheral areas of the scan could not be well-visualized due to eye curvature exceeding the visualized window within the depth of the OCT scan. However, we limited our analysis to a portion of the image defined by a $1.8r$ circle; as a result, the most distorted peripheral regions were not included. In addition, peripheral areas with low signal strength may have impacted quantification. Finally, we restricted our analysis to normal eyes. The effects of distortion correction may be different in imaging of pathologic eyes, particularly for diseases that cause significant peripheral vascular changes. This study's strengths include our algorithm's multifaceted approach to image correction, as well as the inclusion of eyes with varying axial lengths—mirroring the makeup of the general population and allowing our analysis to incorporate varying degrees of eye curvature.

Further research is needed to better understand the optimal approach for image correction in widefield imaging, and the impact that image correction has on quantitative metrics relevant for clinical and research practice.

2.2.5 Conclusion

Correction of widefield montage OCTA images for field and radial distortion, as well as precise image stitching, resulted in non-significant or small changes in vessel density and vessel complexity, but a significant change in flow impairment area, which was more pronounced peripherally than centrally.

Chapter 3. Using OCT to better understand the biomarkers of Age-related Macular Degeneration

The use of optical coherence tomography (OCT) to better understand the biomarkers of age-related macular degeneration (AMD) provides valuable insight into the complex interactions between retinal structures and the progression of AMD. This chapter evaluates OCT techniques, focusing on their application in identifying and distinguishing various AMD-related biomarkers in the retina and choroid.

Section 3.1 discusses a study investigating the impact of calcified drusen on the detection of choriocapillaris flow deficits (CCFD) using swept-source OCT angiography. This section highlights the challenges posed by the high scattering properties of calcified drusen, which obscure the underlying vascular features and complicate the assessment of choriocapillaris perfusion. The results highlight the need for compensation strategies for soft drusen and to exclude artifactual signals in the presence of calcified drusen.

Section 3.2 compares the diagnostic capabilities of OCT B-scan and en face imaging in the assessment of macular atrophy in AMD. It presents a comprehensive analysis of how different scanning protocols and OCT devices can lead to variations in the identification and grading of atrophic lesions. The comparison highlights the need to increase scan density for en face imaging to achieve comprehensive lesion grading.

Chapter 3.1 Calcified Drusen Prevent the Detection of Underlying Choriocapillaris Using Swept-Source Optical Coherence Tomography Angiography

3.1.1 Introduction

Age-related macular degeneration (AMD) affects the central part of the retina known as the macula and is a leading cause of irreversible blindness among the elderly worldwide [67]. Optical coherence tomography (OCT) imaging provides non-invasive and rapid high-resolution three-dimensional (3D) images of the macular anatomy and it has become the modality of choice to stage, treat, and monitor disease progression in AMD [36,38,115]. These images offer valuable insights into the progressive microstructural and microvascular changes that occur in AMD. The widespread use of OCT in ophthalmology has facilitated the identification of OCT biomarkers associated with the progression of changes from early to late AMD. These biomarkers include the area and volume of typical soft drusen [116], the area and volume of calcified drusen (CaD) [117], subretinal drusenoid deposits (SDDs) [118], hyperreflective foci (HRF) [63,68], basal laminar deposits [119], the presence of persistent choroidal hypertransmission defects (hyperTDs)[120], lesions consistent with the complete retinal pigment epithelium and outer retinal atrophy (cRORA) [121,122], and the presence of

choriocapillaris flow deficits (CCFDs) [66,123]. In particular, the extent of CCFDs, detected using OCT angiography (OCTA), has been associated with drusen, the growth of choroidal hyperTDs, the decrease in low luminance visual acuity (LLVA), the increase in LLVA deficits and delayed dark adaptation [124–126]. The local changes in CCFDs have shown a correlation with the growth rate of GA [124]. Thus, understanding the nuances of local variations in choriocapillaris flow can provide insight into disease progression and suggest potential therapeutic targets, especially in early stages or surrounding areas not yet affected by atrophy.

Drusen are formed due to the extracellular deposits that accumulate between the basal lamina of retinal pigment epithelium (RPE) and the inner collagenous layer of Bruch's membrane (BM) [127–130]. The presence of two different types of calcifications – micron sized spherules and calcified nodules has been reported in literature [131–133]. While their differential impact on disease progression and imaging have not been fully explored, the micron-sized spherules are found ubiquitously in all types of drusen, including soft drusen and basal linear deposits. These spherules are involved in drusen formation and growth.

It is hypothesized that the presence of hundreds of these spherules within soft drusen, along with lipids and proteins, would attenuate but not completely block the OCT signals. The attenuated signals under these drusen can be detected in the choroidal structural layers. The attenuated signals under soft drusen tend to be mild and can be compensated using a strategy in which the inverted structural signal from the CC layer is used to enhance the detection of OCTA CC flow signal [127,134]. The underlying assumption when using this strategy is that, if a detectable attenuated signal is present, the compensation strategy can recover the diminished angiographic signal. This strategy has been validated in eyes where the drusen volume resolved spontaneously and the compensated CCFD measurements under drusen prior to drusen resolution were found to be comparable to the compensated measurements obtained after the drusen had resolved [**Error! R eference source not found.**]. However, when the attenuation of the signal is complete, we refer to this completely attenuated signal as a choroidal hypotransmission defect (hypoTD) [10], and the compensation strategy used for typical soft drusen does not work with the CaD that cause hypoTDs.

The presence of CaD, also known as refractile drusen on color fundus imaging or drusen with either hyperreflective or hyporeflective cores on OCT imaging, has been shown to be a biomarker for disease progression [11,135,136]. CaD contain calcium phosphate spherules [117], leading to increased optical absorption and light scattering [137,138]. Consequently, the calcified deposits impede the OCT light from penetrating into the choroid, resulting in hypoTDs in the choroidal layer [11]. This process is similar to the one caused by increased pigmentation within the retina, known as HRF, or along the RPE border [68,139]. However, while we observed complete hypoTDs in the CC layer and deeper choroidal layers beneath hyperpigmentation, CaD resulted in a complete hypoTD specifically within the deeper choroidal layers (e.g., subRPE slab) but

not in the CC layer. Additionally, we observed an absence of OCTA signal in the CC layer that could not be compensated since the OCT signal in the CC structural layer did not appear to be attenuated. In order to explain this lack of attenuation in the CC structural layer, together with the complete attenuation of OCT signal in the deeper choroidal layers, we hypothesize that the highly scattering properties of the calcium phosphate spherules within the CaD, unlike the lipoprotein deposits within typical soft drusen, lead to the artifactual appearance of a structural signal under the CaD in the CC layer. And this artifactual signal is caused by the multiple scattering of OCT light within CaD, giving rise to a tail-like false OCT-signal beneath the CaD that does not carry meaningful information on CCFDs from the OCTA signal. Therefore, understanding the influence of CaD on CCFDs detection is important when using CC perfusion under drusen as an OCT biomarker for disease progression.

The primary objective of this study was to investigate the impact of CaD on the detection of CCFD and to determine if CCFDs can be reliably measured under CaD. In this study, eyes were categorized into three groups: eyes with soft (or typical) drusen, eyes with CaD, and normal age-matched eyes. We proceeded to quantify the CCFDs density by utilizing a heatmap mask and outlining regions exhibiting abnormal concentrations of CCFDs or choriocapillaris flow impairment. We then evaluated the correlation between CCFDs and both typical drusen and CaD by using Dice similarity coefficients (DSCs) derived from the respective CCFD masks and lesion masks. Subsequently, we performed a phantom experiment to simulate the impact of the scattering particles within the CaD and to verify how the presence of CaD would obstruct light propagation into the choroid, while at the same time explaining a structural signal in the CC layer, combined with the absence of OCTA signal from the CC layer.

3.1.2 Material and methods

This retrospective review of a prospective observational OCT imaging study was approved by the institutional review board of University of Miami Miller School of Medicine. The study was performed in accordance with the tenets of the Declaration of Helsinki and complied with the Health Insurance Portability and Accountability Act of 1996. Written informed consents were obtained from all participants before enrollment. Three groups of subjects including eyes with CaD, eyes with soft drusen, and normal eyes were identified from the natural history study and imaged from June 2016 to June 2022 with 3-month intervals over 9 months. Axial length measurements were performed using a noncontact biometry instrument (IOLMaster; Carl Zeiss Meditec, Dublin, California, USA). Exclusion criteria included confounding ocular conditions such as an axial length $\leqslant$ 23 mm or $\geqslant$ 26 mm, glaucoma, and chorioretinal disorders other than dry AMD.

Imaging acquisition

All subjects were scanned using the PLEX® Elite 9000 (Carl Zeiss Meditec, Dublin, CA, USA). The SS-OCTA instrument employed a laser light source with a 1050 nm central wavelength and a 100 nm bandwidth, providing an axial resolution of approximately 5 µm and a lateral resolution of approximately 20 µm estimated at the retinal surface. All patients were imaged using the 6×6 mm scan pattern centered on the fovea. This SS-OCTA scan pattern consisted of 500 B-scans with 500 A-scans per B-scan and each B-scan was repeated twice at each B-scan position, ensuring a uniform 12 µm spacing between fast and slow scans. The angiographic flow information was generated using the previously validated complex optical microangiographic (OMAGc) algorithm [36,140]. Scans with a signal strength less than 7 based on the instrument's output, as well as scans with significant motion artifacts, were excluded.

Image processing

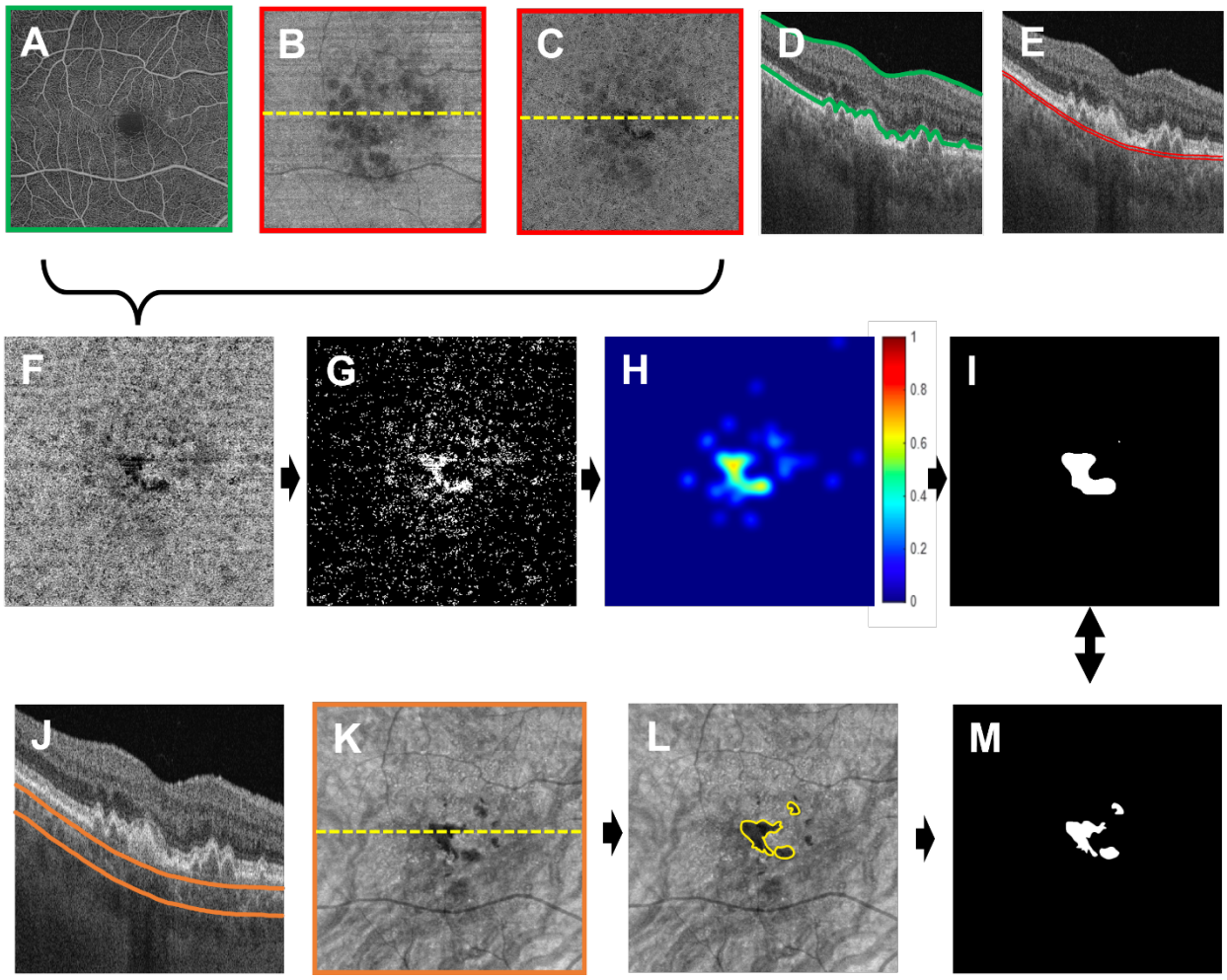

Figure 3.1.1. A schematic flow chart illustrating the image processes.

The process generates and quantify the choriocapillaris flow deficits (CCFDs) and to generate the CCFD masks and the calcified drusen masks for later comparison, taking an eye with both soft and calcified drusen as an example. (A-C), a set of en face images that were generated from the 3D OCTA scans, including en face OCTA retinal flow image (Panel A), OCT choriocapillaris (CC) structural image (Panel B) and OCTA CC flow image (panel C). (D, E) showing representative B-scan image located at the position marked as dashed yellow line in (A-C), illustrating the segmentation lines to define the slab (bounded by green lines, Panel D) to generate en face retinal flow image shown in Panel A, and the slab (bounded by red lines, Panel E) to generate CC enface images shown in Panel B and C, respectively. (F), the compensated CC flow image that was obtained by a validated compensation algorithm and followed by exclusion of any areas with hyperpigmentation and persistent hypertransmission defects. (G), binary CCFD images showing flow deficit regions. (H), CCFD heat map generated from binary CCFD flow image in Panel G, showing the impaired regions of choriocapillaris. (I), final CCFD density mask that was generated by applying a threshold from the heat map in Panel H for comparison with the identified calcified drusen. (J-M), illustrating the steps for manual identification of calcified drusen and generating the corresponding masks, where the calcified drusen were identified and manually outlined (yellow outlines in Panel L) by hypoTDs appeared in the subRPE enface image (Panel K) and confirmed by the corresponding B-scans (Panel J), and finally a mask was generated from the outlines showing the area occupied by the calcified drusen (Panel M). The generated CCFD mask (Panel I) and calcified drusen mask (Panel M) were finally compared to compute a Dice similarity coefficient.

Visualization and quantitation of the CC were performed using the 6×6 mm scans to compute the CCFDs within a 5 mm circle centered on the fovea. A schematic flow chart for the quantification process is shown in Figure 3.1.1. First, a set of en face images were generated from a 3D SS-OCTA 6×6 mm scan that included an OCTA retinal microvascular image (Figure 3.1.1A), a CC structural image (Figure 3.1.1B), and a CC flow image (Figure 3.1.1C), which are needed in the compensation algorithm to adjust for any signal loss and projection artifacts due to the overlying anatomy, including the retina and the RPE/BM complex. After compensation, the CCFD map (Figure 3.1.1F) was thresholded and binarized to quantify the CCFDs as previously described [65,127,141]. The retinal microvascular image (Figure 3.1.1A) was generated by maximum projection of OCTA signals within a slab defined by the inner limiting membrane to 20 μm above the RPE layer (green segmentation lines shown in corresponding B-scan in Figure 3.1.1D). This image is used in the compensation algorithm to remove the overlying retinal projection artifacts in the CC flow image. The en face CC structural (Figure 3.1.1B) and flow (Figure 3.1.1C) images were generated by using a 16 μm thick slab positioned 4 μm beneath the BM [142] using a maximum projection method. Before thresholding, any areas with hyperpigmentation [68,143] and persistent hyperTDs [10,57] were excluded from the compensated CC flow images in Figure 3.1.1F. The fuzzy C-means thresholding algorithm (FCM method) was applied as previously described [66] to produce binary CCFD maps and CCFDs less than 24 μm in size were excluded for the final CC quantification (Figure 3.1.1G). The CCFD percentage (CCFD%) was

defined as the ratio of FD areas (bright areas in Figure 3.1.1G) to the total quantifiable area. CCFD% within a 5 mm circle centered at fovea were also computed.

To facilitate the comparison between CCFD and CaD, a binary mask showing impaired choriocapillaris perfusion regions was generated from the CCFD image (Figure 3.1.1G). In doing so, we first generated a heatmap (Figure 3.1.1H) from the binary CCFD map in which the size of each individual CCFD was measured and a size threshold was applied to create the CCFD heatmap using a gaussian blur function, which represents the density of CCFDs [76]. A density threshold was then applied to the heat map to produce the final CCFD density mask (Figure 3.1.1I), indicating the main area with impaired choriocapillaris perfusion. A grid search algorithm was used to determine the optimized size and density thresholds in this procedure [144], where a criteria of maximum correlation between the density mask and the CaD mask was used to constrain the search. This procedure resulted in the thresholds of 55 pixels for the size and 0.25 for the density, respectively.

In the soft drusen group, the same thresholds for size and density were applied to obtain the CCFD density masks.

Identification of Drusen

Area and volume measurements of typical soft drusen were generated using a validated algorithm known as the Advanced RPE Analysis Algorithm version 0.10, which is available on the Advanced Retinal Imaging Network website (Carl Zeiss Meditec, Dublin, CA, USA) [135]. The drusen volumes in the 3 mm and 5 mm circles centered on the fovea were obtained. CaD were identified as hypoTDs on the sub-RPE structural en face images that are generated using a slab from 64 μm to 400 μm below BM (Figure 3.1.1K). CaD were confirmed using corresponding B-scans (Figure 3.1.1J) as previously reported. These CaD were manually outlined (Figure 3.1.1L) and their area measurements within the outlined boundaries were calculated. Finally, a binary mask was generated showing the areas occupied by the CaD (Figure 3.1.1M) for later computation of DSC with CCFD density mask as described in the last section (Figure 3.1.1I).

In the soft drusen group, the drusen masks were created from the drusen elevation maps generated from the SS-OCT Advanced RPE Analysis Algorithm version 0.10.

Correlations Between CCFDs and Drusen

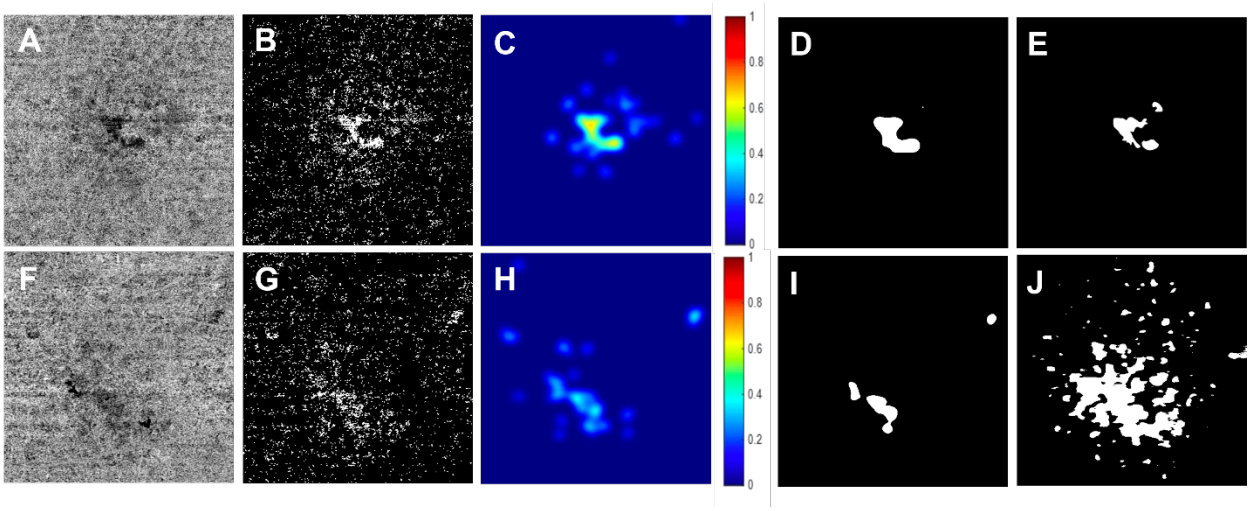

Figure 3.1.2. Examples of choriocapillaris flow deficit (CCFD) density masks and drusen lesion masks for computing Dice similarity coefficients.

(A-E) Same eye as in Figure 3.1.1 with calcified drusen. (F-J) Eye with soft drusen. (A, F) Compensated CC flow images with the exclusion of any areas with hyperpigmentation and persistent hypertransmission defects. (B, G) Corresponding binary CCFD maps of panels A, F. (C, H) Corresponding CCFD heat maps of panels B, G. (D, I) CCFD density masks produced by using the density threshold on the CCFD heat maps in panels C, H. (E, J) Lesion masks generated by manual outlines of drusen and used to compare with CCFD density masks for the calculation of Dice similarity coefficients.

Correlations between CCFDs and both CaD and typical soft drusen were investigated (Figure 3.1.2). To accomplish this, we evaluated the degree of overlap between the CCFD density masks (Figure 3.1.1I and Figure 3.1.2D) and the CaD masks (Figure 3.1.1M and Figure 3.1.2E), for which DSC was computed and compared. The value of a DSC ranges from 0, indicating no spatial overlap between two sets of binary segmentation results, to 1, indicating a complete overlap.

$$DSC = \frac{2TP}{2\mathrm{TP} + \mathrm{FP} + \mathrm{FN}}$$

Where TP denotes true positive, FP denotes false positive, and FN denotes false negative.

The DSC was also calculated between the CCFD density masks and the soft drusen masks (Figure 3.1.2F-J), where the soft drusen mask was created from the drusen elevation map generated from the SS-OCT Advanced RPE Analysis Algorithm version 0.10. The correlation of the square-root area (sqrt) of the CCFD density masks against the sqrt area of CaD and soft drusen were analyzed and compared.

Phantom experiments

To investigate the influence of CaD on OCTA signals, a simplified three-layer phantom was designed and fabricated to simulate the optical properties of the retina tissue with the inclusion of highly scattering lesions to mimic CaD (Figure 3.1.7A). The top layer is a transparent glass layer (to simulate the neural retina tissue that is relatively transparent to the light). To mimic the CaD, we deposited a number of droplets with a size of approximately 200 μm and a height of approximately 80 μm onto a glass slide. The droplets were made of solidified agar emulsion mixed with 1.5% titanium oxide (TiO2), which gives an approximate optical attenuation (or scattering) coefficient of 3.0/mm. The choice of this droplet to mimic the CaD was empirical, however, its light scattering strength is similar to the optical attenuation property of calcium phosphate spherule aggregates [145]. We then flipped the slide over so that the droplets were in direct contact with the thin empty channel designed to accommodate the flow of intralipid that served to mimic choriocapillaris/choroidal blood flow. If the slide had not been flipped over, then the glass slide would have been between the TiO2 droplets and the flowing intralipid. While the configuration of the TiO2 droplets is opposite of the expected configuration of drusen, the construct allows for the direct approximation of the droplets to the choriocapillaris/choroidal flow, much as it exists in the back of the eye when drusen and the choriocapillaris are separated by a thin Bruch's membrane .A phantom with the structural configuration identical to the naturally-occurring configuration of drusen and choriocapillaris requires advanced engineering capabilities that were not available to us. However, this current design adequately demonstrates the detection of an artifactual structural signal beneath the droplet that arises due to high light-scattering properties of the droplet, which obscures the detection of flow in the layer that would be analogous to the choriocapillaris layer that is the layer of interest. The bottom layer was constructed from a highly light-scattering solid base that was designed to mimic the properties of the sclera layer. Then, the dynamic flow was introduced through the infusion of a 5% intralipid solution into the flow channel (middle layer) to simulate the physiological conditions. Note that a 5% intralipid solution has scattering characteristics (with a reduced scattering coefficient of ~1/mm) similar to blood. After its fabrication, the phantom underwent SS-OCT imaging using a home-built swept-source OCT (SS-OCT) system with a central wavelength of 1050nm. This setup facilitated the acquisition of 3D OCT and OCTA images. Notably, the home-built SS-OCT system demonstrated performance characteristics akin to clinical SS-OCT systems, ensuring the reliability and translatability of the acquired phantom data [146].

Statistical analysis

Continuous data were described as mean ± standard deviation. Independent sample t-test and chi-square test compared the results from two groups. Pearson's linear correlation compared the sqrt area of the CCFD density masks and the lesion masks. Statistical analyses were performed with IBM Statistical Package for

the Social Sciences (SPSS) software version 28 (IBM, Armonk, NY) with a p value of < 0.05 considered to be statistically significant.

3.1.3 Results

A total of 90 eyes were selected, in which thirty eyes (29 patients) had CaD, 30 eyes (26 patients) had soft drusen, and 30 eyes (30 patients) served as normal controls. Table 3.1.1 shows that the eyes were well-matched with respect to age and gender across the three groups. In addition, drusen volume within the fovea-centered 3 mm and 5mm circles was matched between the CaD and soft drusen groups (both $p > 0.05$).

Table 3.1.1. Characteristics of subjects and eyes with calcified drusen, typical soft drusen eyes, and eyes with no obvious disease

	Calcified Drusen (N=30)	Typical Soft Drusen (N=30)	Normal (N=30)	p value
Age (years), Mean ± SD	75.07 ± 7.24	73.10 ± 6.05	74.00 ± 6.68	0.52
Gender, Male%	36.67%	50.00%	56.67%	0.14
Drusen volume in 3 mm circle (mm3), Mean ± SD	0.15 ± 0.12	0.15 ± 0.11	NA	0.91
Drusen volume in 5 mm circle (mm3), Mean ± SD	0.21 ± 0.15	0.18 ± 0.15	NA	0.41

Abbreviations: SD, standard deviation; NA, not applicable

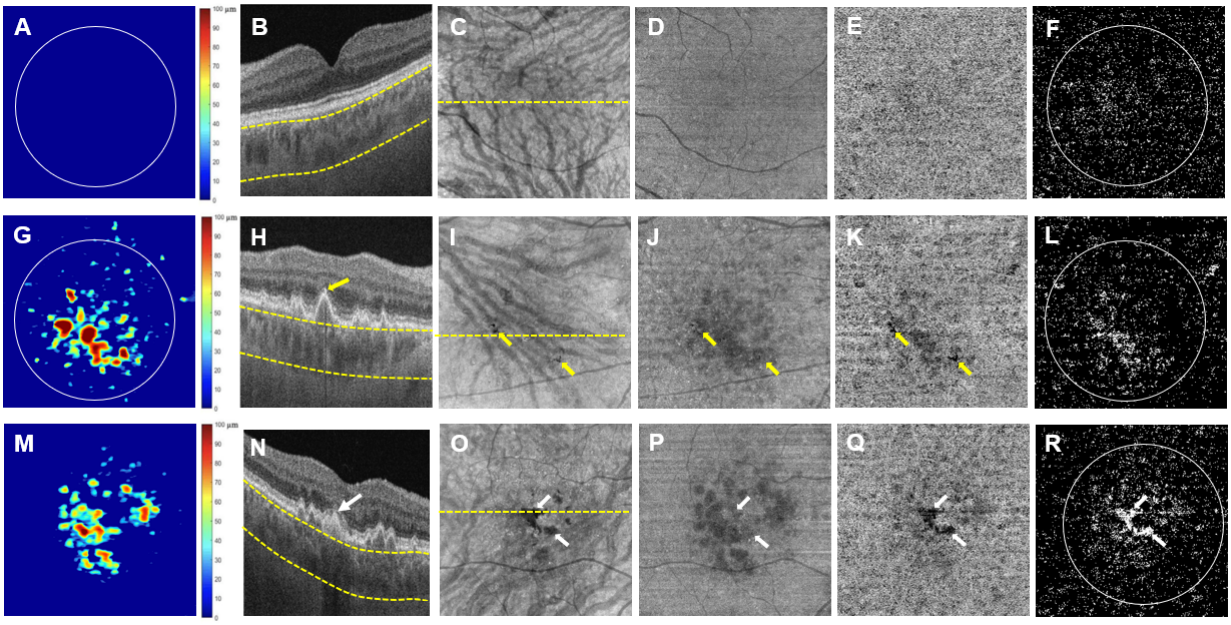

Figure 3.1.3. Examples of a normal eye (A-F), an eye with soft drusen (G-L), and an eye with calcified drusen (M-R) imaged using swept source OCT angiography (SS-OCTA) scans.

(A, G, M) Drusen elevation maps generated from the SS-OCT Advanced RPE Analysis Algorithm version 0.10. The white 5 mm circles centered on the fovea indicate the areas that were used to measure the drusen volumes. (B, H, N) Corresponding OCT B-scans indicated by the dashed yellow lines on the subRPE structural images (C, I, O). The segmentation boundaries used to generate the subRPE slabs are shown by the yellow dashed lines in each panel. (C, I, O) En face subRPE structural images show evidence of choroidal hypotransmission defects (hypoTDs), which correspond with the calcified druse (white arrow) in panels N, O, Q and hyperpigmentation (yellow arrow) in the soft drusen eye in panels H, I, K. (D, J, P) En face CC structural image from the normal eye shows a homogeneous grey area with the outlines of retinal vessels (D) while the eyes with drusen show shadowing from drusen and signal loss from hyperpigmentation (J, P). (E, K, Q) Compensated CC flow images were generated after excluding the areas of hyperpigmentation. (F, L, R) Binary CCFD images were computed to measure the CCFD percentage (CCFD%) (white foci denote CCFDs). The white 5 mm circles centered on the fovea indicate the area that was used to analyze the CCFDs.

Figure 3.1.3 displays representative cases of a normal eye (Figure 3.1.3 A-F), a soft drusen eye (Figure 3.1.3 G-L), and a CaD eye (Figure 3.1.3 M-R) imaged using SS-OCTA scans to generate en face images, corresponding B-scans, drusen volume maps, and compensated CCFD binary maps. Compared with the normal eyes, the structural images from eyes with drusen show signal attenuation under the soft drusen and complete signal loss beneath the hyperpigmentation (Figure 3.1.3 H, I, K). However, no signal loss was observed on the structural CC slab underlying the CaD (white arrows, Figure 3.1.3 N, O, P), whereas the flow signal on the CC slab underlying the CaD was absent (white arrows, Figure 3.1.3 Q, R)

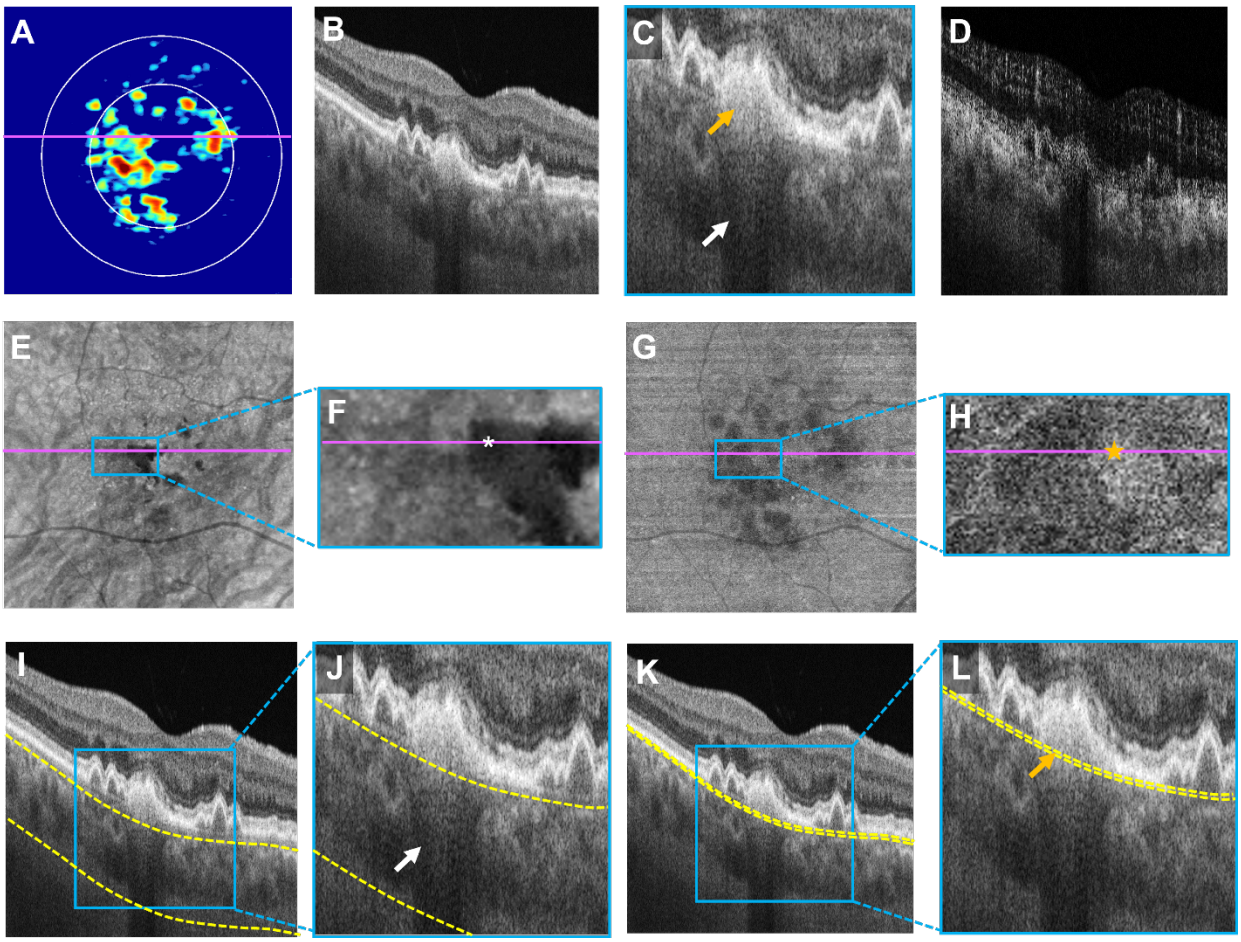

Figure 3.1.4. Illustration of OCT imaging characteristics of calcified drusen (CaD).

Shown is a representative example of an eye with CaD imaged with swept source OCT angiography (SS-OCTA). (A) Drusen volume map. (B) OCT structural image located at the position marked by purple horizontal line in panels A. (C) Enlarged OCT structural image containing CaD. The orange arrow indicates the hyperreflective scattering tail and the white arrow points to the hypotransmission defect (hypoTD). (D) OCT-A flow image at the location marked by purple horizontal line in panels A. (E) En face sub-RPE image generated from a slab defined by segmentation boundaries at 64 to 400 µm below Bruch's Membrane (BM; yellow lines in panels K, L). (F) Enlarged image of the CaD marked in panel E. The white asterisk identifies the hypoTD under the CaD (pointed by the white arrow in panels C, J). (G) En face choriocapillaris (CC) OCT structural image generated from a slab defined by segmentation boundaries at 4 to 20 µm below BM (yellow lines in panels K, L). (H) Enlarged CC structural image beneath the CaD marked in panel F, where the orange star corresponds to the same CaD area as identified with a white asterisk in panel F. (B, C, I, and J) B-scans located at the position marked by purple horizontal line in panels A, E-H without (panel B) and with segmentation boundaries to define subRPE (Panel I), and an enlarged view of the region containing CaD (Panels J, C). (K and L) corresponding B-scans with segmentation boundaries to define the CC slab. The white arrows in Panels C and J point to the shadows seen within the sub-RPE slab causing the hypoTDs appearance in panels E and F. The orange arrows in Panels C and L point to the hyperreflective scattering tail seen within the CC slab that

corresponds to the bright areas seen in panels G and H (marked by yellow star). Taken together, these OCT images show that CaD is associated with hypoTDs on the subRPE slab while simultaneously giving rise to a detectable OCT signal within the CC slab that corresponds to a hyperreflective scattering tail that extends below the CaD and involves the CC slab.

Figure 3.1.4 presents the OCT imaging characteristics of CaD. Enlarged images of the area underlying the CaD (Figure 3.1.4 C, H, I, K) show hypoTDs (white arrows) on the sub-RPE structural slab (Figure 3.1.4 C, H) and a hyperreflective scattering tail (orange arrows) on the CC structural slab and B-scans (Figure 3.1.4 E, I, K). These findings suggest an association between CaD, hypoTDs, and a hyperreflective scattering tail within the CC slab.

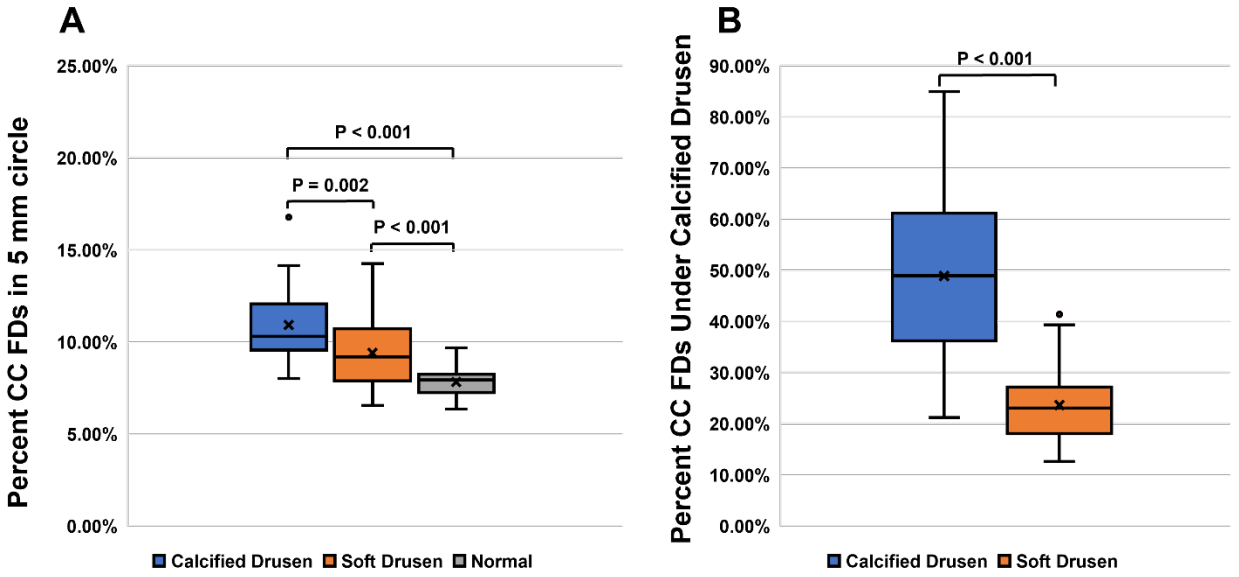

Figure 3.1.5. Comparison of the choriocapillaris flow deficits (CCFDs) among the three groups of eyes.

(A) Comparison of normal eyes, soft drusen eyes, and calcified drusen eyes within the fovea centered 5 mm circles. (B) Comparison of CCFDs underlying the soft drusen and calcified drusen.

Figure 3.1.5 shows the extent of CCFDs in the fovea-centered 5 mm circle in the three groups, specifically underlying the soft drusen and CaD. In the central 5 mm circle, the CCFD% underlying the CaD group exhibited a significant elevation compared with the soft drusen group (10.92% ± 1.88% versus 9.39% ± 1.78%, $p = 0.002$). Furthermore, the CCFD% underlying the soft drusen group exceeded that in the normal control group (9.39% ± 1.78% versus 7.82% ± 0.81%, $p < 0.001$). Notably, when quantified specifically

under the drusen, the CCFD% measurements underlying the CaD were markedly higher (48.87% ± 15.94%) than that observed under the soft drusen (23.63% ± 6.97%, $p < 0.001$).

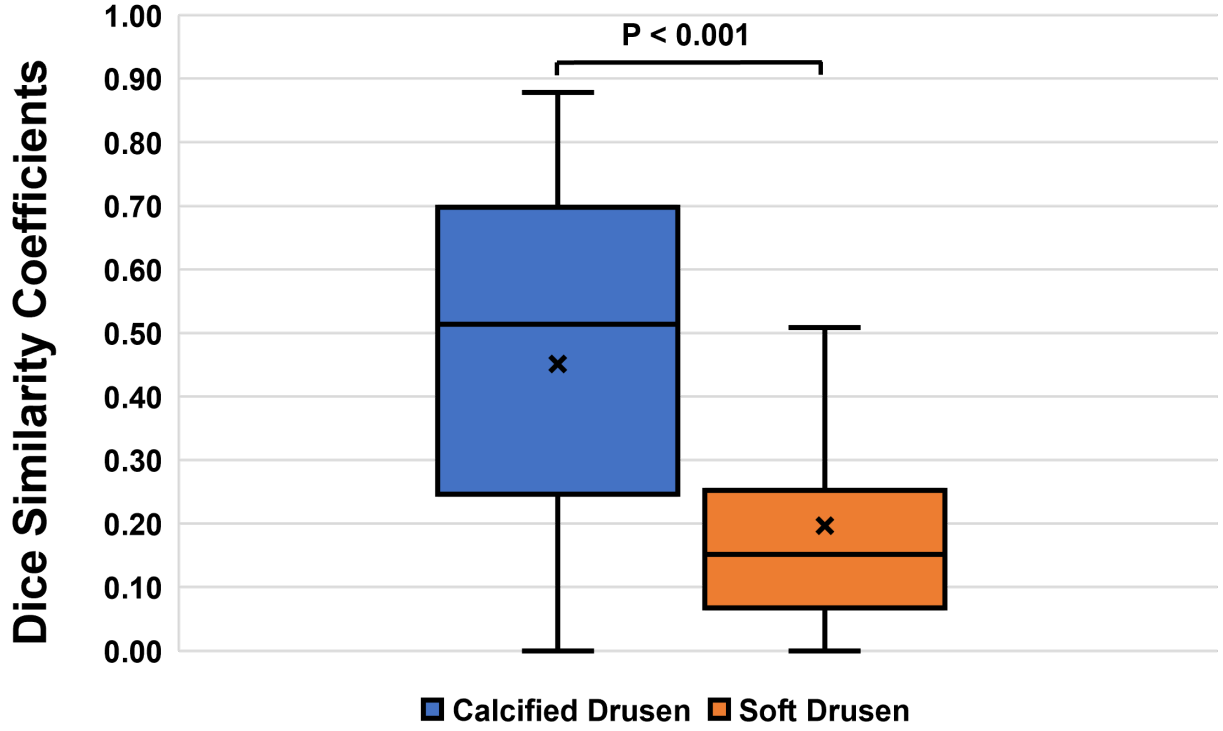

Figure 3.1.6. Dice similarity coefficients of choriocapillaris flow deficit density masks associated with calcified drusen and soft drusen masks.

Figure 3.1.6 shows the DSCs between the area masks of the different drusen types and the masks of the CCFDs obtained using the CCFD heat maps. The DSC served as an important metric to provide the correlation between the shape of CaD with the distribution of CCFD. In the context of CaD, the median DSC of CCFD density masks and CaD masks was computed at 0.51, with a mean value ± standard deviation of 0.45 ± 0.27. In the presence of soft drusen, the DSC of CCFD density masks and soft drusen masks was significantly lower, with a median of 0.15 and a mean ± standard deviation of 0.20 ± 0.18 ($p < 0.001$). This analysis emphasizes the intricate interplay between the CCFD density measurements and the presence of different drusen types.

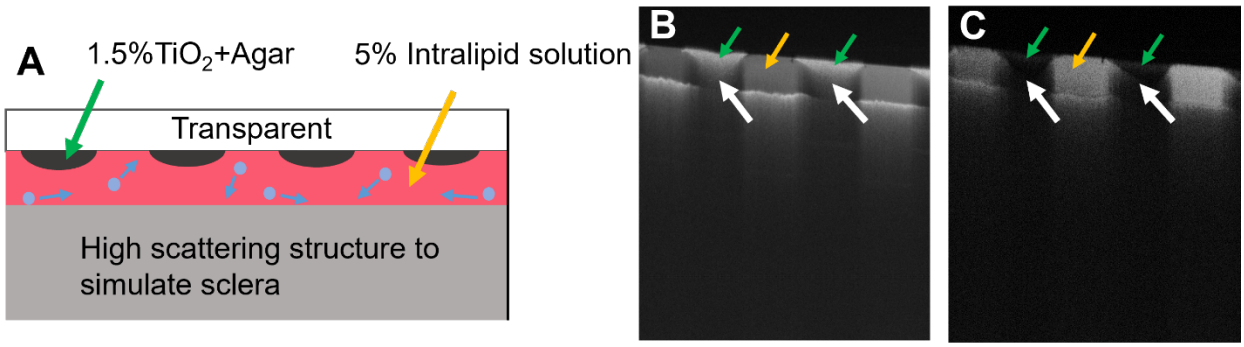

Figure 3.1.7. Phantom experiment to confirm the scattering tail due to highly scattering deposits that simulate calcified drusen demonstrating the inability to detect OCTA flow signals beneath the scattering lesions.

(A) Experimental phantom model consisting of three-layer layers where the upper layer is a transparent glass layer with droplets of highly scattering material deposited on a slide to simulate calcified drusen and then the slide was inverted, and the lesions appear on the bottom surface (green arrow) adjacent to the flowing intralipid. The droplet was made of solidified agar emulsion mixed with 1.5% TiO2 particles. The middle layer contains an empty channel, identified by a yellow arrow, to facilitate the infusion of a scattering liquid to mimic blood flow (5% Intralipid solution). The phantom's base is constructed from high scattering materials to simulate sclera. (B, C) Representative cross-sectional OCT structural image (B) and OCTA flow image (C) scanned from the phantom. The green arrows indicate areas with highly scattering droplets (mimicking calcified drusen), while the yellow arrows point to the flowing intralipid solution. Notably, the scattering tails (white arrows in B) are apparent beneath the droplet due to the increased scattering of light within the mass that increases the optical path length when detected by the OCT; however, in Panel C, the OCTA signals are not generated within the scattering tails where the flow should be present (white arrows), and this flow can be detected adjacent to the scattering tails (yellow arrows).

Figure 3.1.7 depicts the phantom model (Figure 3.1.7A) that simulated how a lesion, like a CaD with high light scattering properties (pointed by green arrows), can create a scattering tail (white arrows in Figure 3.1.7B) that would impact the detection of an angiographic flow signal underlying the lesion (white arrows in Figure 3.1.7C). The complex scattering of the light within the lesion leads to an increased optical pathlength which appears on the OCT image as if the light is reflected from a depth beneath the lesion. Consequently, an artifactual tail is created beneath the lesion (white arrows in Figure 3.1.7B). On the other hand, the highly scattering property of the lesion heavily attenuates the incident light, dramatically reducing the chance of that light penetrating the deeper layers. This attenuation leads to a loss of OCTA flow signal beneath the lesion, and the high light-scattering material makes it impossible to reliably detect useful OCT and OCTA signals from these underlying structures. This phenomenon was highlighted by the white arrow in Figure 3.1.7 C, where the existing real flow below the scattering lesion [136] is missing even though a signal

appears to be present based on the structural image (Figure 3.1.7B). However, the flow on either side of the scattering lesion can be detected. The results of this phantom study suggest that the detection of blood flow beneath the highly scattering lesion and within the tail cannot be reliably detected.

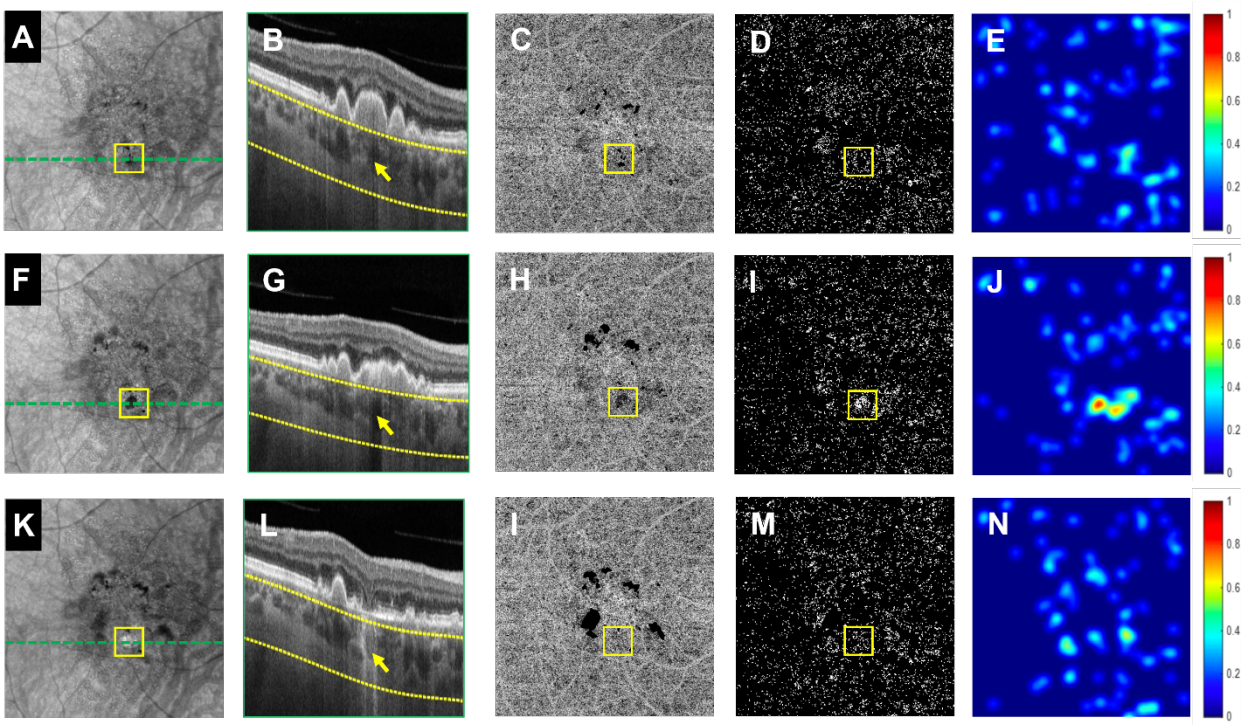

Figure 3.1.8. A representative case that evolved from a normal druse to a calcified druse to a hypertransmission defect (hyperTD) over a nine-month period.

Evolution of a normal druse to a calcified druse to a hypertransmission defect (hyperTD) with a loss choriocapillaris (CC) perfusion under the calcified drusen with reappearance of CC perfusion once the calcified druse resolves and the hyperTD appears. The yellow square identified the region containing the calcified druse of interest. (A-E) Soft drusen stage. (E-J) Calcified drusen stage. (K-N) HyperTD stage. (A, F, K) The en face subRPE images over time with the lesion's location indicated by the yellow square. (B, G, L) The OCT B-scans along the green dashed line in (A, F, K) highlighting the choroidal hypotransmission defect (hypoTD) resulting from the attenuation of light due to the calcified druse (F, G) followed by the hyperTD once the calcified druse resolves resulting in attenuation or loss of the retinal pigment epithelium and outer retina (K, L). (C, H, I) Compensated CC flow images in which hyperpigmentation and other calcified drusen outside the yellow square have been masked and excluded from the analysis. (D, I, M) The corresponding binary CC flow deficit (CCFD) maps. (E, J, N) The corresponding CCFD density heatmaps.

Figure 3.1.8 depicts the natural history of a lesion's transformation from soft drusen to the appearance of a CaD to the appearance of a hyperTD when imaged at 3-month intervals over 9 months. This case example illustrates the absence and then reappearance of CC flow once the calcified material is cleared. This case

also demonstrates an intriguing outcome showing that the appearance of the hyperTD was not associated with an increase in CCFDs. The fluctuations in CCFD% beneath the lesion are particularly noteworthy. An initial increase is observed from 10.15% (Figure 3.1.8D) to 15.34% (Figure 3.1.8I), followed by a subsequent decrease to 11.80% (Figure 3.1.8 M) [127]. This temporal pattern shows that the CC perfusion improves even as the lesion evolves into hyperTDs.

3.1.4 Discussion

The findings from this study highlight the impact of CaD on attempts to quantify CC perfusion. Although a structural signal from the CC layer can be detected under the CaD, this signal provides false depth information. Consequently, it cannot be used to extract OCTA information about blood perfusion because the signal within the scattering tail results from the highly scattering properties of the CaD itself, lacking any useful detectable flow signal. We hypothesize that the highly light-scattering properties of the calcium phosphate spherules within the CaD result in increased optical pathlengths of the light originating from the CaD, thereby forming a scattering tail directly below it. It is crucial to note that that OCT signal represents the detection of the light based on its optical pathlength to provide depth-resolved information. Hence, the artefactual illusion of depth information results from the delayed reflectance of light back to the detector due to the increased optical pathlength of the light originating within the CaD, caused by its high light-scattering properties. Consequently, the signal under the CaD does not arise from the CC layer but rather from within the CaD, so this signal lacks any flow information. Thus, when using the CCFD algorithm to detect CC perfusion, a decrease in CC perfusion under CaD, reported as an increase in CCFDs, is an artefact due to the absence of both structure and angiographic information from beneath the CaD. The scattering tail from the CaD provides a false structural signal in the CC layer, while in the deeper choroidal layers, the strong light attenuation due to the CaD causes a choroidal hypoTD that appears as a dark region on the en face subRPE structural slab. Unlike soft drusen, in which the OCT signal is mildly attenuated as it passes through the drusen and can be compensated for so that the CC perfusion can be quantitated [134], there is no real signal under the CaD that can be compensated. Therefore, CC perfusion cannot be quantified under CaD using current imaging technology and compensation strategies.

Our study evaluated 90 eyes, categorized into groups representing different drusen types and normal controls, and the observed variations in CCFD among these groups demonstrated the impact of CaD on the detection of CCFDs. Using the DSC and area analyses to quantitatively assess the relationship between CCFD and CaD, we demonstrated a strong correlation between CCFD density and CaD, reinforcing the erroneous belief that the presence of CaD is associated with decreased CCFD measurements [147]. Our results demonstrate the need to interpret OCTA data in regions affected by CaD cautiously and to consider the influence of these structures on CCFD quantification. While other studies have associated the decrease in

CC perfusion with drusen as a likely cause of drusen formation and disease progression [148–152], these studies must be viewed with extreme caution since these groups did not meticulously exclude the full extent of CaD from their analyses. This concern about the relationship between CCFDs and disease progression is demonstrated by the case depicted in Figure 3.1.8. When the soft druse was first present, the CCFDs could be quantified; however, once the druse developed calcifications, the CC FD% increased, but this increased CC FD% returned to its initial state once the calcified material resolved and a hyperTD formed. The return of CC perfusion highlights the artefactual nature of the presumed decrease in CC perfusion under CaD. While it may be possible to get restoration of CC perfusion once the calcification resolves, the more likely explanation is that the presence of the calcified material prevented the detection of the CC perfusion. Another observation was that we expected an increase in CC FD% once the hyperTD formed, but it is not what we found. Additional cases showing the evolution of hyperTDs need to be studied, but this case suggests that the RPE changes that result in the formation of a hyperTD are not preceded by a significant decrease in CC perfusion [123,153–156].

Our phantom experiment provided insight into the challenges posed by CaD-like structures in OCTA imaging. The experiment revealed that the presence of CaD introduces scattering tails that can obstruct the OCTA signals from underlying structures. The light attenuation due to high light-scattering material results in the absence of an OCTA flow signal beneath the lesion that cannot be compensated using the published strategy of inverting the decreased structural slab signal because the signal from the beneath the CaD is from the scattering tail and does not contain any structural or flow information. When the concentration of highly light-scattering material exceeds a certain threshold, the OCT and OCTA signals originating from structures underlying the lesion cannot be reliably detected because they are below the minimal OCTA detection range. This phenomenon aligns with our clinical observations, emphasizing the need for the identification of CaD and their exclusion from macular CC perfusion studies. While current CC algorithms can compensate for attenuated signals, the highly scattering calcium phosphate spherules along with their scattering tails present an unsolved challenge that prevents the accurate detection of blood flow patterns under CaD.

Limitations of our study include a small number of eyes in each group; however, considering the statistical significance of our findings, it is highly unlikely that our conclusions will change with additional eyes. Further studies with larger and more diverse cohorts would be useful to validate and extend our findings. While the qualitative nature of the phantom model appears to be consistent with our clinical observations, it is certainly possible that the properties of CaD are not analogous to a 1.5% TiO2 agar suspension. However, the phantom does unequivocally demonstrate the creation of a scattering tail and the impact of the scattering tail on the detection of an OCTA flow signal. We chose a simplified and cost-effective

phantom experiment to illustrate the inability of OCTA to detect flow beneath a highly light-scattering nodule-like deposit. A more sophisticated phantom model, capable of mimicking the scenarios of CaD within pathological and physiological contexts, would be necessary if the aim is to investigate how the scattering signals originating from CaD could be used to determine the physical composition of the drusen.

In summary, our findings underscore the necessity to carefully analyze and interpret CCFDs in eyes with CaD. The easiest way to identify the CaD is by examining the subRPE slab derived from a dense volumetric scan pattern of the macula. These CaD can be identified as choroidal hypoTDs and confirmed on corresponding B-scans to exclude areas of hyperpigmentation, which also cause choroidal hypoTDs. When quantifying CCFDs, it is essential to identify these regions and exclude these hypoTDs before compensating and thresholding the CCFDs to avoid introducing artefacts into the quantitation of CCFDs. The presence of CCFDs underlying CaD is not real but results from the increased light scattering properties of CaD. To further investigate the importance of CC perfusion as an OCT biomarker of disease progression in AMD, we must emphasize the need to identify and exclude these CaD before establishing any temporal relationship between the appearance of CC perfusion deficits and the progression of disease.

Chapter 3.2 Comparison between OCT B-scan and En Face Imaging for the Diagnosis of Early Macular Atrophy in Age-Related Macular Degeneration

3.2.1 Introduction

Historically, geographic atrophy (GA) was identified using fundus biomicroscopy or color fundus imaging and defined as the late stage of nonexudative age-related macular degeneration (AMD) [157]. GA is characterized by the degeneration of photoreceptors, retinal pigment epithelium (RPE), and choriocapillaris (CC), and is typically diagnosed as a sharply demarcated area of atrophy that originates in the perifoveal macula and progressively expands to encompass the entire macula [158] .

The advent of fundus autofluorescence (FAF) imaging largely supplanted color fundus imaging (CFI) for routine identification of macular atrophy in both clinical settings and research trials. However, FAF offers an indirect measure of atrophy, relying on the absence of intrinsic fluorophores that are lost as part of atrophy development. [159,160] In contrast, optical coherence tomography (OCT) has emerged as the preferred tool for directly detecting the anatomical changes in the outer retina and RPE that are associated with GA [57,133,161–163].

In AMD, FAF and OCT imaging each offer unique advantages, with FAF images capturing changes in hypoautofluorescence indicative of atrophy and changes of hyperautofluorescence predictive of disease progression. [159] However, OCT offers a detailed structural assessment, providing detailed information about the depth and layer involvement of atrophic regions, especially the earliest anatomic changes that predict the formation of GA.[143,161] While FAF and OCT imaging have been shown to be similar when identifying and quantifying established foci of GA, [164–167] there have not been many attempts to compare FAF and OCT detection of the earliest anatomic changes that precede the appearance of bona fide GA. [168]

To define the earliest changes that precede the appearance of typical GA, the Classification of Atrophy Meeting (CAM) group has advocated for the preferential use of OCT in diagnosing atrophy in AMD. They have developed consensus terminology based on OCT B-scan imaging, introducing the terms incomplete retinal pigment epithelium and outer retinal atrophy (iRORA) and complete retinal pigment epithelium and outer retinal atrophy (cRORA).[121,161] iRORA is characterized by three OCT features: photoreceptor degeneration, RPE attenuation or disruption, and increased choroidal signal transmission. In addition, cRORA includes these features but also mandates that the areas of RPE change and choroidal hypertransmission each have a measurement of at least 250 μm on the horizontal OCT B-scan, along with evidence of photoreceptor loss. iRORA is proposed as a precursor to cRORA and was proposed to represent a precursor lesion to GA that would be helpful in monitoring disease onset and progression. [169]

To define cRORA, the use of the 250 μm horizontal dimension cut-off for the loss or attenuation of RPE and its accompanying choroidal hypertransmission defect (persistent s) was not based on any natural history study, but rather as a dimension that could be reliably and reproducibly measured. [161] This OCT biomarker for the detection of early macular atrophy is primarily reliant on the analysis of B-scans for defining iRORA and cRORA. It is important to acknowledge that the orientation of the B-scan in relation to the size and location of the atrophic area may impose constraints on the consistent and reliable identification of iRORA. This limitation is crucial for interpreting biomarker efficacy and suggests a need for refined methodologies in OCT imaging. [170] Furthermore, recent studies suggest that intergrader reliability is lower for evaluating iRORA compared with cRORA on B-scans, [169] and 50% of iRORA was found to correspond to cRORA when the lesions were graded in a non-horizontal dimension. [171]

Another strategy for detecting OCT lesions that correspond to GA lesions and for detecting early stage OCT changes that precede the formation of GA is to use en face OCT images derived from dense OCT raster scans. [120,143,143,154,164,171–174] The use of en face persistent choroidal hyperTDs has been proposed as an alternative to using averaged B-scans for the diagnosis of early-stage lesions. [120,143,171,174] This en face strategy using dense volumetric raster B-scans allows for the measurement of hyperTDs in any en face dimension, not just the horizontal dimension. En face OCT detects macular atrophy, including GA, due to the increased choroidal light penetration and reflectivity that results when the highly reflective RPE layer is attenuated or lost, leading to abrupt transition in OCT choroidal reflectivity.[120,164,172,173] These hyperTDs, with a minimum size of 250 μm, have been shown to be persistent and identified as precursors to the formation of typical GA, but diagnosed on en face OCT imaging. [120,139,154] Recent studies indicate that hyperTDs can serve as standalone biomarkers for predicting the progression from drusen to atrophy. [143,174]

With the introduction of OCT B-scan diagnostic definitions of iRORA and cRORA and the introduction of persistent choroidal hyperTD diagnosed on en face OCT images, a lingering question that needed to be addressed is how these different OCT definitions of early atrophy could be reconciled. In their recent study, Corvi et al. [122] reported that there is significant agreement between the B-scan diagnoses of cRORA when compared with the diagnoses of persistent hyperTDs on en face OCT images. However, they found that about 50% of cases initially diagnosed as iRORA were actually cRORA when assessed in the non-horizontal dimension using en face OCT imaging. Since cRORA indicates a complete loss of photoreceptors, the results by Corvi et al [122] indicate that hyperTDs on en face imaging correlates with cRORA, which should correlate with a loss of function.

While Corvi et al [122] primarily focused on eyes with established GA, it was reported that the discrepancies between the grading systems mainly occurred in smaller atrophic areas. Given this background and the evidence that the diagnosis of persistent choroidal hyperTDs on en face images from dense OCT raster

scans can be easily and reliably graded, [10] we wanted to confirm the equivalency between hyperTDs on en face imaging and cRORA on B-scan imaging. We also wanted to improve the diagnosis of iRORA on B-scan imaging by showing that more closely spaced, averaged B-scans were better at distinguishing iRORA from cRORA once neighboring B-scans were graded along with any given B-scan. This would enable graders to identify when when conventionally graded iRORA is really cRORA when viewed in a non-horizontal greatest linear dimension (GLD). This report compares the grading of cRORA and iRORA from a dense scan pattern of averaged SD-OCT B-scans against the grading of persistent choroidal hyperTDs from SS-OCTA en face OCT images.

3.2.2 Methods

Study Design and Ethical Approval

This retrospective analysis of a prospective, observational study used two different OCT imaging techniques to investigate early atrophic lesions in nonexudative AMD. The study was a collaboration between the Moran Eye Center, Bascom Palmer Eye Institute, and Tel Aviv Medical Center. Ethical clearance was obtained from the University of Tel Aviv's ethics committee, and all subjects were enrolled at the Tel Aviv Medical Center. The study was conducted in strict adherence to the principles outlined in the Declaration of Helsinki and was compliant with the Health Insurance Portability and Accountability Act (HIPAA) of 1996. All participants provided informed consent prior to enrollment.

Study Period and Participant Selection

The study was conducted from 2022 to 2023. Consecutive patients presenting to the Macula Center within the Ophthalmology Department at Tel Aviv Medical Center were included if they had at least one eye affected by GA secondary to nonexudative AMD. The diagnosis was confirmed through standard structural OCT imaging.

Exclusion Criteria

Patients were excluded from the study if they had a history of other retinal pathologies, including but not limited to diabetic retinopathy, retinal vein occlusion, and central serous chorioretinopathy. Additionally, patients were ruled out if there was any evidence of exudation, which was defined as the presence of subretinal or intraretinal fluid as observed on structural OCT B-scans or retinal thickness maps.

Imaging Protocols

All enrolled participants underwent 6x6 mm macular scans using both the Spectralis SD-OCT (Heidelberg, 512x97, ART:9) and the SS-OCTA (PLEX® Elite 9000, Carl Zeiss, Meditec Inc., Dublin, CA, 500x500

angio pattern) instruments on the same day. The Spectralis SD-OCT operated at a central wavelength of 880 nm and had a scanning rate of 85,000 A-scans per second. The scanning pattern for the SD-OCT imaging included a 20-degree field of view with 512 A-scans per B-scan and utilized the high-speed raster scan pattern consisting of 97 B-scans with an automatic real-time-tracking (ART) setting of 9 per volume resulting in a B-scan interval of 62 μm. The SS-OCTA device operated at a central wavelength of 1050 nm and had a scanning rate of 100,000 A-scans per second. The scanning pattern consisted of 500 A-scans per B-scan, with each B-scan acquired twice at the same position. The study exclusively included 6x6-mm scans centered on the fovea, resulting in a uniform 12 μm spacing between A-scans and B-scans. All acquired images underwent a quality assessment. Scans with evident motion artifacts or with a signal strength rating below 7 out of 10 on the device's scale were excluded from the subsequent analysis.

Image Processing

En face SS-OCTA images were created from a sub-RPE slab with segmentation boundaries between 64-400 μm beneath Bruch's membrane and referred to as a subRPE slab. HyperTDs with a GLD of at least 250 μm were graded and tracked across multiple visits. For the SS-OCTA scans, the grading of en face images to identify hyperTDs at least 250 μm in GLD was conducted collaboratively by the University of Washington and Bascom Palmer Eye Institute. A previously developed artificial intelligence (AI)-assisted algorithm [57,137] was used to facilitate the identification of hyperTDs using SS-OCT. The semi-automated algorithm integrated data from OCT structural information, optical attenuation coefficients (OAC) signals, and drusen elevation to enhance the segmentation of hyperTDs, as illustrated in Figure 3.2.1F. The software excluded all lesions with a GLD of less than 250 μm from the final hyperTDs mask. Additionally, the software calculated and recorded the area of each individual hyperTD and the cumulative area of all lesions. Two independent graders meticulously reviewed and manually graded the en face hyperTDs and the corresponding choroidal hyperTDs on the B-scans for the grading. A consensus outline from these evaluators was adopted for subsequent analyses. In cases where agreement could not be reached, a senior evaluator was consulted (PJR).

For the SD-OCT B-scans, en face images were also created from the subRPE slab. Raw OCT cubes were extracted from the e2e files using the Heidelberg OCT review software. Inter-frame registration and intensity normalization were conducted to compensate the eye motion and uneven illumination. A contrast-limited adaptive histogram equalization filter was applied to the en face image to enhance the contrast of the image.

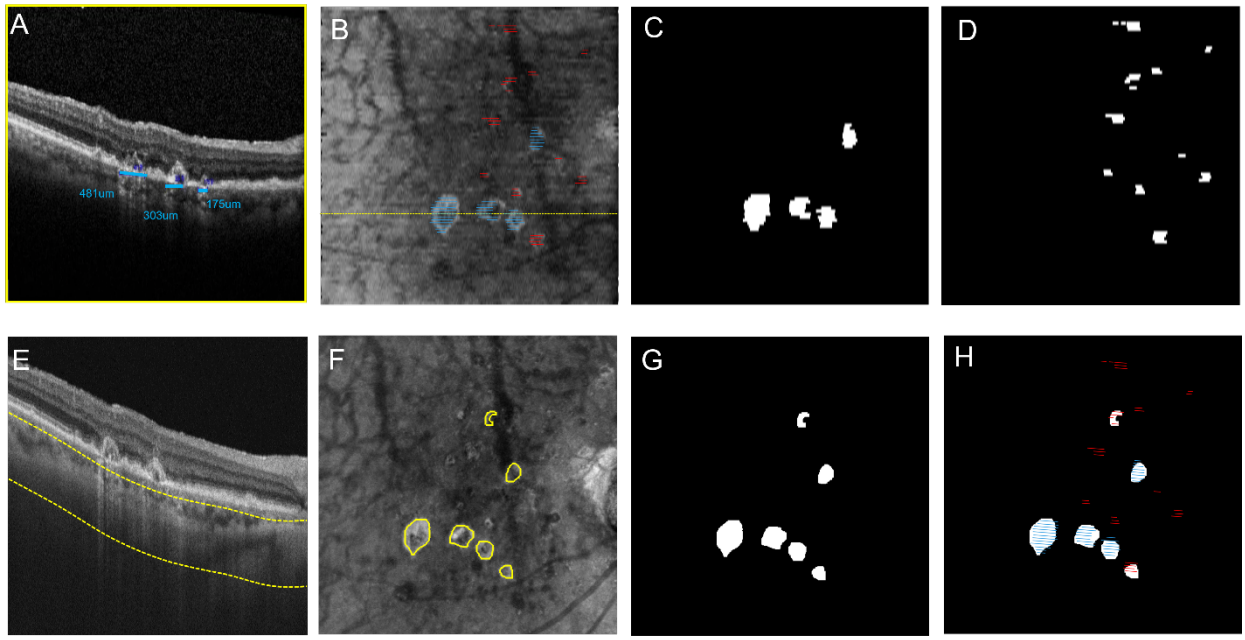

Figure 3.2.1. Identification of incomplete retinal pigment epithelium and outer retinal atrophy (iRORA) and complete RORA (cRORA) in a representative Eye using SD-OCT and SS-OCT Instruments.

(A) SD-OCT B-scan with blue lines denoting iRORA and red lines denoting cRORA. The position of this B-scan is shown by the yellow dashed line in (B). (B) En face image of the sub-retinal pigment epithelium (subRPE) slab obtained from the SD-OCT scan. Persistent choroidal hypertransmission defects (hyperTDs) are visible across the entire scan area with the overlay of lines corresponding to cRORA and iRORA. (C) An en face cRORA mask was generated based on B-scan gradings. (D) An en face iRORA mask was generated based on its B-scan gradings. (E) hyperTD lesions with the red line indicating the segmentation of the internal limiting membrane, RPE, and Bruch's membrane. (F) The en face view of the sub-RPE slab from the SS-OCT, featuring superimposed grading marks for hyperTDs. (G) Binary images of persistent hyperTD lesions from the SS-OCT system, automatically identified by a validated and automated algorithm calculation, with a greatest linear dimension (GLD) $\geq$ 250 µm. (H) The binary mask of hyperTDs, including the SD-OCT B-scan gradings of cRORA and iRORA, registered and overlaid.

Using SD-OCT B-scans, a masked grader (MF) at the Moran Eye Center identified cRORA and iRORA lesions. The review software within the SD-OCT machine was used by graders to identify choroidal hyperTDs, outer retinal changes, and RPE attenuation. cRORA was labeled when the hyperTDs in the B-scan plane met one of the following criteria: 1) lesion size was at least 250 µm; or 2) lesion was connected to another lesion that was at least 250 µm in size; or 3) lesion was linked to more than four adjacent lesions on OCT B-scans, resulting in a GLD exceeding 250 µm along the slow scan direction. Similarly, hyperTDs were categorized as iRORA when their size was smaller than 250 µm in both the fast and slow scan directions. Once the grading was complete, the masks of cRORA and iRORA were projected and

superimposed onto the subRPE slab of the SD-OCT scans as shown in Figure 3.2.1A and 3.2.1B. The resulting masks and their respective areas were calculated for further analysis as depicted in Figure 3.2.1C and 3.2.1D.

The iRORA/cRORA mask created from the SD-OCT images was manually registered to the SS-OCT images to minimize the distortion and lesion mismatch between the OCT systems (see Figure 3.2.1I). The number of iRORA/cRORA lesions that overlaped with the persistent hyperTDs on en face SS-OCTA images were recorded based on the registered image.

Statistical Analyses

The total area of the cRORA and the hyperTDs were compared by paired-samples t test. Statistical analyses were conducted using MATLAB R2021. The data were summarized with mean and standard deviation, if applicable. A two-sided P value less than 0.05 was considered statistically significant.

3.2.3 Results

Study Population and Analysis of SD-OCT and SS-OCTA Scans

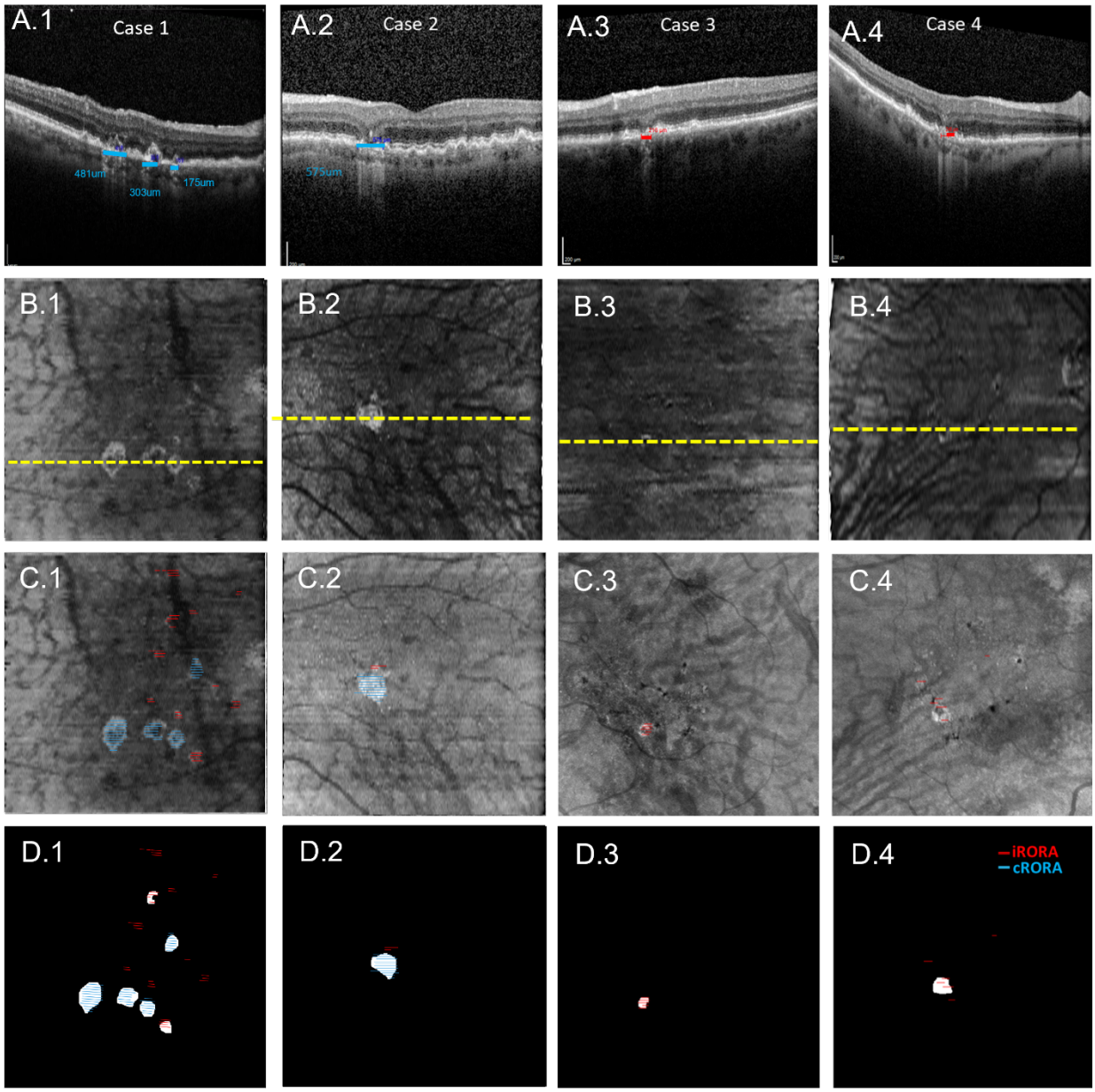

Figure 3.2.2. Four representative cases used to grade iRORA, cRORA, and persistent choroidal hyperTDs.

(A.1-A.4) SD-OCT B-Scans (512x97) with grading of cRORA (blue) and iRORA (red) (B.1-B.4) SD-OCT en face subRPE slab with the yellow dashed line representing the location of the B-scan in panel (A). (C.1-C.4) SS-OCT subRPE slabs with scan size 500x500 overlay with corresponding SD-OCT B-Scan projected gradings (D.1-D.4). HyperTD algorithm mask overlays with b-scan gradings. In case 1, cRORA was correctly identified in 100% (34/34) of gradings, while iRORA was correctly identified in 71.3% (20/28) of gradings. In case 2, cRORA was correctly identified in 100% (11/11) of gradings and iRORA was correctly identified in 100% (2/2) of gradings. In case 3,

iRORA was not identified correctly in any of the gradings (0%, 0/5). In case 4, iRORA was correctly identified in 50% (3/6) of gradings.

A retrospective analysis identified 19 eyes from 15 patients diagnosed with nonexudative AMD and exhibiting persistent choroidal hyperTDs on SS-OCTA en face images. These patients had undergone same day SD-OCT and SS-OCTA imaging between the years 2022 and 2023. Within the collected dataset, 558 SD-OCT B-scans exhibited cRORA, while 142 B-scans were categorized as having iRORA. The mean area of single hyperTD lesion measured on the en face image was 0.64 ± 1.28 mm2, with a maximum of 5.16 mm2 and a minimum of 0.02 mm2. The mean GLD of a single hyperTD lesion was 0.81 ± 0.83 mm, with a maximum of 3.30 mm and a minimum of 0.25mm.

Consensus Grading and Overlap Analysis

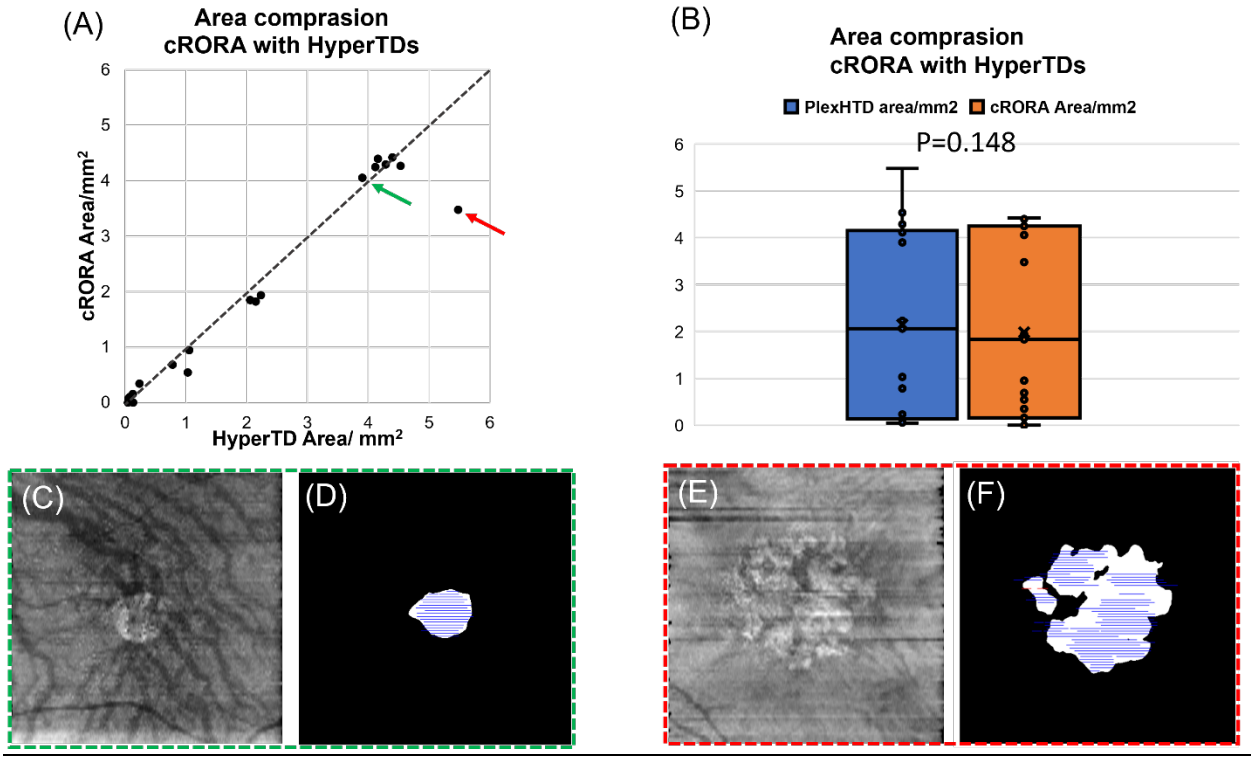

Figure 3.2.3. Comparison of total area measurements for cRORA on SD-OCT scans and persistent choroidal hyperTDs on SS-OCTA scans.

(A) Correlation plot illustrating the relationship between area measurements of cRORA and hyperTDs. The dash diagonal line represents the line of unity (slope=1), indicating a strong correlation between the two measurements (r2=0.938 (B) The box plot compares the areas of cRORA and hyperTDs, with a mean area of 1.98 mm² for cRORA and 2.14 mm² for hyperTDs. The p-value for the comparison of the areas of inner retinal outer retinal atrophy (iRORA) and cRORA is 0.148. (C-D) The representative case indicated by the green arrow. (C) The subRPE slab of the SD-OCT. (D) The hyperTD mask of SS-OCT overlay by the grading of cRORA and iRORA. (E-F) The outlier case as shown by the red arrow in panel (A). (F) shows the subRPE slab of the SD-OCT, while (G) displays the hyperTD mask of SS-OCT overlay with the grading of cRORA and iRORA.

Consensus iRORA/cRORA gradings and the en face hyperTD gradings were performed by the designated evaluators. There was a near-perfect overlap between SD-OCT cRORA lesions and SS-OCTA persistent hyperTDs. Specifically, 556 out of the 558 cRORA lesions identified through SD-OCT imaging were also detected as persistent hyperTDs with a GLD of at least 250 μm in GLD on SS-OCTA en face images (556/558; 99.6%). To further elucidate the correlation between cRORA and hyperTD lesions, area measurements from the cRORA mask obtained from the SD-OCT scans were compared with the en face images of the hyperTDs from the SS-OCTA scans as shown in Figure 3.2.3. The average area per scan for cRORA was 1.98 ± 1.77 mm², while hyperTDs had a slightly larger mean area of 2.14 ± 1.87 mm². A strong correlation (R^2 = 0.938) was noted between the two sets of area measurements and the difference in measurements was not statistically significant (P= 0.148). In Figure 3.2.3, the dashed diagonal line represents the line of unity (slope=1) and shows the correlation between area measurements of the cRORA on SD-OCT and hyperTD on SS-OCT imaging. A representative case was pointed out by the green arrow in Figure 3.2.3 and was shown in (C-E), while an outlier case was indicated by the red arrow and shown in Figure 3.2.3 (F-H).

Additional Observations

Interestingly, 72.5% of iRORA lesions (103/142) were not accompanied by any persistent hyperTDs on en face images, but this would be expected since iRORA lesions measure less than 250 μm even when neighboring B-scans are included. A lesion with a hyperTD measuring less than 250 μm in GLD would not be considered a persistent hyperTD. Conversely, 27.4% of iRORA lesions (39/142) were classified as persistent hyperTDs when they were part of larger lesions. Among 39 iRORA lesions that classified as hyperTDs, the average length measured on B-scans was 179.1 ± 48.7um. These observations are illustrated in four representative cases shown in Figure 3.2.2. In Case 1, if we define cRORA as a lesion that measures 250 μm or greater in any GLD and iRORA as a lesion that measures less than 250 in any GLD, then cRORA was accurately identified in 100% of the gradings (34/34), while iRORA was correctly identified in 71% of the gradings (20/28). In Case 2, cRORA was identified accurately in all gradings (11/11; 100%), and

iRORA was correctly identified in 100% of the gradings (2/2). In Case 3, none of the iRORA lesions were correctly identified (0%, 0/5). In Case 4, iRORA was correctly identified in 50% of the gradings (3/6).

3.2.4 Discussion

We compared the grading of cRORA and iRORA on B-scans with the grading of persistent hyperTDs observed on en face images. The results of this grading exercise indicated that cRORA grading on B-scans was almost identical to the grading of persistent hyperTDs on en face images. This is to be expected since persistent choroidal hyperTDs on en face imaging have a GLD of at least 250 µm so this would include all cRORA lesions graded on horizontal B-scans. However, grading of iRORA based solely on horizontal B-scans, even when considering the neighboring B-scans, does not fully distinguish iRORA from what is actually cRORA when the GLD of choroidal hypertransmission is larger than 250 µm in a non-horizontal dimension. Upon examination in a non-horizontal dimension, it was discovered that 27% of iRORA lesions detected on B-scans were actually cRORA lesions. These iRORA lesions would likely have been recognized correctly as persistent hyperTDs on en face images since they were situated within a larger lesion that would be diagnosed as cRORA when viewed non-horizontally.

En face OCT imaging offers several advantages over B-scan evaluation for diagnosing cRORA and identifying when iRORA lesions are really cRORA lesions. The ability to inspect a single en face image for the presence of persistent hyperTDs considerably expedites the assessment process, providing a fast overview of the entire scan area as compared with meticulous scrolling through each of the 97 B-scans from a raster volume scan. Moreover, en face imaging provides valuable insights into the topographic correlation of atrophic lesions with other anatomic features that are related to AMD progression such as the location of drusen and hyperreflective foci (HRF). [175,176] Our results also suggest that iRORA lesions can be correctly classified as cRORA when closely spaced neighboring B-scans are considered. A retrospective, cross-sectional study that evaluated the correlation between FAF and en face SD-OCT measurements of GA area associated with AMD showed a robust correlation between FAF and en face SD-OCT measurements of GA area ($r = 0.98$; $P < 0.001$), particularly after manual correction of SD-OCT segmentation errors. [166] However, when Corvi et al [170] compared B-scan diagnoses of cRORA and iRORA with en face OCT images, they found that approximately 50% of iRORA lesions were actually cRORA lesions on en face images, but they did not include neighboring B-scans when grading iRORA. In our current study, the B-scan grader specifically included neighboring B-scans when grading iRORA and cRORA, and even with the inclusion of these neighboring B-scans, 27.4% of iRORA lesions were actually cRORA lesions on en face images. In an analysis from our current dataset in which neighboring B-scans were not considered when grading

iRORA lesion, we found that approximately 50% of the iRORA lesions were found to be cRORA lesions. These findings further support the potential of en face OCT imaging in identifying lesions as they progress to typical GA. The application of en face imaging is not only useful for clinical research and clinical trials, but also a valuable tool for assessing disease severity and treatment outcomes in clinical practice in which a single OCT can be used to follow both exudative and nonexudative AMD.

Our study, which specifically uses a SD-OCT instrument capable of producing averaged OCT B-scans, takes advantage of an enhanced ability to detect iRORA lesions compared with an instrument that does not produce averaged B-scans, as previously described by Corvi et al. in which they evaluated the detection of iRORA between two such devices. [170]

Limitations of this investigation include the small sample size; however, it is unlikely that the inclusion of additional eyes would significantly alter the observed similarities between hyperTDs and cRORA detection or the limitations in iRORA detection and the need to grade neighboring B-scans when grading iRORA. Additionally, the current hyperTD detection algorithm is specifically designed for dense SD-OCTA and SS-OCTA scans, and our results also support the need for a dense scanning pattern when grading cRORA and iRORA lesions on all OCT instruments. However, as suggested here, subRPE en face images can be generated as long as a dense SD-OCT scan pattern can be performed, and we recommend a minimum of 97 B-scans over a 6X6 mm field-of-view.

In conclusion, our research highlights the critical importance of thoroughly evaluating choroidal hyperTDs in all neighboring B-scans when classifying iRORA lesions using a dense OCT B-scan imaging pattern to determine when iRORA lesions are really cRORA lesions. In contrast, en face OCT imaging facilitates the detection of persistent hyperTDs, which are equivalent to cRORA lesions. To ensure accurate differentiation between iRORA and cRORA when grading B-scans, it is essential to examine adjacent B-scans for a comprehensive understanding of the extent of choroidal hyperTDs and the accompanying changes in the RPE and outer retina. Most notably, detection of persistent hyperTDs on en face images is much easier than scrolling through 97 or more B-scans to identify these lesions. Additionally, the use of automated algorithms to identify persistent hyperTDs improves the efficiency of lesion detection, streamlining the diagnostic process.

Chapter 4. Developing Automated Biomarker Detection Techniques for Age-related Macular Degeneration Using OCT and OCTA Imaging

In this chapter, we address the need for automated techniques in the detection and quantification of biomarkers for age-related macular degeneration (AMD) using OCT and OCTA. AMD is a leading cause of vision loss among the elderly, and early detection of biomarkers, particularly hyperreflective foci (HRF), has a strong correlation of the progression to the geographic atrophy (GA). This chapter presents innovative computational approaches that leverage machine learning and image processing to refine the diagnostic process and enhance the accuracy and efficiency of biomarker assessment in clinical settings.

Section 4.1 focuses on the automatic segmentation of geographic atrophy in both SD-OCT and SS-OCT scans using deep learning. GA characterized by the loss of photoreceptors, retinal pigment epithelium (RPE), and choriocapillaris, is a significant indicator of late-stage nonexudative AMD. The complexity and variability of atrophy present unique challenges in its detection and quantification. This section discusses the development of a machine learning model that utilizes optical attenuation coefficients (OACs) derived from OCT data to accurately identify and measure areas of atrophy, thus facilitating a more robust analysis of disease progression and treatment efficacy.

Section 4.2 delves into depth-resolved visualization and automated quantification of HRF on OCT scans. HRF, associated with cellular migration and aggregation in the retina, are crucial biomarkers for assessing the risk of progression from intermediate to late AMD. The section introduces a new algorithmic approach that uses OACs to enhance the contrast of these lesions in OCT images, enabling segmentation and quantification of pigment burdens within the retina and RPE. By automating the segmentation and quantification process, this methodology seeks to reduce the labor-intensive aspects of manual image analysis and improve the reliability of assessments related to disease severity and progression.

Chapter 4.1 Automatic segmentation of geographic atrophy in both SD-OCT and SS-OCT scans using deep learning

4.1.1 Introduction

Geographic atrophy (GA), also known as complete RPE and outer retinal atrophy (cRORA) [161], forms in the late stage of nonexudative age-related macular degeneration (AMD) and is characterized by the loss of photoreceptors, retinal pigment epithelium (RPE) and choriocapillaris (CC) [161,177]. GA is estimated to affect approximately 5 million people globally, and its prevalence increases exponentially with age [178,179]. It

remains a leading cause of irreversible vision loss worldwide [180,181]. Currently, there are several clinical trials underway using complement inhibitors for the treatment of GA, where the growth rate of GA area is used as the primary study endpoint [182–185]. An automated and accurate approach to identify, segment, and quantify GA would be of great interest and importance for following these patients in clinical practice and confirming the effectiveness of treatments in clinical trials.

Historically, GA was defined as sharply demarcated area of apparent hypopigmentation on color fundus imaging (CFI), but with current technological advancement, fundus autofluorescence (FAF) and optical coherence tomography (OCT) have become more widely used in clinical practice and clinical research to identify and measure GA [30,120,153,154,173,186–189]. Both modalities have their own advantages as FAF contrasts RPE pigmentation by visualizing ocular fluorophores such as melanin and lipofuscin [179], while OCT provides depth-resolved information using both spectral domain OCT (SD-OCT) and swept-source OCT (SS-OCT). From the OCT datasets it is possible to define custom slabs under the RPE based on boundary specific segmentation that allows for the visualization of defined anatomical regions. One custom slab, known as the sub-retinal pigment epithelium slab (subRPE slab), can produce *en face* images that specifically accentuate the choroidal hyper-transmission defects (hyperTDs) that arise when the RPE is attenuated or absent [120,164,173,190].

Several automatic algorithms have been developed using various imaging approaches to segment GA and calculate GA areas. These include computer vision and traditional machine learning approaches like region-based Chan-Vese model [191], random forest classifier [191], and fuzzy c-means clustering [192] as well as modern deep learning approaches like sparse autoencoders [193,194], convolutional neural networks (CNNs), [195–198] and a generative adversarial network (GAN) [199]. Overall, these published works demonstrated good agreement with human graders and they achieved satisfactory DICE similarity coefficients (DSCs), ranging from 0.68 to 0.89.

In this study, we propose a new deep learning approach to identify, segment, and quantify GA area using optical attenuation coefficients (OACs) calculated from OCT datasets. We introduce novel *en face* OAC images to identify and visualize GA and a CNN model for the task of automatic GA identification and segmentation.

4.1.2 Methods

The OCT images used to develop, train, and test the algorithm were acquired as part of a prospective study performed at the University of Miami and approved by the Institutional Review Board of the University of Miami Miller School of Medicine, in adherence to the tenets of the Declaration of Helsinki and the Health Insurance Portability and Accountability Act of 1996 regulations. Normal subjects and subjects diagnosed

with GA secondary to nonexudative AMD were enrolled from June 2016 to November 2019 with informed consents obtained before participation.

Imaging acquisition

All subjects underwent SS-OCT scanning (PLEX Elite 9000, Carl Zeiss Meditec, Dublin, CA). This instrument uses a 100 kHz light source with a 1050 nm central wavelength and a 100 nm bandwidth, resulting in an axial resolution of ~ 5.5 μm and a lateral resolution of ~20 μm estimated at the retinal surface. 6 × 6 mm scans were acquired at the baseline visit, at six month follow-up visits, and at one year follow-up visits as previously described [154]. For each 6 × 6 mm scan, there are 1536 pixels on each A-line (3 mm), 500 A-lines on each B-scan, and 500 sets of twice repeated B-scans. Scans with a signal strength less than 7 or evident motion artifacts were excluded from further data analysis.

Image processing

A depth-resolved single scattering model was applied to calculate OAC for each pixel in the volumetric SS-OCT dataset [200,201].

An automatic proprietary segmentation algorithm (Carl Zeiss Meditec, Dublin, CA) was used to identify the lower boundary of retinal nerve fiber layer (RNFL) and Bruch's membrane (BM) on the volumetric SS-OCT data. These segmentation lines were then applied to the volumetric OAC data using MATLAB version R2016b software (MathWorks, Natick, Massachusetts). Two separate slabs were defined to generate *en face* images for the GA visualization and segmentation. The first slab was defined as RNFL to BM, as shown between the red dashed lines on an OAC B-scan in Figure 4.1.1 (A). For this slab, four different *en face* OAC images were automatically generated: the maximum projection image (OAC max image as shown in Figure 4.1.1 (B)), the sum projection image (OAC sum image as shown in Figure 4.1.1 (C)), the RPE to BM distance map (the OAC elevation map as shown in Figure 4.1.1 (D), (E)), and the false color OAC image, which is a composite using different OAC images in each color channel, i.e., the OAC max image in the red channel, the OAC sum image in the green channel, and the OAC elevation map in the blue channel, as shown in Figure 4.1.1 (F), as previously described in detail [202]. The position of the RPE is defined as the pixel with the maximum OAC value above BM along each A-line and the OAC elevation map represents the distance between the RPE and BM. A 5 × 5 pixel median filter was used for smoothing to reduce the noise appearance in the image. Green dashed lines in Figure 4.1.1 (D) show an example of this RPE-BM distance on an OAC B-scan. The second slab, also known as the subRPE slab, was defined as extending from 64 μm below BM to 400 μm below BM, and it is shown between the yellow dashed lines in Figure 4.1.1 (G). For this subRPE slab, an *en face* OCT image was also automatically generated, as shown in Figure 4.1.1 (H), using the sum projection. GA lesions (Figure 4.1.1 (I)) were manually outlined

using this *en face* subRPE OCT image, referencing B-scans, by two independent graders (Y.S. and L.W.) using Photoshop CC (Adobe Systems, San Jose, California, USA), and consensus boundaries were reached between both graders. In cases of disagreement, a senior grader (P.J.R.) served as the adjudicator, as described in previous studies [18]. All images were resized to 512 × 512 pixels.

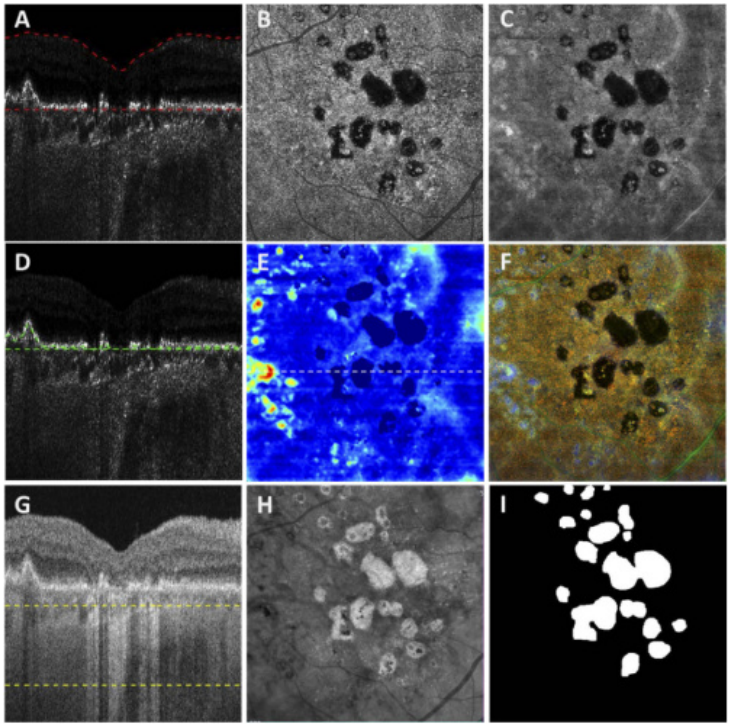

Figure 4.1.1. Representative images obtained using the optical attenuation coefficient (OAC) algorithms and the traditional OCT images with choroidal hypertransmission defect (hyperTDs).

A: Swept-source OCT (SS-OCT) OAC B-scan with red dashed lines of the first slab, from the lower boundary of retinal nerve fiver layer to Bruch's membrane (BM); B: OAC maximum projection *en face* image of the first slab. C: OAC sum projection *en face* image of the first slab. D: OAC B-scan with green dashed lines indicating the distance between OAC identified retinal pigment epithelium (RPE) and BM. E: OAC elevation map calculated using the BM segmentation of the first slab to the OAC line shown in panel D with the distance from the RPE to BM. The map is shown in color with a dynamic range of 0-120 (µm). F: OAC false color composite image of panels B (red channel), C (green channel) and E (blue channel). G: The same SS-OCT B-scan image as panel A with yellow dashed lines depicting the second slab from 64 µm below BM to 400 µm below BM, also known as the subRPE slab. H: OCT sum *en face* projection of the subRPE slab depicting the area with choroidal hyperTDs. I: Ground truth area of geographic atrophy shown in panel H and identified by graders. All B-scans were flattened based on BM segmentation.

Deep learning model

To perform the GA segmentation task, 2 deep learning models were trained using the same U-Net architecture with different input images, namely, the composite OAC false color images and the *en face* OCT subRPE images. The U-Net model architecture is shown in Figure 4.1.2 with specifications all labeled. The only difference for the two models is the input layer, one with a 3 channel image and the other one with a 1 channel image. Training used 80% of all eyes, and testing used 20% of the eyes. Within the training cases, there is also an 80:20 split between training and validation, partitioned at the eye level. Cases were shuffled and the set division was completely random. The hyper-parameters (learning rate, dropout and batch normalization) for the training process were tuned on the validation set using grid search. In the training process, data augmentation with zoom, shear, and rotation was implemented and a batch size of 8 was used. For each 3 × 3 convolution block, the He normal initializer [203] was used for kernel initialization. The Adam optimizer was used and the model evaluation metric was defined as the soft DSC (sDSC). Each model was trained with 200 epochs with a patience for early stopping of 50 epochs, and only the model with the best metric was saved. The models were implemented in Keras using Tensorflow as the backend, and training was performed with a 16GB NVIDIA Tesla P100 GPU through Google Colab.

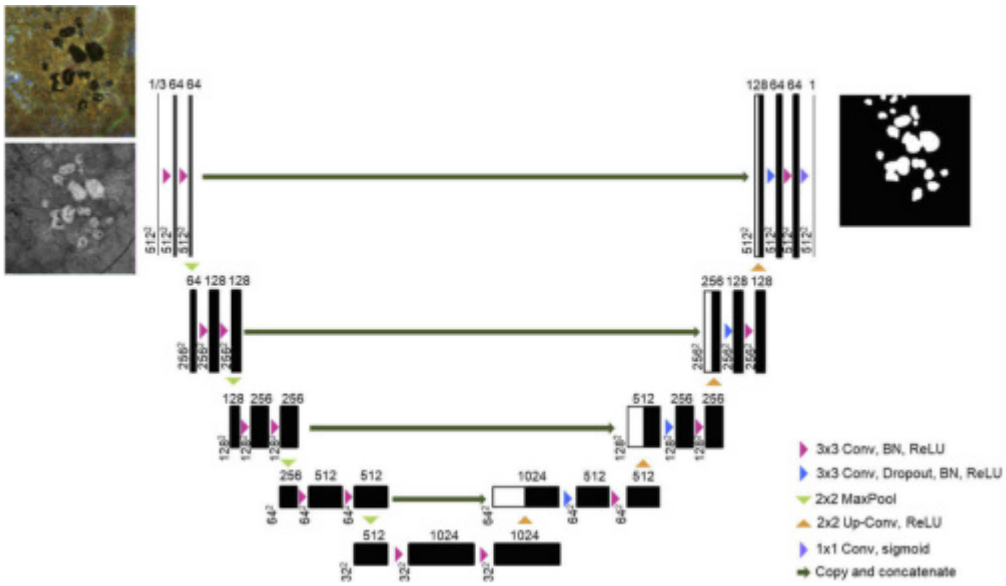

Figure 4.1.2. Model architecture and specifications used to perform geographic atrophy segmentation.

Evaluation metrics and statistical analysis

To evaluate the performance of trained models, DSC, area square-root difference (ASRD), the subject-wise sensitivity, and specificity were calculated on the testing set:

$$DSC = \frac{2TP}{2TP+FP+FN} \tag{4.1.3}$$

$$\text{Sensitivity} = \frac{TP}{TP+FN} \tag{4.1.4}$$

$$Specificity = \frac{TN}{TN+FP} \tag{4.1.5}$$

where TP denotes true positive, TN denotes true negative, FP denotes false positive, and FN denotes false negative. Note that TP, FP and FN in Eq. (4.1.3) represent pixel level information and TP, TN, FP, and FN in Eqs. (4.1.4) and (4.1.5) represent eye level information. A threshold of 0.5 was used to binarize the probability map from the model's prediction output. An image with any GA pixels is classified as having GA.

To further compare the identified GA regions, total area and square-root area measurements of GA were calculated for both ground truth and model outputs. A square-root transformation was applied to calculate the size and growth of GA since this strategy decreases the influence of baseline lesion size on the test-retest variability and on the growth of GA [153,204]. The paired t-test was used to compare model outputs using OAC composite images and OCT subRPE images. Pearson's linear correlation was used to compare the square-root area of the manual and automatic GA segmentations, and Bland Altman plots were used to analyze the agreement between the square-root area of the manual and automatic GA segmentations. P values of < 0.05 were considered to be statistically significant.

4.1.3 Results

In total, 80 eyes diagnosed with GA secondary to nonexudative AMD and 60 normal eyes with no history of ocular disease, normal vision, and no identified optic disc, retinal, or choroidal pathologies on examination were included in this study. All cases were randomly shuffled such that 51 GA eyes and 38 normal eyes were used for training, 13 GA eyes and 10 normal eyes were used for validation, and 16 GA eyes and 12 normal eyes were used for testing. In the training dataset, 22 out of these 51 eyes had three scans from three visits and these scans were added into the training set for data augmentation. Eyes in the validation and testing set only had one scan. Table 4.1.1 summarizes patient demographics in this study.

Table 4.1.1 Patient demographics.

		Training	Validation	Testing
Age (mean ± SD, (range),years)		63 ± 21 (23-91)	60 ± 22 (26-88)	64 ± 22 (27-93)
Gender	Female	62	14	14
	Male	27	9	14
Race	White	78	22	26
	Black	10	0	1
	Asian	1	1	1
AMD grading	N/A	38	10	12
	Advanced; AREDS 4	51	13	16
Number of eyes		89	23	28
Number of patients		70	20	25
Number of visits		3 visits for 22 eyes, 1 visit for 67 eyes	1 visit per eye	1 visit per eye

[a] Abbreviations: SD, standard deviation; AMD, age-related macular degeneration; AREDS, Age-Related Eye Disease Study.

Figure 4.1.3 demonstrates GA visualization with our proposed OAC approach. Panels A and I show examples of *en face* OCT subRPE images of a normal eye and an eye with GA, respectively. Panels B and J show manually labeled GA areas. Panels C-F (normal eye) and K-N (GA eye) show examples of our proposed composite OAC false color images, OAC elevation maps, OAC max images, and OAC sum images, respectively. Panels G and O show OCT B-scans and panels H and P show the corresponding OAC B-scans.

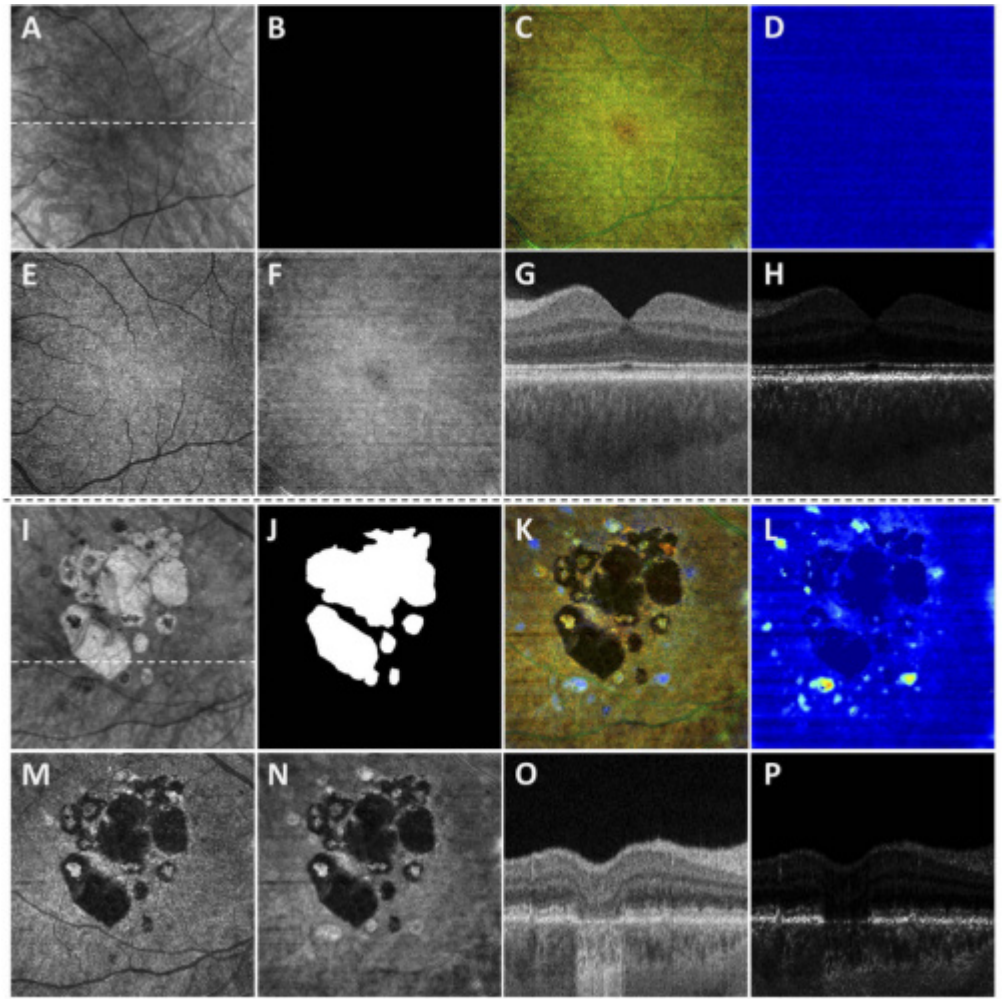

Figure 4.1.3. Geographic atrophy (GA) visualized using the optical attenuation coefficient (OAC) estimated from swept-source optical coherence tomography (SS-OCT).

Representative images are shown from a normal eye (A – H, 34 years old male) and a GA eye (I – P, 76 years old female), respectively. A, I: OCT subRPE images. B, J: ground truth of GA generated by graders. C, K: composite OAC false color images. D, L: OAC elevation maps. E, M: OAC max images. F, N: OAC sum images. G, O: OCT B-scans with its location represented by dashed lines in panels A and I. H, P: corresponding OAC B-scans with the same location of G and O. All images are from 6 × 6 mm SS-OCT scans. All B-scans were flattened based on BM segmentation.

In total, 2 separate models with the same architecture were trained using the same datasets but with different *en face* images as the input, namely, the composite OAC false color model and the OCT subRPE model. Both models had the same learning rate of 0.0003 and the same batch normalization momentum of 0.1 with the scale set as false. A dropout of 0.3 was used for the composite OAC model and a dropout of 0.5 was used for the OCT subRPE model. All hyper parameters were tuned on the validation set. Each

model was trained with 200 epochs and their specific sDSC for training, validation, and testing are given in Table 4.1.2.

Soft DICE	OAC false color	OCT subRPE
Training	0.948	0.951
Validation	0.931	0.922
Testing	0.944	0.897

Table 4.1.2. Training and testing results of proposed models.

A series of evaluation metrics were quantified on the testing cases for each trained model, and their specific values are tabulated in Table 4.1.3. For testing, the model outputs, GA probability maps (0-1), were binarized with a threshold of 0.5. DSC was calculated for each individual image and the mean and standard deviation (SD) were reported in Table 4.1.3 for each model. In the 16 GA eyes in the testing set, the composite OAC false color model significantly outperformed the OCT subRPE model ($p = 0.03$, paired t-test). Both models achieve 100% sensitivity and 100% specificity in identifying GA subjects from normal subjects.

	OAC false color	OCT subRPE
DSC (GA eyes)	0.940 ± 0.032	0.889 ± 0.056
Sensitivity	100%	100%
Specificity	100%	100%

Table 4.1.3. Evaluation metrics for all trained models.

Figures 4.1.4 - 4.1.7 show 4 cases with GA from the test set. In these figures, panel A shows the OCT subRPE image; panel B shows the GA predicted by the OCT subRPE model (magenta dotted lines) compared with the ground truth (cyan dashed lines); and panel C shows a representative OCT B-scan with its location at the dashed line in panel A. Panel D shows the composite OAC image; panel E shows GA predicted by the composite OAC model (magenta dotted lines) compared with the ground truth (cyan dashed lines); and panel F shows OAC B-scan with the same location as panel C. Solid white arrows indicate false negative GA segmentation and dashed arrows show the false positive GA segmentation.

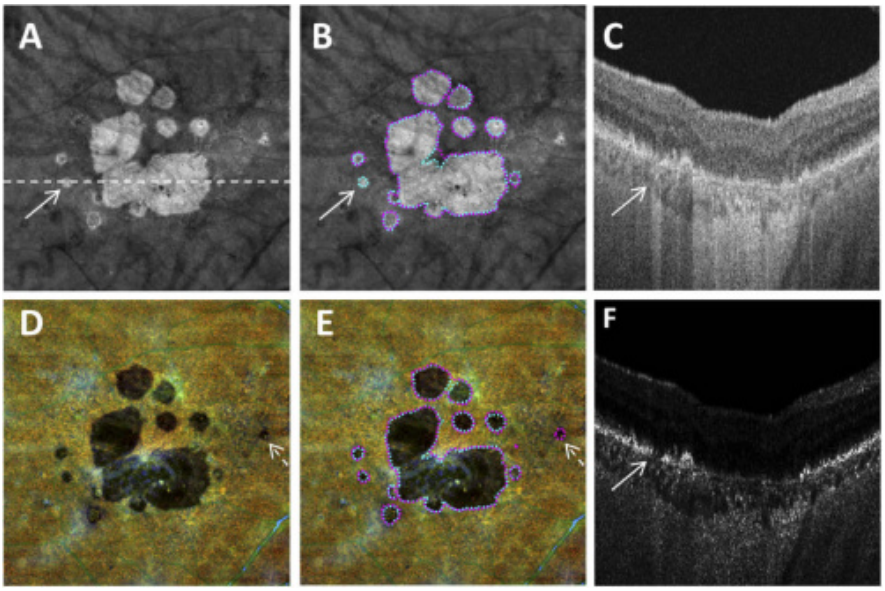

Figure 4.1.4. *En face* visualization of geographic atrophy (GA) predicted by trained models from a 92 years old male patient.

A: OCT subRPE image. B: GA predicted by the OCT subRPE model (magenta dotted lines) compared to the ground truth (cyan dashed lines). C: OCT B-scan with its location represented as dashed line in A. D: Composite Optical attenuation coefficient (OAC) image. E: GA predicted by the composite OAC model (magenta dotted lines) compared to the ground truth (cyan dashed lines). F: OAC B-scan with its location represented as dashed line in A. Solid arrows indicate false negative segmentation results and dashed arrows indicate false positive segmentation results.

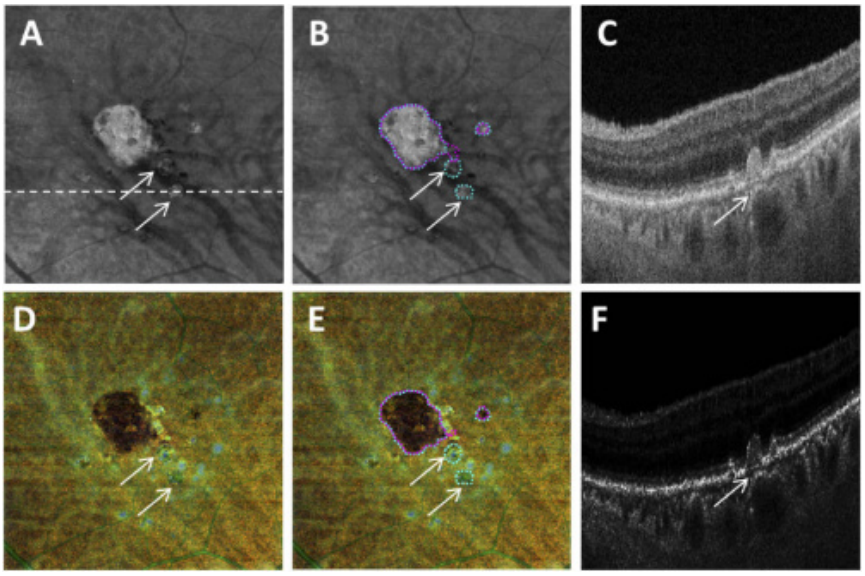

Figure 4.1.5. *En face* visualization of geographic atrophy (GA) predicted by trained models from a 79-year-old male patient.

A: OCT subRPE image. B: GA predicted by the OCT subRPE model (magenta dotted lines) compared to the ground truth (cyan dashed lines). C: OCT B-scan with its location represented as dashed line in A. D: Composite Optical attenuation coefficient (OAC) image. E: GA predicted by the composite OAC model (magenta dotted lines) compared to the ground truth (cyan dashed lines). F: OAC B-scan with its location represented as dashed line in A. Solid arrows indicate false negative segmentation results.

To further compare the quantification of GA segmentation generated by our models with the ground truth, the GA square-root area was calculated for all GA cases in the test set. Figure 4.1.6 shows the Bland-Altman plots and Pearson's correlation plots of both proposed models. GA square-root area segmented by both models showed significant correlation with ground truth ($R2 = 0.99$ for composite OAC model and $R2 = 0.92$ for OCT subRPE model, both $p < 0.0001$). Both model outputs also showed satisfactory agreement with the ground truth; the composite OAC model resulted in a smaller bias of 11 μm while the OCT subRPE model resulted in a larger bias of 117 μm, compared with the ground truth.

4.1.4 Discussions and conclusion

In this study, we introduced a novel strategy to visualize GA using OAC calculated from OCT datasets, and we demonstrated that the proposed composite OAC false color *en face* images could be effectively used to identify, segment, and quantify GA areas automatically with a deep learning model.

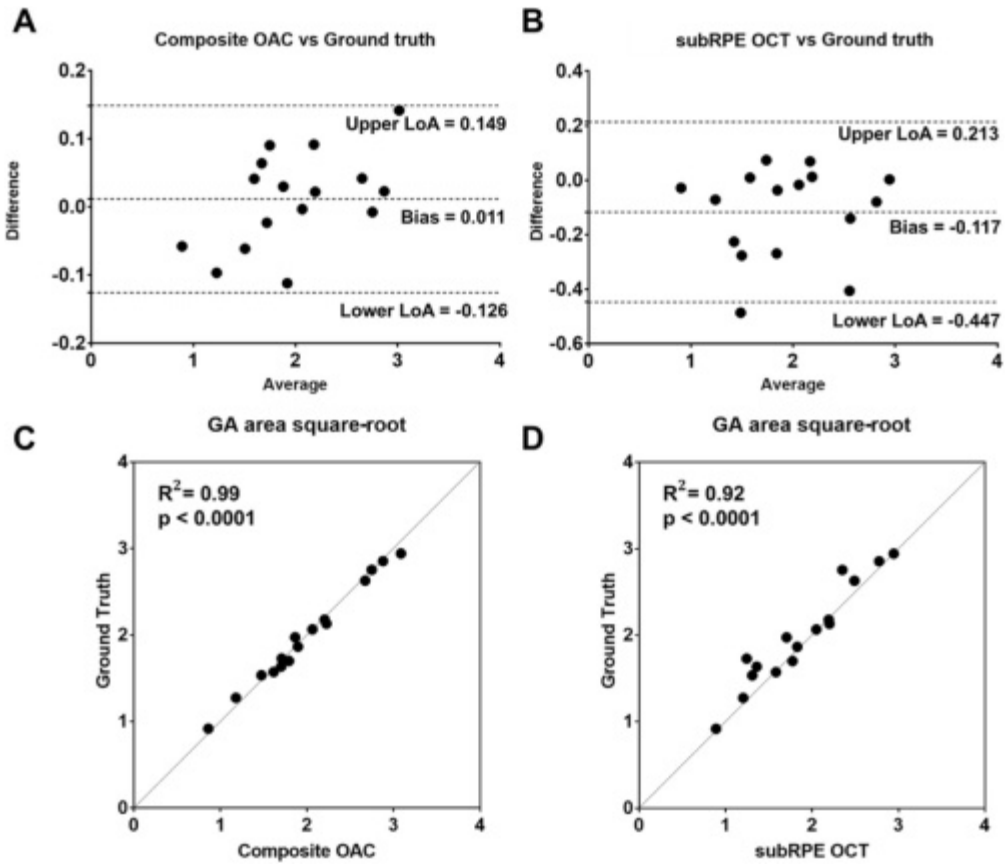

Figure 4.1.6. Quantitative comparison of geographic atrophy (GA) square-root area predicted by trained models with ground truth.

A: Bland-Altman plot of GA square-root area generated by the composite optical attenuation coefficient (OAC) model compared with ground truth. B: Bland-Altman plot of GA square-root area generated by the OCT sub-retinal pigment epithelium (subRPE) model compared with ground truth. C: Pearson's correlation plot of GA square-root area generated by the composite OAC model with ground truth. D: Pearson's correlation plot of GA square-root area generated by the OCT subRPE model with ground truth. All units of axes are in mm. LoA, limit of agreement.

According to Classification of Atrophy Meetings (CAM) consensus, the definition of GA or cRORA is defined by 3 inclusive OCT criteria: (1) region of hyperTD with at least 250 µm in its greatest linear dimension, (2) zone of attenuation or disruption of the RPE of at least 250 µm in its greatest linear dimension, and (3) evidence of overlying photoreceptor degeneration; and 1 exclusive criteria: the presence of scrolled RPE or other signs of an RPE tear [161]. This definition of GA or cRORA relies solely on average B-scans, but en face imaging of GA using the subRPE slab is a convenient alternative for the detection of GA using fundus autofluorescence and conventional OCT B-scans [164,190,204–206]. Our proposed OAC

approach is particularly suitable for GA identification because it allows en face views with direct three-dimensional information of RPE attenuation and disruption. OAC quantifies the tissues' ability to attenuate (absorb and scatter) light, meaning that it is particularly useful to identify high pigmentation (or the lack of) in retinal tissues. Using our custom slab and *en face* imaging strategy, we show that the composite OAC false color images provide a novel approach to visualizing the RPE with strong contrast. When RPE cells die and lose pigments, their OAC values are reduced as well, resulting in a dark appearance on the composite OAC images. This is very similar to the loss of lipofuscin causing a dark appearance on FAF images, but OAC is not specific to lipofuscin, nor melanin. In addition to the enhanced contrast for attenuated or disrupted RPE, our OAC approach also provides the same depth-resolved advantage as the traditional OCT approach. By incorporating three different *en face* images from the same slab in the composite OAC images, we provide depth-resolved information, namely the RPE elevation information on an *en face* view. This approach is also useful for identifying drusen or other forms of RPE elevation in AMD eyes [202].

We used the same deep learning model architecture and trained two models with different input images; the traditional OCT subRPE images that were widely used in previous studies [191,194,199] and the novel composite OAC images we introduced in this study. We purposely designed our study so as to illustrate the importance of image pre-processing for GA segmentation with deep learning. In our study, using the same model architecture, the same hyper-parameter tuning process, and the same patients' OCT scans, we demonstrated a significantly higher agreement with the ground truth by using composite OAC images than by using traditional OCT subRPE images in our testing set. For all 28 eyes in our testing sets, both models successfully identified eyes with GA from normal eyes. For the 16 eyes with GA in the testing sets, the composite OAC model achieved a mean DSC of 0.940 and a SD of 0.032, significantly higher than the OCT subRPE model with a mean DSC of 0.889 and a SD of 0.056 ($p = 0.03$, paired t-test), respectively. For GA square-root area measurements, the composite OAC model achieved a stronger correlation with the ground truth than the OCT subRPE model ($r = 0.995$ vs $r = 0.959$, $R^2 = 0.99$ vs $R^2 = 0.92$), as well as a smaller mean bias (11 μm vs 117 μm).

Previous studies have reported GA segmentation models with different input images resulting in different DSC segmentation accuracies. Using CFI as inputs, Feeny et al. reported a DSC of 0.68 ± 0.25 using a random forest algorithm [207] and Liefers et al. reported a DSC of 0.72 ± 0.26 with a deep learning network [208]. In comparison, models with FAF and SD-OCT images have resulted in higher DSC values. Hu et al. reported a DSC of 0.89 ± 0.07 using FAF inputs and a DSC of 0.87 ± 0.09 using SD-OCT inputs with a level set approach [209]. Wu et al. reported a DSC of 0.872 ± 0.066 using SD-OCT images as input with GAN synthesized FAF and a U-Net model for segmentation [199]. In our study, using a simple U-Net model and

SS-OCT data, we achieved a DSC of 0.889 ± 0.056 using subRPE images, similar to what were used in SD-OCT studies. Though different datasets were used in different studies and direct comparisons of testing DSC values are somewhat unfair, our SS-OCT subRPE model achieved a segmentation accuracy that was similar to these previous studies. However, the model using composite OAC images achieved a significantly higher segmentation accuracy (0.940 ± 0.032) compared with the model using OCT subRPE images. This is a fair comparison since the same volumetric SS-OCT datasets were used to generate the *en face* images for input in the models. It should also be noted that though our deep learning model structure is simpler compared to some of these previously published studies, [197–199] our segmentation accuracy in terms of DSC is similar to or superior to what were reported before, likely due to the use of denser and higher quality SS-OCT scans as well as the enhanced contrast of GA produced by using the OAC.

The criteria for defining GA or cRORA are evolving and this adds difficulty to the task of GA segmentation. In our study, we followed the criteria proposed by the CAM consensus meeting and defined regions of cRORA based on the attenuation/disruption of the RPE [199]. Figure 4.1.4 – 4.1.7 demonstrate some segmentation inaccuracies of our proposed model using solid arrows to represent false negative segmentation and dashed arrows to represent false positive segmentation. It should be noted that we did not apply a size threshold (250 microns in its greatest linear dimension) to our model outputs, therefore some false positive segmentations (Figure 4.1.4, dashed arrows) may represent incomplete RPE and outer retina atrophy (iRORA) instead of cRORA due to its size. Depending on specific applications, further developments and uses of our model could include size thresholding. There are several possible situations that may lead to possible false negative results. Figure 4.1.5 shows example of un-segmented cRORA that may not reach the 250 micron threshold in the horizontal dimension, yet the border of the lesion in a non-horizontal dimension may exceed 250 microns. As shown in B-scans (panels C and F), even though hyperTDs and attenuated/disrupted RPE are present, the RPE is still elevated and the hypertransmission or OAC defect can still be seen on both the composite OAC image and the subRPE OCT image. This raises the question of whether restricting the definition of cRORA to the horizontal dimension really makes sense since the progression of disease occurs in all dimensions. The advantage of *en face* imaging is that the full geometry of disease progression can be appreciated, not just what occurs in the horizontal dimension on the B-scan. In these situations, both models may be better at actually identifying the full extent of disease. Figure 4.1.6 shows an example of a false negative outcome where residual RPE was surrounded by cRORA. According to the manual grading guidelines, such regions were included in the cRORA outline, but both models struggled to correctly segment them as there is still residual RPE signal present. Figure 4.1.7 shows an example of a false negative outcome caused by choroidal vessel artifacts. The OCT subRPE model failed to identify these regions correctly, but the composite OAC model correctly labeled these regions as cRORA,

since the choroidal vessel artifacts are not as prominent on OAC images as they are on OCT subRPE images.

There are several limitations of our study. First, our approach is an estimation of the true OAC values and might not be an entirely accurate representation of the OAC. We selected this approach for its computation simplicity and its depth-resolved nature. It should also be noted that the assumption of complete signal attenuation within the imaging range is often violated within GA lesions, meaning that our study could underestimate the OAC values within the GA region. There are other OAC estimation approaches that could potentially be more accurate but would not meet the purpose here to develop an automated segmentation of GA [210–212]. Second, we used a well-known and simple U-Net model structure and our technical contribution in terms of model architecture is very limited. We made this choice to emphasize the added value of the proposed composite OAC images and to demonstrate that innovation in data pre-processing could be equally important, if not more important than model architecture innovation in medical imaging. Third, we had a limited dataset to work with and only 80 eyes with GA were included in our study, there is also a significant difference in age among our eyes with GA and normal eyes. With the limited number of patients in our study, we were not able to only include one eye per patient and this could potentially introduce bias in our study as well. Future developments and validation using a larger dataset are warranted. Lastly, it should be noted that though our study was based on SS-OCT data, it remains to be seen whether our proposed method can equally be applied to SD-OCT data. Our study has only included OCT scans from PLEX Elite 9000, there could potentially be variation in converting OCT signal back to linear scale among different OCT instruments and future studies are warranted.

In summary, we proposed a novel strategy to visualize and quantify GA using composite OAC false color *en face* images generated from SS-OCT datasets, and we demonstrated that these OAC images could be used to identify, segment, and quantify GA automatically and accurately with a simple deep learning U-Net model.

Chapter 4.2 Depth-resolved visualization and automated quantification of hyperreflective foci on OCT scans using optical attenuation coefficients

4.2.1 Introduction

Hyperreflective foci (HRF) detected by optical coherence tomography (OCT) imaging of eyes with age-related macular degeneration (AMD) result from the aggregation and migration of cells from the retinal pigment epithelium (RPE) into the retina [63]. These HRF appear as foci of hyperpigmentation on color fundus imaging (CFI) and fundus biomicroscopy, and when associated with medium-sized drusen, these pigmentary abnormalities are sufficient to categorize an eye as having intermediate AMD (iAMD) [46,213]. Moreover, these HRF are recognized as a risk factor for disease progression from iAMD to late AMD [214–219]. A recent OCT study found that focal pigment abnormalities on CFI not only correspond to intraretinal HRF, but also to HRF along the RPE [139]. Due to the high reflectivity of HRF in the retina and along the RPE, these lesions are associated with decreased light penetration into the choroid and cause OCT choroidal hypo-transmission defects (hypoTDs), which appear as dark foci on *en face* sub-RPE choroidal slabs [139]. In light of these observations, we will use the terms foci of hyperpigmentation and pigment burden to refer to the HRF on OCT.

While the presence of HRF has been recognized as a risk factor for disease progression in AMD, there have been limited attempts to quantify these lesions using OCT imaging [139,217]. In these previous reports [217,220], retinal OCT B-scans and *en face* images were used to identify HRF in the retina, but foci of hyperreflectivity along or in close proximity to the RPE were not included. This oversight significantly limits the utility of these approaches to quantify the total burden of hyperpigmentation, which, we now know, includes foci of intraretinal hyperpigmentation and hyper-pigmentation along the RPE [139]. Currently, we are unaware of any automated algorithms that can visualize and quantify this total retinal pigment burden in the macula.

In order to develop a rapid and reliable algorithm that could quantify the total pigment burden in the macula, we developed a novel approach for identifying both the HRF in the retina and the foci of hyperpigmentation along the RPE. These lesions were localized and quantified by identifying the foci of hyperpigmentation within OCT slabs that included only the retina (above RPE) and foci of hyperpigmentation within slabs that included only the RPE complex, while the total pigment burden was quantified using a slab that included both the retina and RPE. Reference manual total pigment burden measurements were obtained by combining manual outlines of HRF within the B-scans and the total manual outlines of hypoTDs visualized on *en face* sub-RPE slabs that used segmentation boundaries extending from 64 to 400 μm below Bruch's membrane (BM).

Previously, we pioneered the use of these sub-RPE slabs to visualize and quantify areas of choroidal hypertransmission defects (hyperTDs) associated with the formation and growth of geographic atrophy (GA) [120,139,154,166,171]. While using these slabs to characterize GA, we came to appreciate that the same sub-RPE *en face* slabs could be used to identify areas of choroidal hypoTDs in iAMD, which appeared as dark regions on the *en face* OCT images [11,139]. While hypoTDs are often associated with hyperpigmentation, there are other pathological features such as calcified drusen, vitelliform material, and large retinal pigment epithelial detachments (PEDs) that may also lead to choroidal hypoTDs in eyes with iAMD [11,221,222]. These non-pigmentary lesions can be easily identified and excluded from the manual annotations by reviewing the corresponding B-scan through a particular region [11,139]. This strategy of using OCT *en face* imaging in conjunction with B-scans is currently used clinically to identify and localize the pathologies associated with both choroidal hyperTDs and hypoTDs. An automated algorithm for the segmentation of these pigmentary lesions would reduce the labor required to manually identify the pathologies associated with hypoTDs.

In this report, we utilize a strategy that converts OCT images into images that are contrasted by optical attenuation coefficients (OAC), a technique which has been shown to be useful in the automated segmentation and evaluation of GA [57,223], as well as choroidal thickness and choroidal vascularity [223,224]. OAC is defined in terms of the loss of OCT signal with depth caused by tissue absorption and scattering [225,226]. It is one of the physical parameters that measures the optical properties of a tissue [227] and can be directly extracted from OCT scans. OAC values enhance the contrast between high and low scattering regions in comparison to the standard OCT intensity and can be useful in localizing and quantifying the total pigment burden in the macula, since the HRF are characterized by strong optical scattering properties. Herewith, we describe a strategy using the OAC information from the original OCT images to develop an automated algorithm to visualize, localize, and quantify HRF in the retina and along the RPE by using the OACs within specific slabs obtained from the entire OCT scanning volume.

4.2.2. Method

Imaging acquisition

Patients at the Bascom Palmer Eye institute were enrolled in a prospective SS-OCT imaging study approved by the institutional review board of the University of Miami, Miller School of Medicine. Informed consent was obtained from each subject before imaging. The study was performed in accordance with the tenets of the Declaration of Helsinki and complied with the Health Insurance Portability and Accountability Act of 1996. For each enrolled patient, they underwent SS-OCT imaging using a 6×6 mm macular scan pattern (PLEX Elite 9000; Carl Zeiss Meditec, Inc, Dublin, CA, USA). The SS-OCT instrument has a scanning rate of 100,000 A-scans per second and a swept source laser with a central wavelength of 1,050 nm. Each 6×6 mm scan consisted of 500 B-scans, repeated twice at each B-scan location, and each B-scan consisted

of 500 A-scans. Scans with a signal strength less than 7 or with obvious motion artifacts were excluded. Scans were then retrospectively reviewed for the presence of HRF consistent with increased pigmentary deposits within the retina and along the RPE.

OAC calculation from OCT scan

Multiple models and methods have been developed to evaluate OAC from OCT scans [227,227–230]. In this work, SS-OCT scans were converted into OAC maps using the method described by Vermeer et al [201]:

$$\mu_i = \frac{A_i}{2\Delta \sum_{i+1}^{\infty} A_i} \tag{4.2.1}$$

where A is the OCT signal intensity in linear space and i denotes the pixel's position on A-Scan. Δ is the pixel size, and μ is the OAC which has a unit of mm^{-1}. Regions of HRF have higher OACs due to greater light attenuation than the surrounding tissue. Representative OCT B-scans and corresponding OAC images are shown in Figure 4.2.1, where the highly scattering RPE and migrated pigment are more strongly contrasted compared to the original OCT B-scans.

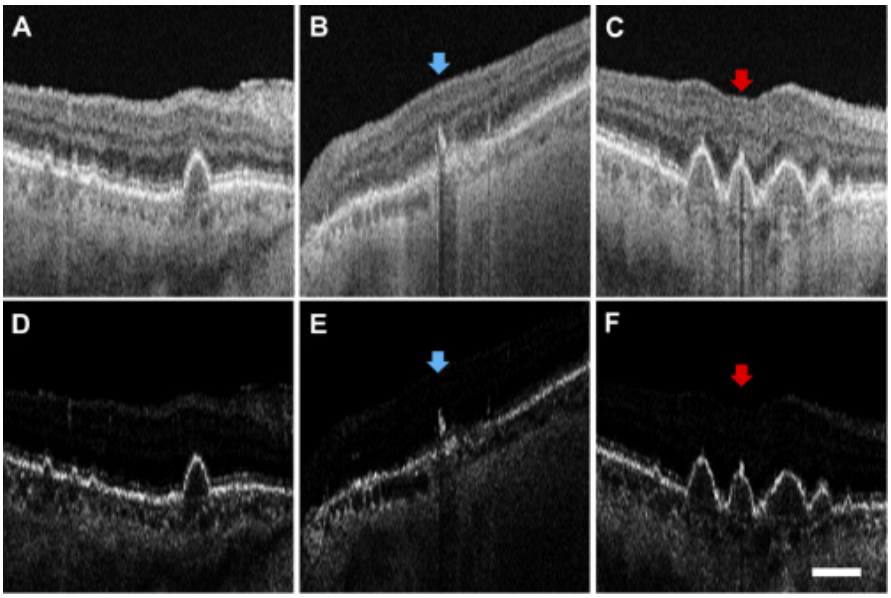

Figure 4.2.1. Representative OCT B-scans of eyes with drusen, intra-retinal pigment migration and hyperreflective foci along the retina pigment epithelium.

OCT B-scans with (A) drusen, (B) intra-retinal pigment migration (blue arrow) and (C) hyperreflective foci (HRF) along the retina pigment epithelium (RPE, red arrow), respectively. Corresponding optical attenuation coefficient (OAC) B-scans with (D) drusen, (E) intra-retinal pigment migration (blue arrow) and (F) HRF along the RPE (red arrow). Scale bar: 1 mm.

Visualization of HRF in 3-dimensional OAC volume

The distinct contrast of HRF in the OAC transformed OCT scans facilitates their automatic visualization and quantification. To do so, the segmentations of inner limiting membrane (ILM), nerve fiber layer (NFL), RPE and Bruch's membrane (BM) are required. While there are numerous strategies developed to achieve the segmentations including machine learning algorithms [231–239], in this work, the segmentations of ILM, NFL, RPE and BM were obtained using the manufacturer's automated software from OCT scan (Figure 4.2.2 (A)). The OAC data of the entire scan was then flattened at the position of BM for each B-scan (Figure 4.2.2 (C)). The 99.9 percentile of the intensities of all the OAC signals in the slab between ILM and NFL was set as the threshold for the background. Any signal in the OAC dataset with intensity smaller than the threshold was set to zero. Three channels were used to color code the information to help facilitate the visualization of the location of the HRF within the retina: (1) A mask of the slab from ILM to 40 μm above RPE was generated to identify intra-retinal HRF. The OAC values within this masked region were color-coded from black to blue, so that pigment migration is highlighted in blue (Figure 4.2.2 (D) (E)), (2) A mask of the slab from 40 μm above RPE to 10 μm below RPE was generated to identify HRF along the RPE. The OAC values within the masked region were color-coded from black to red, so that pigment deposits were highlighted with a red color (Figure 4.2.2 (F) (G)). (3) A slab below RPE with a thickness of 5 pixels (10 μm) is generated to demonstrate the RPE elevation in the region. The pixels in each A-scan were assigned as the distance from the RPE to BM at the location and color coded from grey to white, in which the regions with drusen were highlighted in white (Figure 4.2.2 (H) (I)). All the parameters were set empirically to best demonstrate the HRF and their surrounding tissues.

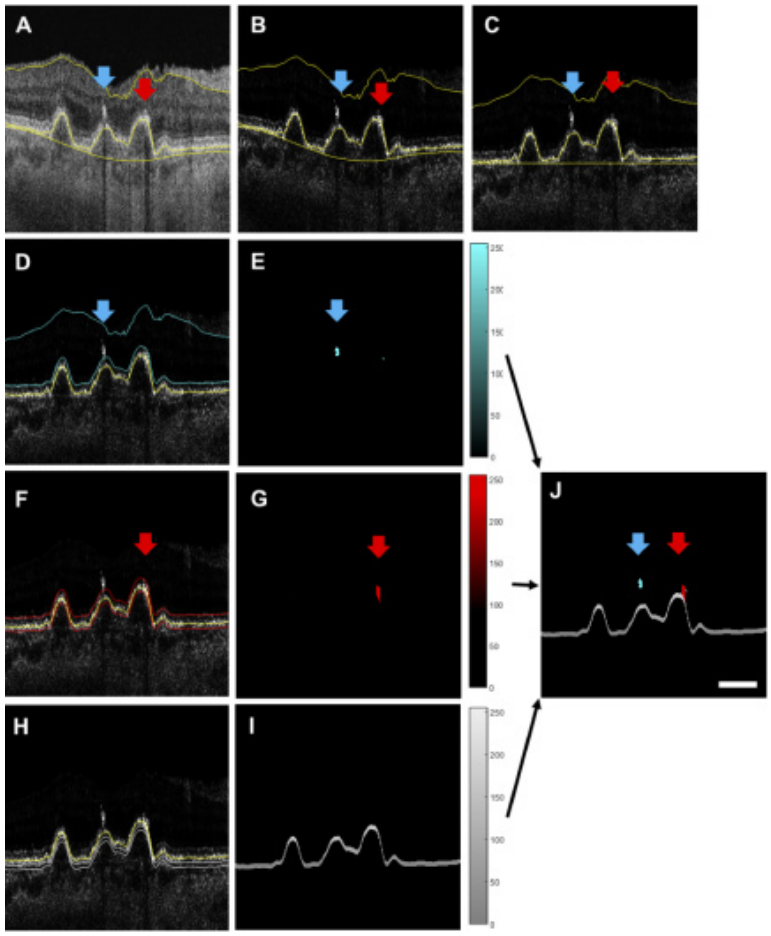

Figure 4.2.2. Color-coded visualization of hyperreflective foci (HRF) using optical attenuation coefficients (OACs).

(A) OCT B-scan overlaid with automated segmentations of the internal limiting membrane (ILM), retinal pigment epithelium (RPE) and BM (Bruch's membrane, yellow lines) from the manufacturer's software. (B) OACs of the corresponding B-scan with overlaid segmentations of ILM, RPE and BM. (C) Flattened OAC B-scan based on BM with segmentations of ILM, RPE and BM. (D, E) A mask is generated for intra-retinal region between ILM to 40 µm above RPE illustrated as blue lines in D. RPE segmentation is illustrated as yellow lines. OAC signals inside the masked region are color-coded from black to blue, where intra-retinal pigment migration is highlighted in blue with a blue arrow (E). (F, G) A mask is generated for the RPE-involved region from 40 µm above RPE to 10 µm below RPE illustrated as red lines in F. OAC signals inside the masked region are color-coded from black to red, where increased pigmentation along RPE is highlighted in red with a red arrow (G). (H, I) A mask is generated as a 10 µm thick slab from 10 to 20 µm below RPE illustrated as white lines in H. RPE elevation is color-coded from grey to white, where regions with drusen are highlighted in white (I). (J) Combined images showing HRF in the retina (blue) and along RPE (red) with elevation information (greyscale). Blue arrow: HRF in the retina; red arrow: HRF along the RPE. Scale bar: 1 mm.

Quantification of HRF from en face images

The intra-retinal HRF from each OCT B-scan and the areas with choroidal hypotransmission defects on OCT sub-RPE slabs were manually outlined by two graders (RL and JL). The grading on B-scans were firstly projected to an *en face* binarized image by marking all the pixels with the corresponding labeled A-line positions to 1 and then combined with the grading on sub-RPE images to generate the *en face* manual labels of the total pigment burden. The grading on B-scans is necessary because not all the intra-retinal HRF have hypo-transmission defects on choroid, therefore, these pigments might be missed if only sub-RPE images are graded. For automated quantification of the total retinal pigment burden using OAC imaging, an *en face* strategy was used. Similar to other *en face* strategies previously used for GA segmentation and area measurement [57,153], an *en face* sum projection of OAC signals in a slab from the ILM to BM was generated. To segment the total pigment burden, we applied an adaptive thresholding strategy with a local window of 700 μm in diameter. A MatLab built-in function was applied to calculate the locally adaptive threshold for each pixel using the local mean intensity around the neighborhood of the pixel. The area of the total pigment burden was defined within a 5 mm circle centered on the fovea, and this area was used to compare the measurements obtained from manual segmentation and the automated algorithm.

Statistical analysis

Pearson correlation and Bland-Altman analysis were utilized to compare the area measurements of the total pigment burden from the manual segmentations and the automated algorithm. Statistical analysis was carried out using MATLAB R2018b and IBM SPSS V25 (Armonk, NY, USA), and plots were generated using GraphPad Prism (GraphPad Software, San Diego, CA, USA).

4.2.3 Results

A total of 49 eyes with nonexudative AMD from 42 patients (74.6 ± 6.9 years, 61.2% women) with intra-retinal HRF and increased reflectivity along the RPE were recruited. In these eyes hyper-reflective lesions were visualized using the automated algorithm developed in this study, intra-retinal HRF were distinguished from hyper-reflective lesions along the RPE, and the position of these HRF were localized relative to the position of drusen.

The total pigment burden area measurements were automatically generated from the *en face* OAC images and validated against manual segmentations. Out of the 49 recruited eyes, the hyper-reflective lesions of a test set of 24 eyes from 20 patients (74.2 ± 6.4 years, 70.8%women) were manually segmented by identifying intra-retinal lesions on OCT B-scans and choroidal hypo-transmission defects on OCT sub-RPE slabs extending 64 to 400 μm below BM. A consensus was reached between the two graders (RL and JL) on all the 24 scans. Note that this set of scans with manual annotations was not used to develop the OAC

algorithm or in optimizing the thresholding parameters. A significant correlation was found in the area measurements of the total pigment burden between the automated and manual segmentations ($P < 0.001$, Figure 4.2.3 (A)). Bland-Altman analysis showed that there was an averaged bias of 0.032 mm^2 between manual and automated segmentations (Figure 4.2.3 (B)). The areas of pigment segmented from the OAC algorithm tended to be smaller than the manually segmented pigment from OCT scans. Overall, the automated algorithm had a good agreement with human graders.

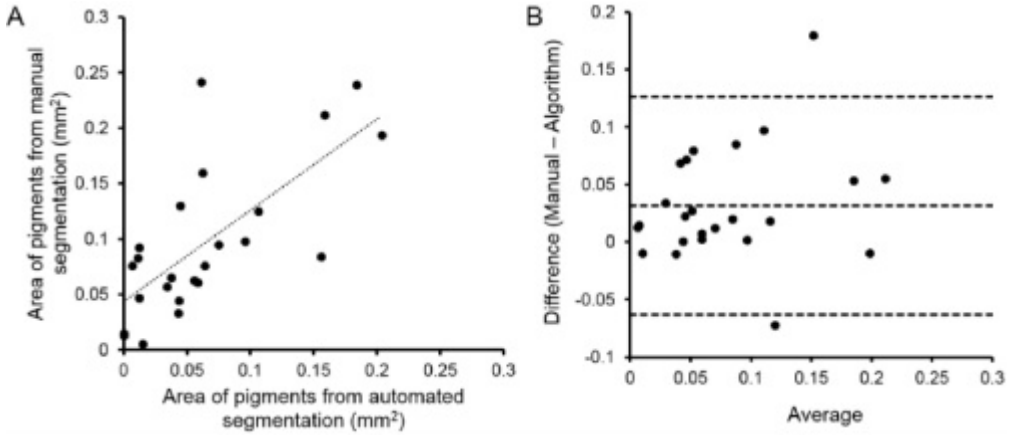

Figure 4.2.3. Comparison of the area of total pigment burden measured manually and automatically.

(A) Area of total pigment burden measured using the OAC algorithm vs. the area of total pigment measured manually. (B) Bland-Altman analysis of the data shown in A.

Figures 4.2.4 and 4.2.5 show two representative eyes with HRF along the RPE (Figure 4.2.4) and within the retina (Figure 4.2.5). There was good agreement between the segmentations from the automated algorithm and those from the human graders (Figure 4.2.4 (D) (H) and 4.2.5 (D) (H)). The OAC B-scans show enhanced contrast of the hyperpigmentation that appear slightly smaller compared with the original OCT B-scans (Figure 4.2.4 (B) (F) and 4.2.5 (B) (F)), this might explain why the segmented regions from OAC images are generally smaller than the manually segmented regions from the OCT images. We also observed improved contrast of pigmentary lesions on the *en face* images using OACs (Figure 4.2.4 (A) (E) and 4.2.5 (A) (E)), and this might explain why some small lesions were picked up by the algorithm which were not marked by the graders.

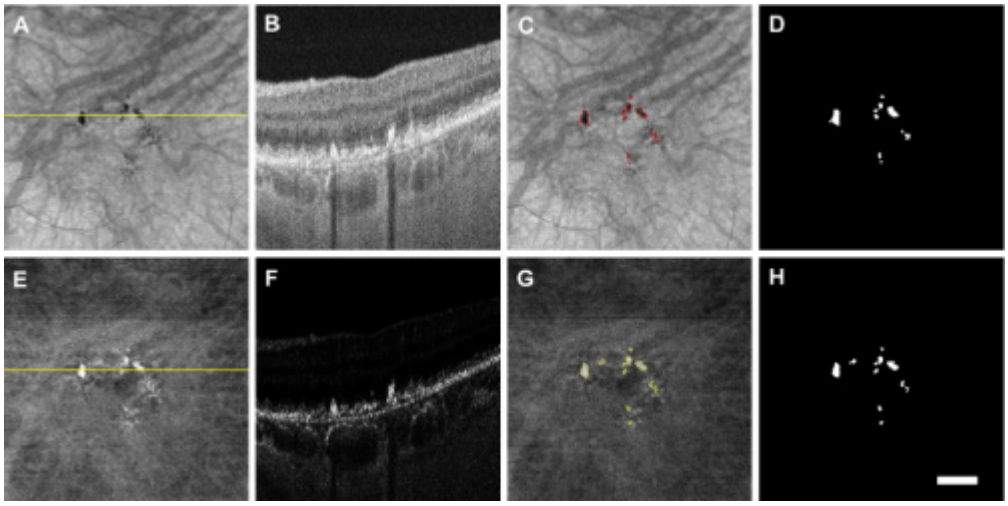

Figure 4.2.4. An example of manual and automated segmentations of the total pigment burden in an eye with hyper-reflective foci along the RPE.

(A) En face OCT image of the sub-RPE slab. (B) Representative OCT B-scan (location indicated by yellow line). (C) Manual segmentation (red) of total pigment burden overlaid on the slab from beneath the retinal pigment epithelium (sub-RPE slab). The manual segmentation was generated combining the outlines from sub-RPE OCT image and B-scans. (D) Binarized total pigment burden from the manual segmentation. (E) En face OAC images of a slab from the ILM to BM. (F) Representative OAC B-scan (location indicated by yellow line). (G) Automated segmentation of the total pigment burden (yellow) overlaid on the OAC image. (H) Binarized total pigment burden from automated algorithm. Scale bar: 1 mm.

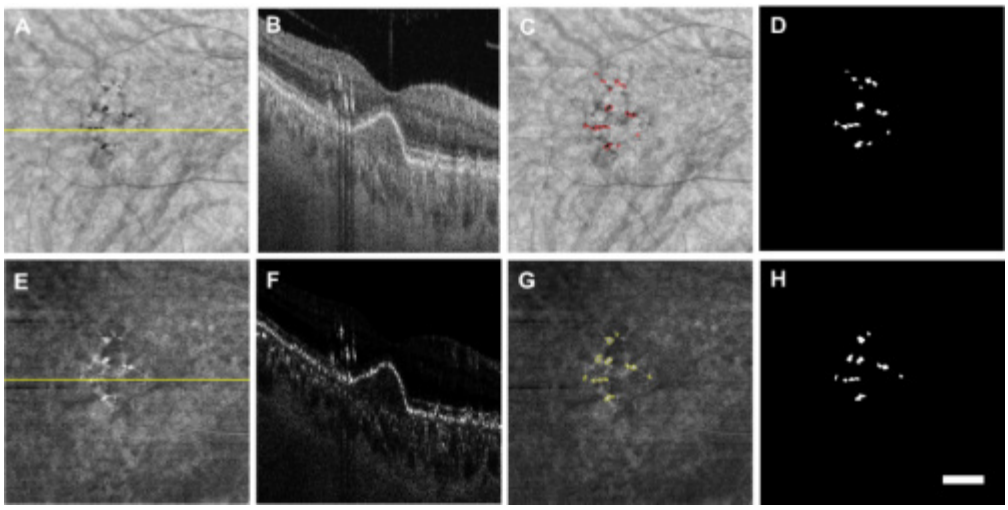

Figure 4.2.5. An example of manual and automated segmentations of the total pigment burden in an eye with intra-retinal hyper-reflective foci.

(A) En face OCT image of the sub-RPE slab. (B) Representative OCT B-scan (location indicated by yellow lines). (C) Manual segmentation (red) of total pigment burden overlaid on the slab from beneath the retinal pigment epithelium (sub-RPE slab). The manual segmentation was generated combining the outlines from sub-RPE OCT image and B-scans. (D) Binarized total pigment burden from the manual segmentation. (E) En face OAC images of a slab from the ILM to BM. (F) Representative OAC B-scan (location indicated by yellow lines). (G) Automated segmentation of the total pigment burden (yellow) overlaid on the OAC image. (H) Binarized total pigment burden from automated algorithm. Scale bar: 1 mm.

4.2.4 Discussion

Both the OAC B-scans and *en face* maps have demonstrated their importance in complementing traditional OCT images so that the physical properties of tissues can be enhanced and the more prominent features can be used to more easily develop automated algorithms [200,227]. Previously, OACs have been applied to improve the automated segmentation of GA and the choroid [200,227]. For the purpose of visualizing and automatically quantifying HRF, we sought to use OACs to identify regions where the light attenuation is the greatest at different depths between the ILM and just beneath the RPE. This strategy provided us with depth-resolved information and allowed us to distinguish intraretinal HRF from foci of increased pigmentation along the RPE since both appear as hyperpigmentation on color fundus imaging and as hypotransmission defects on sub-RPE OCT slabs [139]. Furthermore, since the OAC is calculated as a relative ratio of attenuation along the light path, the variance in laser energy and signal strength between scans would have a minimal effect on the measurements [226,227].

There have been previous attempts to develop automated algorithms to segment the HRF in the retina from OCT B-scans [220,240–242]. One group developed a complicated algorithm combining regions of interest generated by using morphological reconstruction, and the HRF were estimated using a component tree method to quantify the HRF from B-scans on spectral domain OCT (SD-OCT) [241]. However, the noise from retinal vessels and disrupted layers made the automated segmentation extremely challenging. In addition, several deep convolutional neural networks have been developed to segment the HRF in the retina from OCT B-scans [220,240,242]. The major limitation of these deep learning methods is the laborious manual annotations on cross-sectional images, making the performance of the model highly dependent on the small dataset in the study. So far, no automated algorithms are available in the clinical settings that can satisfactorily visualize and quantify the intraretinal HRF and the increased pigmentation along the RPE, to provide an assessment of the total retinal pigment burden.

The ability to provide depth-resolved visualization of HRF should be useful in distinguishing intraretinal pigment migration and hyperpigmentation along the RPE to determine if either or both serve as risk factors

for disease progression and to provide a convenient risk-assessment for disease progression in eyes with iAMD. Of note, it has been reported that intra-retinal RPE migration mainly occurred above areas of drusen (73.3% of eyes) [243]. As demonstrated in Figure 4.2.4, our proposed technique provided a visual representation of the entire scanned volume resulting in the opportunity to directly identify and quantitate where the hyperpigmentation is located and distributed within the macula. The proposed method using OACs to evaluate reflectivity along RPE should be useful to distinguish the non-pigmentary lesions such as calcified drusen, vitelliform material, and large retinal PEDs in eyes with iAMD because such lesions may also lead to choroidal hypoTDs in OCT scans but not necessarily high OACs. It is worth exploring whether OACs can work as a biomarker to separate pigmentary lesions from non-pigmentary lesions in the future study.

The quantification of HRF from *en face* OAC images has several advantages. It is consistent with several other clinical practices using *en face* images in AMD studies such as drusen mapping, the identification and segmentation of GA, and the analysis of choriocapillaris flow deficits. By using only one *en face* image for each scan, it is faster to compute compared with previous methods using hundreds of OCT B-scans for a single volumetric scan [220,240–242]. We validated our strategy by showing that the measurements of total pigment burden using OACs were highly correlated with those from manual segmentations. While the results illustrated the differences between automated and manual segmentations in some complicated cases, these differences were mainly the results of how the foci of pigmentation appear on the OAC images versus traditional OCT image, with the OAC foci appearing slightly smaller. This can be further improved by optimizing the parameters using a larger and more various training dataset and by considering to combine automated strategies on both OAC and OCT images. Thus, by using the OAC strategy and an automated thresholding method, we were able to largely eliminate the laborious measurement of areas with increased pigmentation on OCT B-scans and areas of hypotransmission defects on sub-RPE *en face* OCT images.

There are several limitations in this study. First, the current work only validated the quantification of total pigment burden from *en face* OAC images. It will be interesting to explore if the technique can further provide quantification of HRF in the retina and along the RPE separately. Previous studies have reported using OCT B-scans that the HRF would most frequently migrate from the RPE into the outer nuclear layer (66.7% of eyes) and less frequently into more anterior retinal layers [244]. With the *en face* OAC images of selected slabs, it will be possible to easily study the dynamics of pigment migration over time without the tedious review on OCT B-scans at numerous visits. In addition, while the proposed method focusses on the HRF along and above the RPE since these lesions appear to be associated with the greatest risk of disease progression in AMD, it should also be possible to detect HRF in the choroid as previously reported from OCT B-scans [244]. Another limitation is that the scanning protocol used in this study was limited to 6 × 6

mm macular scans of SS-OCT only. Based on the properties of OACs, it should be possible to apply the same technique to other scanning protocols with different fields-of-view, as well as other OCT imaging modalities such as SD-OCT. Lastly, a limited number of scans have been tested and used for validation. Further testing with a larger dataset of eyes that contain various pathologies is warranted to provide additional validation of the technique and demonstrate its potential broader applications in clinical settings.

4.2.5 Conclusion

Overall, an automated algorithm based on OACs was able to visualize, localize, and quantify areas of increased pigmentation in the retina and along the RPE, and the automated *en face* measurements of the total pigment burden were successfully validated against manual measurements. This algorithm should be useful for assessing the overall risk of disease progression in eyes with AMD, monitoring disease progression, and studying the impact of therapies in eyes with AMDs.

Chapter 5. Summary and feature work

This thesis explores the development of innovative algorithms for enhancing the clinical assessment of ocular diseases using Optical Coherence Tomography (OCT) and Optical Coherence Tomography Angiography (OCTA). The research focuses on improving image quality, automating disease biomarker detection, and enhancing clinical applicability.

To achieve so, Chapter 2 presents advanced image processing algorithms to enhance OCT and OCTA image quality. The chapter details a three-dimensional registration algorithm for speckle reduction and visualization, as well as methods for correcting distortions in widefield montage images. These techniques significantly improve the signal-to-noise ratio and contrast of OCTA images, facilitating better visualization and quantification of ocular structures.

Chapter 3 focuses on using OCT to understand and quantify biomarkers of Age-related Macular Degeneration (AMD). It distinguishes between different types of drusen, explores their interaction with the choriocapillaris, and analyzes the grading exercise of macular atrophy. This chapter demonstrates how OCT can accurately identify and monitor AMD biomarkers.

Chapter 4 introduces automated detection techniques for AMD biomarkers using deep learning models integrated with OCT and OCTA imaging. It discusses the development of algorithms for automatic segmentation of geographic atrophy and quantification of hyperreflective foci, enhancing the clinical utility of OCT and OCTA in diagnosing and monitoring AMD.

Future research will focus on further refining the proposed algorithms to enhance their accuracy, speed, and robustness, potentially by implementing them on GPU platforms to reduce processing times. Potential clinical trials will be conducted to validate the effectiveness of these algorithms in real-world clinical settings, helping to fine-tune the algorithms based on clinical feedback and ensuring their reliability and applicability. In addition, the development of algorithms compatible with different OCT systems will facilitate widespread adoption, requiring the creation of standardized protocols that can be easily integrated into different clinical workflows. The application of these algorithms will be extended beyond ophthalmology to other medical fields such as dermatology, cardiology, dentistry, and oncology, requiring the adaptation of algorithms to analyze OCT images of different tissue types. Improving the deep learning models by incorporating more diverse and extensive training datasets will enhance their ability to accurately detect and segment various ocular and systemic disease biomarkers. Finally, the development of real-time

processing capabilities to provide immediate feedback during OCT imaging sessions will significantly improve the efficiency of clinical assessments and enable timely decision making.

By addressing these areas, OCT and OCTA can achieve greater diagnostic accuracy and efficiency, leading to better patient outcomes and significant improvements in medical imaging practices.

List of Journal Publications

A portion of this dissertation has been featured in the selected journal papers listed below

1. Cheng Y, Chu Z, Wang RK. Robust three-dimensional registration on optical coherence tomography angiography for speckle reduction and visualization. Quantitative Imaging in Medicine and Surgery. 2021 Mar;11(3):879.
2. Cheng Y et al. Calcified drusen prevent the detection of the underlying choriocapillaris using swept-source optical coherence tomography angiography, IOVS 2024 (Accepted)
3. Cheng Y et al. Comparison between OCT B-scan and En Face Imaging for the Diagnosis of Early Macular Atrophy in Age-Related Macular Degeneration, (Under review)
4. Mehta N, Cheng Y, Alibhai AY, Duker JS, Wang RK, Waheed NK. Optical coherence tomography angiography distortion correction in widefield montage images. Quantitative Imaging in Medicine and Surgery. 2021 Mar;11(3):928.
5. Rosenfeld PJ, Cheng Y, Shen M, Gregori G, Wang RK. Unleashing the power of optical attenuation coefficients to facilitate segmentation strategies in OCT imaging of age-related macular degeneration: perspective. Biomedical optics express. 2023 Sep 1;14(9):4947-63.
6. Chu Z, Cheng Y, Zhang Q, Zhou H, Dai Y, Shi Y, Gregori G, Rosenfeld PJ, Wang RK. Quantification of choriocapillaris with phansalkar local thresholding: pitfalls to avoid. American journal of ophthalmology. 2020 May 1;213:161-76.
7. Cheng Y, Guo L, Pan C, Lu T, Hong T, Ding Z, Li P. Statistical analysis of motion contrast in optical coherence tomography angiography. Journal of biomedical optics. 2015 Nov 1;20(11):116004-.
8. Lu J, Cheng Y, Hiya FE, Shen M, Herrera G, Zhang Q, Gregori G, Rosenfeld PJ, Wang RK. Deep-learning-based automated measurement of outer retinal layer thickness for use in the assessment of age-related macular degeneration, applicable to both swept-source and spectral-domain OCT imaging. Biomedical Optics Express. 2024 Jan 1;15(1):413-27.
9. Lu J, Cheng Y, Li J, Liu Z, Shen M, Zhang Q, Liu J, Herrera G, Hiya FE, Morin R, Joseph J. Automated segmentation and quantification of calcified drusen in 3D swept source OCT imaging. Biomedical Optics Express. 2023 Mar 1;14(3):1292-306.
10. Li J, Wu CY, Shen M, Bynoe L, Nezgoda J, Liu J, Cheng Y, Sporysheva A, Albini T, Wang RK, Gregori G. Longitudinal quantification of choriocapillaris flow deficits in persistent placoid maculopathy: a case report. BMC ophthalmology. 2023 Dec;23(1):1-5
11. Shen M, Li J, Shi Y, Zhang Q, Liu Z, Zhou H, Lu J, Cheng Y, Chu Z, Zhou X, Liu J. Decreased Central Macular Choriocapillaris Perfusion Correlates With Increased Low Luminance Visual Acuity Deficits. American journal of ophthalmology. 2023 Sep 1;253:1-1.
12. Li J, Shen M, Cheng Y, Zhang Q, Liu J, De Sisternes L, Lewis WH, Wang RK, Gregori G, Rosenfeld PJ. The Impact of Cataracts on the Measurement of Macular Choriocapillaris Flow Deficits Using Swept-Source OCT Angiography. Translational Vision Science & Technology. 2023 Jun 1;12(6):7-.
13. Li J, Liu Z, Lu J, Shen M, Cheng Y, Siddiqui N, Zhou H, Zhang Q, Liu J, Herrera G, Hiya FE. Decreased Macular Choriocapillaris Perfusion in Eyes With Macular Reticular Pseudodrusen Imaged With Swept-Source OCT Angiography. Investigative Ophthalmology & Visual Science. 2023 Apr 3;64(4):15-.
14. Zhang Q, Shi Y, Shen M, Cheng Y, Zhou H, Feuer W, de Sisternes L, Gregori G, Rosenfeld PJ, Wang RK. Does the outer retinal thickness around geographic atrophy represent another clinical biomarker for predicting growth?. American journal of ophthalmology. 2022 Dec 1;244:79-87.
15. Zhou H, Liu J, Laiginhas R, Zhang Q, Cheng Y, Zhang Y, Shi Y, Shen M, Gregori G, Rosenfeld PJ, Wang RK. Depth-resolved visualization and automated quantification of hyperreflective foci on OCT scans using optical attenuation coefficients. Biomedical optics express. 2022 Aug 1;13(8):4175-89.

16. Lu Y, Zhou H, Zhou X, Cheng Y, Wang RK. Correlation between laser speckle flowgraphy and oct-derived retinal and choroidal metrics in healthy human eye. Translational Vision Science & Technology. 2022 Jun 1;11(6):15-.
17. Chu Z, Shi Y, Zhou X, Wang L, Zhou H, Laiginhas R, Zhang Q, Cheng Y, Shen M, de Sisternes L, Durbin MK. Optical coherence tomography measurements of the retinal pigment epithelium to Bruch membrane thickness around geographic atrophy correlate with growth. American journal of ophthalmology. 2022 Apr 1;236:249-60.
18. Chu Z, Wang L, Zhou X, Shi Y, Cheng Y, Laiginhas R, Zhou H, Shen M, Zhang Q, de Sisternes L, Lee AY. Automatic geographic atrophy segmentation using optical attenuation in OCT scans with deep learning. Biomedical optics express. 2022 Mar 1;13(3):1328-43.
19. Lu J, Deegan AJ, Cheng Y, Liu T, Zheng Y, Mandell SP, Wang RK. Application of OCT-derived attenuation coefficient in acute burn-damaged skin. Lasers in Surgery and Medicine. 2021 Nov;53(9):1192-200.
20. Lu J, Deegan AJ, Cheng Y, Mandell SP, Wang RK. OCT-Based Angiography and Surface Topography in Burn-Damaged Skin. Lasers in Surgery and Medicine. 2021 Aug;53(6):849-60.
21. Xie Z, Wang G, Cheng Y, Zhang Q, Le MN, Wang RK. Optical coherence tomography angiography measures blood pulsatile waveforms at variable tissue depths. Quantitative Imaging in Medicine and Surgery. 2021 Mar;11(3):907.
22. Zhou K, Song S, Legocki A, Cheng Y, Ding L, Rezaei KA, Wang RK, Cabrera MT. Quantitative handheld swept-source optical coherence tomography angiography in awake preterm and full-term infants. Translational Vision Science & Technology. 2020 Dec 1;9(13):19-.
23. Wei W, Zhang Q, Rayner SG, Qin W, Cheng Y, Wang F, Zheng Y, Wang RK. Automated vessel diameter quantification and vessel tracing for OCT angiography. Journal of biophotonics. 2020 Dec;13(12):e202000248.
24. Wang G, Le NM, Hu X, Cheng Y, Jacques SL, Subhash H, Wang RK. Semi-automated registration and segmentation for gingival tissue volume measurement on 3D OCT images. Biomedical Optics Express. 2020 Aug 1;11(8):4536-47.
25. Chu Z, Zhou H, Cheng Y, Zhang Q, Wang RK. Improving visualization and quantitative assessment of choriocapillaris with swept source OCTA through registration and averaging applicable to clinical systems. Scientific reports. 2018 Nov 14;8(1):16826.

Bibliography

1. Bourne, R. *et al.* Trends in prevalence of blindness and distance and near vision impairment over 30 years: an analysis for the Global Burden of Disease Study. *Lancet Glob. Health* **9**, e130–e143 (2021).
2. Steinmetz, J. D. *et al.* Causes of blindness and vision impairment in 2020 and trends over 30 years, and prevalence of avoidable blindness in relation to VISION 2020: the Right to Sight: an analysis for the Global Burden of Disease Study. *Lancet Glob. Health* **9**, e144–e160 (2021).
3. Digital Ocular Fundus Imaging: A Review | Ophthalmologica | Karger Publishers. https://karger.com/oph/article/226/4/161/255375/Digital-Ocular-Fundus-Imaging-A-Review.
4. Spaide, R. F. Peripheral areas of nonperfusion in treated central retinal vein occlusion as imaged by wide-field fluorescein angiography. *Retina* **May;31(5):829–37**, (2011).
5. Ocular ultrasonography focused on the posterior eye segment: what radiologists should know | Insights into Imaging. https://link.springer.com/article/10.1007/s13244-016-0471-z.
6. Huang, D. *et al.* Optical Coherence Tomography. *Science* **254**, 1178–1181 (1991).
7. Drexler, W. *et al.* Optical coherence tomography today: speed, contrast, and multimodality. *J. Biomed. Opt.* **19**, 071412 (2014).
8. Boer, J. F. de, Leitgeb, R. & Wojtkowski, M. Twenty-five years of optical coherence tomography: the paradigm shift in sensitivity and speed provided by Fourier domain OCT [Invited]. *Biomed. Opt. Express* **8**, 3248–3280 (2017).
9. Boer, J. F. de *et al.* Improved signal-to-noise ratio in spectral-domain compared with time-domain optical coherence tomography. *Opt. Lett.* **28**, 2067–2069 (2003).
10. Liu, J. *et al.* Diagnosing Persistent Hypertransmission Defects on En Face OCT Imaging of Age-Related Macular Degeneration. *Ophthalmol. Retina* **6**, 387–397 (2022).
11. Liu, J. *et al.* Multimodal Imaging and En Face OCT Detection of Calcified Drusen in Eyes with Age-Related Macular Degeneration. *Ophthalmol. Sci.* **2**, 100162 (2022).
12. Miller, A. R. *et al.* Comparison between spectral-domain and swept-source optical coherence tomography angiographic imaging of choroidal neovascularization. *Invest. Ophthalmol. Vis. Sci.* **58**, 1499–505 (2017).
13. Zhang, Q. *et al.* Wide-field optical coherence tomography based microangiography for retinal imaging. *Sci Rep* **25;6(1):22017**, (2016).

14. Kraus, M. F. *et al.* Motion correction in optical coherence tomography volumes on a per A-scan basis using orthogonal scan patterns. *Biomed. Opt. Express* **3**, 1182–99 (2012).

15. Wei, D. W., Deegan, A. J. & Wang, R. K. Automatic motion correction for in vivo human skin optical coherence tomography angiography through combined rigid and nonrigid registration. *J. Biomed. Opt.* **22**, (2017).

16. Kraus, M. F. & Hornegger, J. OCT Motion Correction. in *Optical Coherence Tomography: Technology and Applications* (eds. Drexler, W. & Fujimoto, J. G.) 459–476 (Springer International Publishing, Cham, 2015). doi:10.1007/978-3-319-06419-2_16.

17. Izatt, J. A., Choma, M. A. & Dhalla, A.-H. Theory of Optical Coherence Tomography. in *Optical Coherence Tomography: Technology and Applications* (eds. Drexler, W. & Fujimoto, J. G.) 65–94 (Springer International Publishing, Cham, 2015). doi:10.1007/978-3-319-06419-2_3.

18. Subhash, H. M. Full-Field and Single-Shot Full-Field Optical Coherence Tomography: A Novel Technique for Biomedical Imaging Applications. *Adv. Opt. Technol.* **2012**, e435408 (2012).

19. de Boer, J. F. Spectral/Fourier Domain Optical Coherence Tomography. in *Optical Coherence Tomography: Technology and Applications* (eds. Drexler, W. & Fujimoto, J. G.) 165–193 (Springer International Publishing, Cham, 2015). doi:10.1007/978-3-319-06419-2_6.

20. Andretzky, P. *et al.* Optical coherence tomography by spectral radar: dynamic range estimation and in-vivo measurements of skin. in *Optical and Imaging Techniques for Biomonitoring IV* vol. 3567 78–87 (SPIE, 1999).

21. Mitsui, T. Dynamic Range of Optical Reflectometry with Spectral Interferometry. *Jpn. J. Appl. Phys.* **38**, 6133 (1999).

22. Fercher, A. F., Hitzenberger, C. K., Kamp, G. & El-Zaiat, S. Y. Measurement of intraocular distances by backscattering spectral interferometry. *Opt. Commun.* **117**, 43–48 (1995).

23. Leitgeb, R. A. & Wojtkowski, M. Complex and Coherence-Noise Free Fourier Domain Optical Coherence Tomography. in *Optical Coherence Tomography: Technology and Applications* (eds. Drexler, W. & Fujimoto, J. G.) 195–224 (Springer International Publishing, Cham, 2015). doi:10.1007/978-3-319-06419-2_7.

24. Drexler, W. *et al.* Ultrahigh Resolution Optical Coherence Tomography. in *Optical Coherence Tomography: Technology and Applications* (eds. Drexler, W. & Fujimoto, J. G.) 277–318 (Springer International Publishing, Cham, 2015). doi:10.1007/978-3-319-06419-2_10.

25. Leitgeb, R., Hitzenberger, C. K. & Fercher, A. F. Performance of fourier domain vs. time domain optical coherence tomography. *Opt. Express* **11**, 889–894 (2003).

26. Chinn, S. R., Swanson, E. A. & Fujimoto, J. G. Optical coherence tomography using a frequency-tunable optical source. *Opt. Lett.* **22**, 340–342 (1997).

27. Bouma, B. E., Tearney, G. J., Vakoc, B. & Yun, S. H. Optical Frequency Domain Imaging. in *Optical Coherence Tomography: Technology and Applications* (eds. Drexler, W. & Fujimoto, J. G.) 225–254 (Springer International Publishing, Cham, 2015). doi:10.1007/978-3-319-06419-2_8.

28. Choma, M. A., Sarunic, M. V., Yang, C. & Izatt, J. A. Sensitivity advantage of swept source and Fourier domain optical coherence tomography. *Opt. Express* **11**, 2183–2189 (2003).

29. Huang, D. *et al.* 400 MHz ultrafast optical coherence tomography. *Opt. Lett.* **45**, 6675–6678 (2020).

30. Choi, W. *et al.* Ultrahigh-speed, swept-source optical coherence tomography angiography in nonexudative age-related macular degeneration with geographic atrophy. *Ophthalmology* **122**, 2532–2544 (2015).

31. Zhi, Z., Qin, W., Wang, J., Wei, W. & Wang, R. K. 4D optical coherence tomography-based micro-angiography achieved by 1.6-MHz FDML swept source. *Opt. Lett.* **40**, 1779–1782 (2015).

32. WANG, Z. *et al.* Cubic meter volume optical coherence tomography. *Optica* **3**, 1496–1503 (2016).

33. Song, S., Xu, J. & Wang, R. K. Long-range and wide field of view optical coherence tomography for in vivo 3D imaging of large volume object based on akinetic programmable swept source. *Biomed. Opt. Express* **7**, 4734–4748 (2016).

34. Jacques, S. L. Optical properties of biological tissues: a review. *Phys. Med. Biol.* **58**, R37 (2013).

35. Wang, R. K. *et al.* Three dimensional optical angiography. *Opt. Express* **15**, 4083–97 (2007).

36. Wang, R. K., An, L., Francis, P. & Wilson, D. J. Depth-resolved imaging of capillary networks in retina and choroid using ultrahigh sensitive optical microangiography. *Opt. Lett.* **35**, 1467–1469 (2010).

37. Yousefi, S., Zhi, Z. & Wang, R. K. Eigendecomposition-Based Clutter Filtering Technique for Optical Microangiography. *IEEE Trans. Biomed. Eng.* **58**, 2316–2323 (2011).

38. Chen, C.-L. & Wang, R. K. Optical coherence tomography based angiography [Invited]. *Biomed. Opt. Express* **8**, 1056–1082 (2017).

39. Cheng, Y. *et al.* Statistical analysis of motion contrast in optical coherence tomography angiography. *J. Biomed. Opt.* **20**, 116004 (2015).

40. Barton, J. K. & Stromski, S. Flow measurement without phase information in optical coherence tomography images. *Opt. Express* **13**, 5234–5239 (2005).

41. Jonathan, E., Enfield, J. & Leahy, M. J. Correlation mapping method for generating microcirculation morphology from optical coherence tomography (OCT) intensity images. *J. Biophotonics* **4**, 583–587 (2011).

42. Fingler, J., Schwartz, D., Yang, C. & Fraser, S. E. Mobility and transverse flow visualization using phase variance contrast with spectral domain optical coherence tomography. *Opt. Express* **15**, 12636–12653 (2007).

43. Kim, D. Y. *et al.* In vivo volumetric imaging of human retinal circulation with phase-variance optical coherence tomography. *Biomed. Opt. Express* **2**, 1504–1513 (2011).

44. Thorell, M. R. *et al.* Swept-source OCT angiography of macular telangiectasia type 2. *Ophthalmic Surg. Lasers Imaging Retina* **45**, 369–380 (2014).

45. Jia, Y. *et al.* Split-spectrum amplitude-decorrelation angiography with optical coherence tomography. *Opt. Express* **20**, 4710–4725 (2012).

46. Ferris, F. L. *et al.* Clinical Classification of Age-related Macular Degeneration. *Ophthalmology* **120**, 844–851 (2013).

47. M., E. *et al.* Role of optical coherence tomography imaging in predicting progression of age-related macular disease: a survey. *Diagnostics* **11**, 2313.

48. R., R. *et al.* Deep learning-based single-shot prediction of differential effects of anti-VEGF treatment in patients with diabetic macular edema. *Biomed Opt Express* **11**, 1139–1152.

49. Virgili, G. *et al.* Optical coherence tomography (OCT) for detection of macular oedema in patients with diabetic retinopathy. *Cochrane Database Syst. Rev.* (2015) doi:10.1002/14651858.CD008081.pub3.

50. OCT for glaucoma diagnosis, screening and detection of glaucoma progression | British Journal of Ophthalmology. https://bjo.bmj.com/content/98/Suppl_2/ii15.short.

51. M., A. & S, D. J. Optical coherence tomography–current and future applications. - *DOI - PMC* **24**, 213–221.

52. A., S. E. & G, F. J. The ecosystem that powered the translation of OCT from fundamental research to clinical and commercial impact [Invited. - *DOI - PMC* **8**, 1638–1664.

53. T., K. & R, H. High-speed OCT light sources and systems [Invited. - *DOI - PMC* **8**, 828–859.

54. G., Z. *et al.* Clinically relevant deep learning for detection and quantification of geographic atrophy from optical coherence tomography: a model development and external validation study. *Lancet Digit Health* **3**, 665–675.

55. M., P. *et al.* Association of complement C3 inhibitor pegcetacoplan with reduced photoreceptor degeneration beyond areas of geographic atrophy. - *DOI - PMC - PubMed* **12**, 17870.

56. D., V. W. *et al.* Predicting topographic disease progression and treatment response of pegcetacoplan in geographic atrophy quantified by deep learning. *Ophthalmol Retina* **7**, 4–13.

57. Chu, Z. *et al.* Automatic geographic atrophy segmentation using optical attenuation in OCT scans with deep learning. *Biomed. Opt. Express* **13**, 1328–1343 (2022).

58. Y., K. *et al.* Detection of nonexudative macular neovascularization on structural OCT images using vision transformers. - *DOI - PMC - PubMed* **2**, 100197.

59. V., P. *et al.* A deep learning model for automated segmentation of geographic atrophy imaged using swept-source OCT. *Ophthalmol Retina* **7**, 127–141.

60. S., S.-Z. *et al.* Deep learning-enabled volumetric cone photoreceptor segmentation in adaptive optics optical coherence tomography images of normal and diseased eyes. *Biomed Opt Express* **14**, 815–833.

61. Kashani, A. H. *et al.* Optical coherence tomography angiography: A comprehensive review of current methods and clinical applications. *Prog. Retin. Eye Res.* **60**, 66–100 (2017).

62. A., S. M., S., M., M., G., F., R. & F, A. J. Retinal and choroidal changes in AMD: A systematic review and meta-analysis of spectral-domain optical coherence tomography studies. *Surv Ophthalmol* **68**, 54–66.

63. Cao, D. *et al.* Hyperreflective Foci, Optical Coherence Tomography Progression Indicators in Age-Related Macular Degeneration, Include Transdifferentiated Retinal Pigment Epithelium. *Invest. Ophthalmol. Vis. Sci.* **62**, 34–34 (2021).

64. Zhang, Q. *et al.* Accurate estimation of choriocapillaris flow deficits beyond normal intercapillary spacing with swept source OCT angiography. *Quant. Imaging Med. Surg.* **8**, (2018).

65. Chu, Z., Zhou, H., Cheng, Y., Zhang, Q. & Wang, R. K. Improving visualization and quantitative assessment of choriocapillaris with swept source OCTA through registration and averaging applicable to clinical systems. *Sci. Rep.* **8**, 16826 (2018).

66. Chu, Z., Gregori, G., Rosenfeld, P. J. & Wang, R. K. Quantification of Choriocapillaris with Optical Coherence Tomography Angiography: A Comparison Study. *Am. J. Ophthalmol.* **208**, 111–123 (2019).

67. Fleckenstein, M. *et al.* Age-related macular degeneration. *Nat Rev Primer* **7**, 31 (2021).

68. Zhou, H. *et al.* Depth-resolved visualization and automated quantification of hyperreflective foci on OCT scans using optical attenuation coefficients. *Biomed. Opt. Express* **13**, 4175–4189 (2022).

69. Natural history of subclinical neovascularization in nonexudative age-related macular degeneration using swept-source OCT angiography. *Ophthalmology* **125**, 255–66 (2018).

70. Roisman, L. *et al.* Optical coherence tomography angiography of asymptomatic neovascularization in intermediate age-related macular degeneration. *Ophthalmology* **123**, 1309–19 (2016).

71. Deegan, A. J. *et al.* Optical coherence tomography angiography of normal skin and inflammatory dermatologic conditions. *Lasers Surg. Med.* **50**, 183–93 (2018).

72. Tan, H. E. I. *et al.* Optical coherence tomography of the tympanic membrane and middle ear: a review. *Otolaryngol. Neck Surg.* **159**, 424–38 (2018).

73. Le, N. M. *et al.* A noninvasive imaging and measurement using optical coherence tomography angiography for the assessment of gingiva: An in vivo study. *J. Biophotonics* **11:e201800242**, (2018).

74. Vignali, L., Solinas, E. & Emanuele, E. Research and clinical applications of optical coherence tomography in invasive cardiology: a review. *Curr. Cardiol. Rev.* **10**, 369–76 (2014).

75. Spaide, R. F., Fujimoto, J. G. & Waheed, N. K. Image artifacts in optical coherence angiography. Retina.

76. Chu, Z. *et al.* Quantitative assessment of the retinal microvasculature using optical coherence tomography angiography. *J. Biomed. Opt.* **21**, 066008 (2016).

77. Li, P. *et al.* Single-shot angular compounded optical coherence tomography angiography by splitting full-space B-scan modulation spectrum for flow contrast enhancement. *Opt. Lett.* **41**, 1058–61 (2016).

78. Wang, R. K. *et al.* Wide-field optical coherence tomography angiography enabled by two repeated measurements of B-scans. *Opt. Lett.* **41**, 2330–3 (2016).

79. Li, P. *et al.* Hybrid averaging offers high-flow contrast by cost apportionment among imaging time, axial, and lateral resolution in optical coherence tomography angiography. *Opt. Lett.* **41**, 3944–7 (2016).

80. Wong, A., Mishra, A., Bizheva, K. & Clausi, D. A. General Bayesian estimation for speckle noise reduction in optical coherence tomography retinal imagery. *Opt. Express* **18**, 8338–52 (2010).

81. Sheehy, C. K. *et al.* High-speed, image-based eye tracking with a scanning laser ophthalmoscope. *Biomed. Opt. Express* **3**, 2611–22 (2012).

82. Kocaoglu, O. P. *et al.* Adaptive optics optical coherence tomography with dynamic retinal tracking. *Biomed. Opt. Express* **5**, 2262–84 (2014).

83. Potsaid, B. *et al.* Ultrahigh speed spectral/Fourier domain OCT ophthalmic imaging at 70,000 to 312,500 axial scans per second. *Opt. Express* **16**, 15149–69 (2008).

84. Zang, P. *et al.* Automated three-dimensional registration and volume rebuilding for wide-field angiographic and structural optical coherence tomography. *J. Biomed. Opt.* **22**, (2017).

85. Hendargo, H. C. *et al.* Automated non-rigid registration and mosaicing for robust imaging of distinct retinal capillary beds using speckle variance optical coherence tomography. *Biomed. Opt. Express* **4**, 803–21 (2013).

86. Lezama, J. *et al.* Segmentation guided registration of wide field-of-view retinal optical coherence tomography volumes. *Biomed. Opt. Express* **7**, (2016).

87. Wang, G. *et al.* Semi-automated registration and segmentation for gingival tissue volume measurement on 3D OCT images. *Biomed. Opt. Express* **11**, 4536–47 (2020).

88. Niemeijer, M. *et al.* in *Registration of 3D spectral OCT volumes using 3D SIFT feature point matching. Medical Imaging 2009: Image Processing* (ed. M.) (International Society for Optics and Photonics, 2009).

89. Staring, M., Klein, S. & Pluim, J. P. A rigidity penalty term for nonrigid registration. *Med. Phys.* **34**, 4098–108 (2007).

90. Thévenaz, P. & Unser, M. Optimization of mutual information for multiresolution image registration. *IEEE Trans. Image Process.* **9**, 2083–99 (2000).

91. Klein, S., Pluim, J. P., Staring, M. & Viergever, M. A. Adaptive stochastic gradient descent optimisation for image registration. *Int. J. Comput. Vis.* **81**, (2009).

92. Lester, H. & Arridge, S. A survey of hierarchical non-linear medical image registration. *Pattern Recognit* **32**, 129–49 (1999).

93. Klein, S., Staring, M., Murphy, K., Viergever, M. A. & Pluim, J. P. Elastix: a toolbox for intensity-based medical image registration. *IEEE Trans. Med. Imaging* **29**, 196–205 (2010).

94. Zhang, Q. *et al.* Wide-field imaging of retinal vasculature using optical coherence tomography-based microangiography provided by motion tracking. *J. Biomed. Opt.* **20**, (2015).

95. An, L., Subhush, H., Wilson, D. & Wang, R. High-resolution wide-field imaging of retinal and choroidal blood perfusion with optical microangiography. *J. Biomed. Opt.* **15**, (2010).

96. Yin, X., Chao, W., JR, & R.K. User-guided segmentation for volumetric retinal optical coherence tomography images. *J. Biomed. Opt.* **19**, (2014).

97. Chu, Z. *et al.* Quantifying choriocapillaris flow deficits using global and localized thresholding methods: a correlation study. *Quant. Imaging Med. Surg.* **8**, (2018).

98. Shamonin, D. P. *et al.* Fast parallel image registration on CPU and GPU for diagnostic classification of Alzheimer's disease.

99. TE, C., A, R., NK, W. & JS, D. A review of optical coherence tomography angiography (OCTA. *Int J Retina Vitr.* **15;1(1):5**, (2015).

100. TE, C. *et al.* Visualization of the retinal vasculature using wide-field montage optical coherence tomography angiography. *Ophthalmic Surg Lasers Imaging Retina* **Jun;46(6):611–6**, (2015).

101. Ortiz, S. *et al.* Optical distortion correction in optical coherence tomography for quantitative ocular anterior segment by three-dimensional imaging. *Opt Express* **1;18(3):2782–96**, (2010).

102. Wang, D. *et al.* Correction of image distortions in endoscopic optical coherence tomography based on two-axis scanning MEMS mirrors. *Biomed Opt Express* **6;4(10):2066–77**, (2013).

103. Lee, S., Reinhardt, J. M., Cattin, P. C. & Abràmoff, M. D. Objective and expert-independent validation of retinal image registration algorithms by a projective imaging distortion model. *Med Image Anal* **Aug;14(4):539–49**, (2010).

104. Cheung, C. M. G. & Wong, T. Y. Clinical use of optical coherence tomography angiography in diabetic retinopathy treatment: Ready for showtime? *JAMA Ophthalmol* **1;136(7):729–30**, (2018).

105. Podoleanu, A., Charalambous, I., Plesea, L., Dogariu, A. & Rosen, R. Correction of distortions in optical coherence tomography imaging of the eye. *Phys Med Biol* **7;49(7):1277–94**, (2004).

106. S, J., JAN, B., A, B., AGH, P. & JJJ, D. Real-time correction of geometric distortion artefacts in large-volume optical coherence tomography. *Meas. Sci. Technol.* **24**, 0–0 (2013).

107. Alcantarilla, P. F., Bartoli, A. & Davison, A. J. KAZE Features. in *Computer Vision – ECCV 2012* 214–27 (Springer, Berlin Heidelberg, 2012).

108. Snyder, J. P. *Map Projections: A Working Manual*. *Professional Paper* https://pubs.usgs.gov/publication/pp1395 (1987) doi:10.3133/pp1395.

109. Fischler, M. A. & Bolles, R. C. Random sample consensus: a paradigm for model fitting with applications to image analysis and automated cartography. *Commun ACM* **1;24(6):381–95**, (1981).

110. Reif, R. *et al.* Quantifying optical microangiography images obtained from a spectral domain optical coherence tomography system. *Int J Biomed Imaging* (2012).

111. Ganjee, R., Moghaddam, M. E. & Nourinia, R. Automatic segmentation of abnormal capillary nonperfusion regions in optical coherence tomography angiography images using marker-controlled watershed algorithm. *J Biomed Opt* **Sep;23(9):1–16**, (2018).

112. Koulisis, N. *et al.* Correlating Changes in the Macular Microvasculature and Capillary Network to Peripheral Vascular Pathologic Features in Familial Exudative Vitreoretinopathy. *Ophthalmol Retina* **Jul;3(7):597–606**, (2019).

113. Kuo, A. N. *et al.* Correction of ocular shape in retinal optical coherence tomography and effect on current clinical measures. *Am J Ophthalmol* **Aug;156(2):304–11**, (2013).

114. Tan, C. S. *et al.* Measuring the precise area of peripheral retinal non-perfusion using ultra-widefield imaging and its correlation with the ischaemic index. *Br J Ophthalmol* **Feb;100(2):235–9**, (2016).

115. Cheng, Y., Chu, Z. & Wang, R. K. Robust three-dimensional registration on optical coherence tomography angiography for speckle reduction and visualization. *Quant. Imaging Med. Surg.* **11**, 879–894 (2021).

116. Abdelfattah, N. S. *et al.* Drusen Volume as a Predictor of Disease Progression in Patients With Late Age-Related Macular Degeneration in the Fellow Eye. *Invest. Ophthalmol. Vis. Sci.* **57**, 1839–1846 (2016).

117. Tan, A. C. S. *et al.* Calcified nodules in retinal drusen are associated with disease progression in age-related macular degeneration. *Sci. Transl. Med.* **10**, eaat4544 (2018).

118. Chen, L. *et al.* SUBRETINAL DRUSENOID DEPOSIT IN AGE-RELATED MACULAR DEGENERATION: Histologic Insights Into Initiation, Progression to Atrophy, and Imaging. *Retina* **40**, 618–631 (2020).

119. Sura, A. A. *et al.* Measuring the Contributions of Basal Laminar Deposit and Bruch's Membrane in Age-Related Macular Degeneration. *Invest. Ophthalmol. Vis. Sci.* **61**, 19–19 (2020).

120. Shi, Y., Yang, J., Feuer, W., Gregori, G. & Rosenfeld, P. J. Persistent Hypertransmission Defects on En Face OCT Imaging as a Stand-Alone Precursor for the Future Formation of Geographic Atrophy. *Ophthalmol Retina* **5**, 1214–1225 (2021).

121. Guymer, R. H. *et al.* Incomplete Retinal Pigment Epithelial and Outer Retinal Atrophy in Age-Related Macular Degeneration: Classification of Atrophy Meeting Report 4. *Ophthalmology* **127**, 394–409 (2020).

122. Corvi, F. *et al.* Comparison between B-Scan and En Face Images for Incomplete and Complete Retinal Pigment Epithelium and Outer Retinal Atrophy. *Ophthalmol Retina* **7**, 999–1009 (2023).

123. Moult, E. M. *et al.* Analysis of correlations between local geographic atrophy growth rates and local OCT angiography-measured choriocapillaris flow deficits. *Biomed. Opt. Express* **12**, 4573–4595 (2021).

124. Shen, M. *et al.* Decreased Central Macular Choriocapillaris Perfusion Correlates With Increased Low Luminance Visual Acuity Deficits. *Am. J. Ophthalmol.* **253**, 1–11 (2023).

125. Kar, D. *et al.* Choriocapillaris Impairment Is Associated With Delayed Rod-Mediated Dark Adaptation in Age-Related Macular Degeneration. *Invest. Ophthalmol. Vis. Sci.* **64**, 41–41 (2023).

126. Nassisi, M., Tepelus, T., Corradetti, G. & Sadda, S. R. Relationship Between Choriocapillaris Flow and Scotopic Microperimetry in Early and Intermediate Age-related Macular Degeneration. *Am. J. Ophthalmol.* **222**, 302–309 (2021).

127. Zhang, Q. *et al.* A Novel Strategy for Quantifying Choriocapillaris Flow Voids Using Swept-Source OCT Angiography. *Invest. Ophthalmol. Vis. Sci.* **59**, 203–211 (2018).

128. Sarks, J. P., Sarks, S. H. & Killingsworth, M. C. Evolution of soft drusen in age-related macular degeneration. *Eye* **8**, 269–283 (1994).

129. Spaide, R. F. & Curcio, C. A. DRUSEN CHARACTERIZATION WITH MULTIMODAL IMAGING. *Retina* **30**, 1441–1454 (2010).

130. Chen, L., Messinger, J. D., Kar, D., Duncan, J. L. & Curcio, C. A. Biometrics, Impact, and Significance of Basal Linear Deposit and Subretinal Drusenoid Deposit in Age-Related Macular Degeneration. *Invest. Ophthalmol. Vis. Sci.* **62**, 33–33 (2021).

131. Thompson, R. B. *et al.* Identification of hydroxyapatite spherules provides new insight into subretinal pigment epithelial deposit formation in the aging eye. *Proc. Natl. Acad. Sci.* **112**, 1565–1570 (2015).

132. Pilgrim, M. G. *et al.* Characterization of Calcium Phosphate Spherical Particles in the Subretinal Pigment Epithelium–Basal Lamina Space in Aged Human Eyes. *Ophthalmol. Sci.* **1**, 100053 (2021).

133. Jaffe, G. J. *et al.* Imaging Features Associated with Progression to Geographic Atrophy in Age-Related Macular Degeneration: Classification of Atrophy Meeting Report 5. *Ophthalmol Retina* **5**, 855–867 (2021).

134. Shi, Y. *et al.* Validation of a Compensation Strategy Used to Detect Choriocapillaris Flow Deficits Under Drusen With Swept Source OCT Angiography. *Am. J. Ophthalmol.* **220**, 115–127 (2020).

135. Jiang, X. *et al.* Validation of a Novel Automated Algorithm to Measure Drusen Volume and Area Using Swept Source Optical Coherence Tomography Angiography. *Transl. Vis. Sci. Technol.* **10**, 11–11 (2021).

136. Lu, J. *et al.* Automated segmentation and quantification of calcified drusen in 3D swept source OCT imaging. *Biomed. Opt. Express* **14**, 1292–1306 (2023).

137. Rosenfeld, P. J., Cheng, Y., Shen, M., Gregori, G. & Wang, R. K. Unleashing the power of optical attenuation coefficients to facilitate segmentation strategies in OCT imaging of age-related macular degeneration: perspective. *Biomed. Opt. Express* **14**, 4947–4963 (2023).

138. Wang, R. K. *et al.* An explanation for why choroidal blood vessels appear dark on clinical OCT images. *Invest. Ophthalmol. Vis. Sci.* **58**, 4754–4754 (2017).

139. Laiginhas, R. *et al.* Multimodal Imaging, OCT B-Scan Localization, and En Face OCT Detection of Macular Hyperpigmentation in Eyes with Intermediate Age-Related Macular Degeneration. *Ophthalmol. Sci.* **2**, 100116 (2022).

140. Zhang, A., Zhang, Q., Chen, C.-L. & Wang, R. Methods and algorithms for optical coherence tomography-based angiography: a review and comparison. *J. Biomed. Opt.* **20**, 100901 (2015).

141. Zhang, A., Zhang, Q. & Wang, R. K. Minimizing projection artifacts for accurate presentation of choroidal neovascularization in OCT micro-angiography. *Biomed. Opt. Express* **6**, 4130–4143 (2015).

142. Chu, Z., Zhang, Q., Gregori, G., Rosenfeld, P. J. & Wang, R. K. Guidelines for Imaging the Choriocapillaris Using OCT Angiography. *Am. J. Ophthalmol.* **222**, 92–101 (2021).

143. Laiginhas, R. *et al.* Persistent Hypertransmission Defects Detected on En Face Swept Source Optical Computed Tomography Images Predict the Formation of Geographic Atrophy in Age-Related Macular Degeneration. *Am. J. Ophthalmol.* **237**, 58–70 (2022).

144. Feurer, M. & Hutter, F. Hyperparameter optimization. *Autom. Mach. Learn. Methods Syst. Chall.* 3–33 (2019).

145. Lamouche, G. *et al.* Review of tissue simulating phantoms with controllable optical, mechanical and structural properties for use in optical coherence tomography. *Biomed. Opt. Express* **3**, 1381–98 (2012).

146. Zhou, K. *et al.* Visualizing choriocapillaris using swept-source optical coherence tomography angiography with various probe beam sizes. *Biomed. Opt. Express* **10**, 2847–2860 (2019).

147. Greig, E. C. *et al.* Assessment of Choriocapillaris Flow Prior to Nascent Geographic Atrophy Development Using Optical Coherence Tomography Angiography. *Invest. Ophthalmol. Vis. Sci.* **65**, 33–33 (2024).

148. Byon, I., Ji, Y., Alagorie, A. R., Tiosano, L. & Sadda, S. R. TOPOGRAPHIC ASSESSMENT OF CHORIOCAPILLARIS FLOW DEFICITS IN THE INTERMEDIATE AGE-RELATED MACULAR DEGENERATION EYES WITH HYPOREFLECTIVE CORES INSIDE DRUSEN. *Retina* **41**, 393–401 (2021).

149. Lane, M. *et al.* Visualizing the Choriocapillaris Under Drusen: Comparing 1050-nm Swept-Source Versus 840-nm Spectral-Domain Optical Coherence Tomography Angiography. *Invest. Ophthalmol. Vis. Sci.* **57**, OCT585–OCT590 (2016).

150. Lauermann, J. L., Eter, N. & Alten, F. Optical Coherence Tomography Angiography Offers New Insights into Choriocapillaris Perfusion. *Ophthalmologica* **239**, 74–84 (2018).

151. Chatziralli, I., Theodossiadis, G., Panagiotidis, D., Pousoulidi, P. & Theodossiadis, P. Choriocapillaris Vascular Density Changes in Patients with Drusen: Cross-Sectional Study Based on Optical Coherence Tomography Angiography Findings. *Ophthalmol. Ther.* **7**, 101–107 (2018).

152. Corvi, F. *et al.* CHORIOCAPILLARIS FLOW DEFICITS AS A RISK FACTOR FOR PROGRESSION OF AGE-RELATED MACULAR DEGENERATION. *Retina* **41**, 686–693 (2021).

153. Thulliez, M. *et al.* Correlations between Choriocapillaris Flow Deficits around Geographic Atrophy and Enlargement Rates Based on Swept-Source OCT Imaging. *Ophthalmol. Retina* **3**, 478–488 (2019).

154. Shi, Y. *et al.* Correlations Between Choriocapillaris and Choroidal Measurements and the Growth of Geographic Atrophy Using Swept Source OCT Imaging. *Am. J. Ophthalmol.* **224**, 321–331 (2021).

155. You, Q. S. *et al.* Geographic Atrophy Progression Is Associated With Choriocapillaris Flow Deficits Measured With Optical Coherence Tomographic Angiography. *Invest. Ophthalmol. Vis. Sci.* **62**, 28–28 (2021).

156. Arya, M., Sabrosa, A. S., Duker, J. S. & Waheed, N. K. Choriocapillaris changes in dry age-related macular degeneration and geographic atrophy: a review. *Eye Vis.* **5**, 22 (2018).

157. Schmitz-Valckenberg, S. *et al.* GEOGRAPHIC ATROPHY: Semantic Considerations and Literature Review. *Retina* **36**, 2250–2264 (2016).

158. Holz, F. G. *et al.* Progression of Geographic Atrophy and Impact of Fundus Autofluorescence Patterns in Age-related Macular Degeneration. *Am. J. Ophthalmol.* **143**, 463-472.e2 (2007).

159. Yung, M., Klufas, M. A. & Sarraf, D. Clinical applications of fundus autofluorescence in retinal disease. *Int J Retina Vitr.* **2**, 12 (2016).

160. Batioglu, F., Demirel, S., Özmert, E., Abdullayev, A. & Bilici, S. Short-term outcomes of switching anti-VEGF agents in eyes with treatment-resistant wet AMD. *BMC Ophthalmol.* **15**, 40 (2015).

161. Sadda, S. R. *et al.* Consensus Definition for Atrophy Associated with Age-Related Macular Degeneration on OCT: Classification of Atrophy Report 3. *Ophthalmology* **125**, 537–548 (2018).

162. Spaide, R. F. *et al.* Consensus Nomenclature for Reporting Neovascular Age-Related Macular Degeneration Data: Consensus on Neovascular Age-Related Macular Degeneration Nomenclature Study Group. *Ophthalmology* **127**, 616–636 (2020).

163. Lu, J. *et al.* Deep-learning-based automated measurement of outer retinal layer thickness for use in the assessment of age-related macular degeneration, applicable to both swept-source and spectral-domain OCT imaging. *Biomed. Opt. Express* **15**, 413–427 (2024).

164. Yehoshua, Z. *et al.* Comparison of Geographic Atrophy Growth Rates Using Different Imaging Modalities in the COMPLETE Study. *Ophthalmic Surg Lasers Imaging Retina* **46**, 413–22 (2015).

165. Sayegh, R. G. *et al.* A systematic comparison of spectral-domain optical coherence tomography and fundus autofluorescence in patients with geographic atrophy. *Ophthalmology* **118**, 1844–51 (2011).

166. Velaga, S. B., Nittala, M. G., Hariri, A. & Sadda, S. R. Correlation between Fundus Autofluorescence and En Face OCT Measurements of Geographic Atrophy. *Ophthalmol Retina* **6**, 676–683 (2022).

167. Schmitz-Valckenberg, S., Fleckenstein, M., Göbel, A. P., Hohman, T. C. & Holz, F. G. Optical coherence tomography and autofluorescence findings in areas with geographic atrophy due to age-related macular degeneration. *Invest. Ophthalmol. Vis. Sci.* **52**, 1–6 (2011).

168. Wu, Z. *et al.* Fundus Autofluorescence Characteristics of Nascent Geographic Atrophy in Age-Related Macular Degeneration. *Invest. Ophthalmol. Vis. Sci.* **56**, 1546–1552 (2015).

169. Wu, Z. *et al.* OCT Signs of Early Atrophy in Age-Related Macular Degeneration: Interreader Agreement: Classification of Atrophy Meetings Report 6. *Ophthalmol Retina* **6**, 4–14 (2022).

170. Corvi, F. *et al.* COMPARISON OF SPECTRALIS AND CIRRUS OPTICAL COHERENCE TOMOGRAPHY FOR THE DETECTION OF INCOMPLETE AND COMPLETE RETINAL PIGMENT EPITHELIUM AND OUTER RETINAL ATROPHY. *Retina* **41**, 1851–1857 (2021).

171. Schaal, K. B., Gregori, G. & Rosenfeld, P. J. En Face Optical Coherence Tomography Imaging for the Detection of Nascent Geographic Atrophy. *Am. J. Ophthalmol.* **174**, 145–154 (2017).

172. Nunes, R. P. *et al.* Predicting the progression of geographic atrophy in age-related macular degeneration with SD-OCT en face imaging of the outer retina. *Ophthalmic Surg Lasers Imaging Retina* **44**, 344–59 (2013).

173. Thulliez, M., Motulsky, E. H., Feuer, W., Gregori, G. & Rosenfeld, P. J. En Face Imaging of Geographic Atrophy Using Different Swept-Source OCT Scan Patterns. *Ophthalmol. Retina* **3**, 122–132 (2019).

174. Liu, J. *et al.* Onset and Progression of Persistent Choroidal Hypertransmission Defects in Intermediate Age-Related Macular Degeneration: A Novel Clinical Trial Endpoint. *Am. J. Ophthalmol.* **254**, 11–22 (2023).

175. Schmidt-Erfurth, U. *et al.* Role of Deep Learning-Quantified Hyperreflective Foci for the Prediction of Geographic Atrophy Progression. *Am. J. Ophthalmol.* **216**, 257–270 (2020).

176. Finger, R. P. *et al.* Reticular Pseudodrusen: A Risk Factor for Geographic Atrophy in Fellow Eyes of Individuals with Unilateral Choroidal Neovascularization. *Ophthalmology* **121**, 1252–1256 (2014).

177. Bird, A. C., Phillips, R. L. & Hageman, G. S. Geographic atrophy: a histopathological assessment. *JAMA Ophthalmol* **132**, 338–345 (2014).

178. Rudnicka, A. R. *et al.* Incidence of late-stage age-related macular degeneration in American whites: systematic review and meta-analysis. *Am J Ophthalmol* **160**, 85-93 3 (2015).

179. Fleckenstein, M. *et al.* The progression of geographic atrophy secondary to age-related macular degeneration. *Ophthalmology* **125**, 369–390 (2018).

180. Friedman, D. S. *et al.* Prevalence of age-related macular degeneration in the United States. *Arch Ophthalmol* **122**, 1019 (2004).

181. Wong, W. L. *et al.* Global prevalence of age-related macular degeneration and disease burden projection for 2020 and 2040: a systematic review and meta-analysis. *Lancet Glob. Health* **2**, 106–116 (2014).

182. Rosenfeld, P. J. Preventing the growth of geographic atrophy: an important therapeutic target in age-related macular degeneration. *Ophthalmology* **125**, 794–795 (2018).

183. Jaffe, G. J. *et al.* C5 inhibitor Avacincaptad pegol for geographic atrophy due to age-related macular degeneration: a randomized pivotal phase 2/3 trial. *Ophthalmology* **128**, 576–586 (2021).

184. Li, H., Chintalapudi, S. R. & Jablonski, M. M. Current drug and molecular therapies for the treatment of atrophic age-related macular degeneration: phase I to phase III clinical development. *Expert Opin Invest DrugsExpert Opin Invest Drugs* **26**, 1103–1114 (2017).

185. Liao, D. S. *et al.* Complement C3 inhibitor pegcetacoplan for geographic atrophy secondary to age-related macular degeneration: a randomized phase 2 trial. *Ophthalmology* **127**, 186–195 (2020).

186. Schmitz-Valckenberg, S. *et al.* Natural history of geographic atrophy progression secondary to age-related macular degeneration (Geographic Atrophy Progression Study. *Ophthalmology* **123**, 361–368 (2016).

187. Fleckenstein, M. *et al.* Tracking progression with spectral-domain optical coherence tomography in geographic atrophy caused by age-related macular degeneration. *Invest Ophthalmol Vis Sci* **51**, 3846–3852 (2010).

188. Fleckenstein, M. *et al.* High-resolution spectral domain-OCT imaging in geographic atrophy associated with age-related macular degeneration. *Invest Ophthalmol Vis Sci* **49**, 4137–4144 (2008).

189. Sunness, J. S. *et al.* The long-term natural history of geographic atrophy from age-related macular degeneration: enlargement of atrophy and implications for interventional clinical trials. *Ophthalmology* **114**, 271–277 (2007).

190. Yehoshua, Z. *et al.* Comparison of geographic atrophy measurements from the OCT fundus image and the sub-RPE slab image. *Ophthalmic Surg Lasers Imaging Retina* **44**, 127–132 (2013).

191. Niu, S., Sisternes, L., Chen, Q., Leng, T. & Rubin, D. L. Automated geographic atrophy segmentation for SD-OCT images using region-based CV model via local similarity factor. *Biomed Opt Express* **7**, 581–600 (2016).

192. Ramsey, D. J. *et al.* Automated image alignment and segmentation to follow progression of geographic atrophy in age-related macular degeneration. *Retina* **34**, 1296–1307 (2014).

193. Ji, Z., Chen, Q., Niu, S., Leng, T. & Rubin, D. L. Beyond retinal layers: a deep voting model for automated geographic atrophy segmentation in SD-OCT images. *Transl Vis Sci Technol* **7**, (2018).

194. Xu, R. *et al.* Automated geographic atrophy segmentation for SD-OCT images based on two-stage learning model. *Comput Biol Med* **105**, 102–111 (2019).

195. Keenan, T. D. *et al.* A deep learning approach for automated detection of geographic atrophy from color fundus photographs. *Ophthalmology* **126**, 1533–1540 (2019).

196. Chiu, S. J. *et al.* Validated automatic segmentation of AMD pathology including Drusen and geographic atrophy in SD-OCT images. *Invest Ophthalmol Vis Sci* **53**, 53–61 (2012).

197. Hu, Z., Wang, Z. & Sadda, S. R. Automated segmentation of geographic atrophy using deep convolutional neural networks. in *Medical Imaging 2018: Computer-Aided Diagnosis (International Society for Optics and Photonics* 1057511 (2018).

198. Xu, R., Niu, S., Gao, K. & Chen, Y. Multi-path 3D convolution neural network for automated geographic atrophy segmentation in SD-OCT images. in *International Conference on Intelligent Computing* 493–503 (Springer, 2018).

199. Wu, M. *et al.* Geographic atrophy segmentation in SD-OCT images using synthesized fundus autofluorescence imaging. *Comput Methods Programs Biomed* **182**, 105101 (2019).

200. Zhou, H. *et al.* Attenuation correction assisted automatic segmentation for assessing choroidal thickness and vasculature with swept-source OCT. *Biomed Opt Express* **9**, 6067–6080 (2018).

201. Vermeer, K. A., Mo, J., Weda, J. J., Lemij, H. G. & Boer, J. F. Depth-resolved model-based reconstruction of attenuation coefficients in optical coherence tomography. *Biomed Opt Express* **5**, 322–337 (2014).

202. Chu, Z. D. *et al.* OCT measurements of the retinal pigment epithelium to Bruch's membrane thickness around geographic atrophy correlate with growth. *Am J Ophthalmol* **236**, 249–260 (2022).

203. He, K., Zhang, X., Ren, S. & Sun, J. Delving deep into rectifiers: surpassing human-level performance on imagenet classification. in *Proceedings of the IEEE International Conference on Computer Vision* 1026–1034 (2015).

204. Yehoshua, Z. *et al.* Progression of geographic atrophy in age-related macular degeneration imaged with spectral domain optical coherence tomography. *Ophthalmology* **118**, 679–686 (2011).

205. Schaal, K. B., Rosenfeld, P. J., Gregori, G., Yehoshua, Z. & Feuer, W. J. Anatomic Clinical Trial Endpoints for Nonexudative Age-Related Macular Degeneration. *Ophthalmology* **123**, 1060–1079 (2016).

206. Yehoshua, Z. *et al.* Systemic complement inhibition with eculizumab for geographic atrophy in age-related macular degeneration: the COMPLETE study. *Ophthalmology* **121**, 693–701 (2014).

207. Feeny, A. K., Tadarati, M., Freund, D. E., Bressler, N. M. & Burlina, P. Automated segmentation of geographic atrophy of the retinal epithelium via random forests in AREDS color fundus images. *Comput Biol Med* **65**, 124–136 (2015).

208. Liefers, B. *et al.* A deep learning model for segmentation of geographic atrophy to study its long-term natural history. *Ophthalmology* **127**, 1086–1096 (2020).

209. Hu, Z. *et al.* Segmentation of the geographic atrophy in spectral-domain optical coherence tomography and fundus autofluorescence images. *Invest Ophthalmol Vis Sci* **54**, 8375–8383 (2013).

210. Almasian, M., Bosschaart, N., Leeuwen, T. G. & Faber, D. J. Validation of quantitative attenuation and backscattering coefficient measurements by optical coherence tomography in the concentration-dependent and multiple scattering regime. *J Biomed Opt* **20**, 121314 (2015).

211. Faber, D. J., Meer, F. J., Aalders, M. C. & Leeuwen, T. G. Quantitative measurement of attenuation coefficients of weakly scattering media using optical coherence tomography. *Opt Express* **12**, 4353–4365 (2004).

212. Liu, J. *et al.* Optimized depth-resolved estimation to measure optical attenuation coefficients from optical coherence tomography and its application in cerebral damage determination. *J Biomed Opt* **24**, 035002 (2019).

213. Davis, M. D. *et al.* The age-related eye disease study severity scale for age-related macular degeneration - AREDS report no. 17. *Arch Ophthalmol* **123**, 1484–1498 (2005).

214. Christenbury, J. G. *et al.* Progression of Intermediate Age-related Macular Degeneration with Proliferation and Inner Retinal Migration of Hyperreflective Foci. *Ophthalmology* **120**, 1038–1045 (2013).

215. Sleiman, K. *et al.* Optical Coherence Tomography Predictors of Risk for Progression to Non-Neovascular Atrophic Age-Related Macular Degeneration. *Ophthalmology* **124**, 1764–1777 (2017).

216. Lei, J. Q., Balasubramanian, S., Abdelfattah, N. S., Nittala, M. G. & Sadda, S. R. Proposal of a simple optical coherence tomography-based scoring system for progression of age-related macular degeneration. *Graefes Arch Clin Exp Ophthalmol* **255**, 1551–1558 (2017).

217. Nassisi, M. *et al.* Quantity of Intraretinal Hyperreflective Foci in Patients With Intermediate Age-Related Macular Degeneration Correlates With 1-Year Progression. *Invest Ophthalmol Vis. Sci* **59**, 3431–3439 (2018).

218. Nassisi, M. *et al.* OCT Risk Factors for Development of Late Age-Related Macular Degeneration in the Fellow Eyes of Patients Enrolled in the HARBOR Study. *Ophthalmology* **126**, 1667–1674 (2019).

219. Curcio, C. A., Zanzottera, E. C., Ach, T., Balaratnasingam, C. & Freund, K. B. Activated Retinal Pigment Epithelium, an Optical Coherence Tomography Biomarker for Progression in Age-Related Macular Degeneration. *Invest Ophthalmol Vis. Sci* **58**, 211–226 (2017).

220. Varga, L. *et al.* Automatic segmentation of hyperreflective foci in OCT images. *Comput. Methods Programs Biomed.* **178**, 91–103 (2019).

221. Spaide R. F., Noble K., Morgan A. & Freund K. B. Vitelliform macular dystrophy. *Ophthalmology* **113**, 1392-1400 4 (2006).

222. Zhou, H. *et al.* Mitigating the effects of choroidal hyper- and hypo-transmission defects on choroidal vascularity index assessments using optical coherence tomography. *Quant Imaging Med Surg* **12**, 2932–2946 (2022).

223. Chu, Z. *et al.* Optical Coherence Tomography Measurements of the Retinal Pigment Epithelium to Bruch Membrane Thickness Around Geographic Atrophy Correlate With Growth. *Am J Ophthalmol* **236**, 249–260 (2022).

224. Zhou, H. *et al.* Automated morphometric measurement of the retinal pigment epithelium complex and choriocapillaris using swept source OCT. *Biomed Opt Express* **11**, 1834–1850 (2020).

225. Gong, P. *et al.* Parametric imaging of attenuation by optical coherence tomography: review of models, methods, and clinical translation. *J Biomed Opt* **25**, (2020).

226. Schmitt, J. M., Knuttel, A., Yadlowsky, M. & Eckhaus, M. A. Optical-Coherence Tomography of a Dense Tissue - Statistics of Attenuation and Backscattering. *Phys Med Biol* **39**, 1705–1720 (1994).

227. Chang, S. & Bowden, A. K. Review of methods and applications of attenuation coefficient measurements with optical coherence tomography. *J Biomed Opt* **24**, (2019).

228. Ghafaryasl, B. *et al.* Attenuation coefficient estimation in Fourier-domain OCT of multi-layered phantoms. *Biomed Opt Express* **12**, 2744–2758 (2021).

229. Li, K., Liang, W., Yang, Z., Liang, Y. & Wan, S. Robust, accurate depth-resolved attenuation characterization in optical coherence tomography. *Biomed Opt Express* **11**, 672–687 (2020).

230. Hohmann, M. *et al.* Direct measurement of the scattering coefficient. *Biomed Opt Express* **12**, 320–335 (2021).

231. Stromer, D. *et al.* Correction propagation for user-assisted optical coherence tomography segmentation: general framework and application to Bruch's membrane segmentation. *Biomed Opt Express* **11**, 2830–2848 (2020).

232. Schottenhamml, J. *et al.* OCT-OCTA segmentation: combining structural and blood flow information to segment Bruch's membrane. *Biomed Opt Express* **12**, 84–99 (2021).

233. Heikka, T., Cense, B. & Jansonius, N. Retinal layer thicknesses retrieved with different segmentation algorithms from optical coherence tomography scans acquired under different signal-to-noise ratio conditions. *Biomed Opt Express* **11**, 7079–7095 (2020).

234. Borkovkina, S., Camino, A., Janpongsri, W., Sarunic, M. & Jian, Y. Real-time retinal layer segmentation of OCT volumes with GPU accelerated inferencing using a compressed, low-latency neural network. *Biomed Opt Express* **11**, 3968–3984 (2020).

235. Romo-Bucheli, D. *et al.* Reducing image variability across OCT devices with unsupervised unpaired learning for improved segmentation of retina. *Biomed Opt Express* **11**, 346–363 (2020).

236. Li, J. *et al.* Multi-scale GCN-assisted two-stage network for joint segmentation of retinal layers and discs in peripapillary OCT images. *Biomed Opt Express* **12**, 2204–2220 (2021).

237. Wang, J. *et al.* Weakly supervised anomaly segmentation in retinal OCT images using an adversarial learning approach. *Biomed Opt Express* **12**, 4713–4729 (2021).

238. Saxena, A. *et al.* Framework for quantitative three-dimensional choroidal vasculature analysis using optical coherence tomography. *Biomed Opt Express* **12**, 4982–4996 (2021).

239. Mukherjee, S. *et al.* Retinal layer segmentation in optical coherence tomography (OCT) using a 3D deep-convolutional regression network for patients with age-related macular degeneration. *Biomed Opt Express* **13**, 3195–3210 (2022).

240. Yu, C. C. *et al.* Hyper-reflective foci segmentation in SD-OCT retinal images with diabetic retinopathy using deep convolutional neural networks. *Med Phys* **46**, 4502–4519 (2019).

241. Okuwobi, I. P. *et al.* Automated Quantification of Hyperreflective Foci in SD-OCT With Diabetic Retinopathy. *IEEE J Biomed Health Inf.* **24**, 1125–1136 (2020).

242. Xie, S. *et al.* Fast and Automated Hyperreflective Foci Segmentation Based on Image Enhancement and Improved 3D U-Net in SD-OCT Volumes with Diabetic Retinopathy. *Trans Vis Sci Tech* **9**, 21 (2020).

243. Ho, J. *et al.* Documentation of Intraretinal Retinal Pigment Epithelium Migration via High-Speed Ultrahigh-Resolution Optical Coherence Tomography. *Ophthalmology* **118**, 687–693 (2011).

244. Fragiotta, S. *et al.* Significance of Hyperreflective Foci as an Optical Coherence Tomography Biomarker in Retinal Diseases: Characterization and Clinical Implications. *J Ophthalmol.* 1–10 (2021).